POLITECNICO DI MILANO

Scuola di Ingegneria Industriale e dell'Informazione

Corso di Laurea Magistrale in
Materials Engineering and Nanotechnology

Ab Initio Study on the Thermal Transport Properties of Bidimensional Materials: Application to Thermoelectricity

Nano-Materials for Energy Lab
Institut Lumière Matière
Villeurbanne CEDEX, France

Relatore esterno: Prof. Christophe Adessi
Correlatore esterno: Prof. Georges Bouzerar
Relatore interno: Prof. Andrea Li Bassi

Tesi di Laurea Magistrale di:
Stefano Pecorario, matricola 878124

Anno Accademico 2018-2019

Ai miei genitori

Acknowledgements

I would like to express my deep gratitude to Prof. Christophe Adessi for his mentoring and support during my internship in Lyon. I am thankful to Prof. Georges Bouzerar for the time spent discussing about my work and for his sharp suggestions. Many thanks also to Simon Thébaud and Mehdi Meziane for their tips and for having shared their office with me.
I am grateful to Prof. Andrea Li Bassi for his always punctual advice.
Furthermore, I am thankful to Maryse for her support and her patient help in proofreading the work.
I would like to express my limitless gratitude to my family for their lifelong support and for always believing in me.
Finally, I am thankful to all my friends who made these years at university beautiful.

Abstract

My master thesis consists of a DFT study on the thermal transport properties of graphene and single-layer transition metal dichalcogenides.
Calculations have been performed using the *SIESTA* DFT package based on atomic orbitals. In a first part, the phonon dispersion relation of graphene, MoS_2, $MoSe_2$, WS_2 and WSe_2 were calculated. By means of the Landauer formalism, the ballistic phonon transmission function and the thermal conductance were computed and compared. Using the atomistic Green's function technique, the influence of a disordered distribution of sulphur vacancies on the thermal conductivity was analysed. The thermoelectric figure of merit of MoS_2 in presence of sulphur vacancies was obtained as well.
Finally, a procedure was developed to include in the calculations the effect of phonon-phonon Umklapp scattering and scattering due to the roughness of the boundaries. This method was successfully applied to compute the lattice thermal conductivity of graphene, allowing to evaluate the impact of scattering as a function of the temperature and of the size of the samples.

Sommario

La mia tesi di laurea magistrale consiste in uno studio computazionale sulle proprietà di trasporto termico in materiali bidimensionali, quali il grafene e i monostrato dicalcogenuri dei metalli di transizione (single-layer TMDCs). I materiali 2D sono un argomento di ricerca che è attualmente di particolare interesse per uno svariato numero di possibili applicazioni in campi come elettronica, fotonica, catalisi, immagazzinamento dell'energia e termoelettricità.
Questa tesi si concentra sulle proprietà termoelettriche di grafene, MoS_2, WS_2, $MoSe_2$ e WSe_2. Buoni materiali termoelettrici si identificano per un'ottima conduttività elettrica, un elevato coefficiente di Seebeck e una bassa conduttività termica.
Queste caratteristiche sono solitamente proprie di semiconduttori altamente drogati. I single-layer TMDCs sono semiconduttori a gap diretto, con ottime potenzialità come materiali termoelettrici. Diversamente, il grafene è un ottimo conduttore sia elettrico che termico e il suo coefficiente di Seebeck è ridotto a causa dell'assenza di un gap elettronico. Tuttavia, i nanoribbon di grafene presentano un gap elettronico dovuto a effetti di confinamento spaziale degli elettroni. Inoltre, in quanto capostipite della famiglia dei materiali bidimensionali, il grafene si presta ad essere il miglior sistema per la comprensione dei fenomeni di trasporto in materiali 2D e per una comparazione con lo studio dei single-layer TMDCs.
Oltre a ricercare materiali con ottime proprietà termoelettriche intrinseche, il modo più efficace con cui si cerca di incrementare l'efficienza di conversione termoelettrica consiste nel ridurre la conduttività termica mediante metodi come la nanostrutturazione del materiale e l'introduzione di difetti (impurità, lacune, interfacce). L'obiettivo è quello di ostacolare il trasporto fononico senza impattare in modo significativo sul trasporto elettrico, in modo che gli elettroni si propaghino come in un mezzo cristallino e i fononi come in un materiale amorfo.

L'intento di questo lavoro di tesi è quello di investigare con metodi computazionali il trasporto dei fononi nei sopracitati materiali 2D alla scala mesoscopica. Le simulazioni si basano su calcoli DFT eseguiti mediante il metodo "SIESTA" (Capitolo 1), con cui, tra le altre cose, si ottengono le curve di dispersione fononiche. La funzione di trasmissione dei fononi e la conduttanza termica sono calcolate nel contesto del formalismo di Landauer (Capitolo 2).

Nella prima parte, si mostrano le relazioni di dispersione dei fononi in grafene, MoS_2, $MoSe_2$, WS_2 e WSe_2. Inoltre, si calcola la conduttanza termica (contributo fononico) in funzione della temperatura in regime di trasporto balistico. Le nette differenze tra le proprietà di trasporto termico del grafene e dei TMDCs vengono evidenziate (Capitolo 4).
Nella seconda parte, si analizza l'impatto di vacanze di zolfo in single-layer MoS_2 al fine di ostacolare il trasporto di fononi e, di conseguenza, aumentare l'efficienza termoelettrica del materiale. Mediante un metodo basato sulle funzioni di Green, si valuta l'influenza di una distribuzione disordinata delle vacanze. Gli effetti sulla conduttività termica sono investigati in funzione della concentrazione delle lacune e delle dimensioni dei campioni. I risultati mostrano una significativa riduzione della conduttività termica rispetto a quella del materiale privo di difetti. Tuttavia, si mostra che anche le proprietà elettriche sono inficiate dalla presenza di vacanze di zolfo; pertanto, si procede al calcolo della figura di merito del sistema, traendone la conclusione che l'efficienza del materiale può essere lievemente migliorata solo per MoS_2 drogato di tipo p (Capitolo 5). La valutazione della figura di merito per MoS_2 in presenza di un sistema disordinato di vacanze costituisce un contributo originale rispetto a quanto presente in letteratura.

Nell'ultima parte si mostra una procedura sviluppata autonomamente per includere l'impatto sul trasporto termico dei fenomeni di scattering fonone-fonone (processo Umklapp) e di scattering fonone-interfaccia. Il metodo è basato su un approccio che combina il calcolo della funzione di trasmissione fononica secondo il formalismo di Landauer e la valutazione del cammino libero medio dei fononi nel materiale, attraverso il calcolo del parametro di Grüneisen . I fondamenti teorici di questo metodo sono descritti nel Capitolo 3. La procedura è applicata con successo al fine di calcolare la conduttività termica (contributo fononico) del grafene in un regime di transizione balistico-diffusivo (Capitolo 6).

Contents

Introduction

0.1 2D Materials

Since the discovery of graphene in 2004 by Novoselov *et. al.* [62], two-dimensional (2D) materials have attracted intensive attention due to their unique physical properties and the potential technological applications in fields such as electronics, photonics, catalysis, spintronics and energy storage [59, 88, 12, 98].
There exists a huge variety of bidimensional materials. Some of them are monolayers comprising a single element (e.g. graphene, phosphorene, germanene and silicene), while others feature different atoms alternating in the same layer (e.g. boron nitride, transition metal dichalcogenides (TMDCs) and MXenes).
The combination of 2D layers in Van der Waals heterostructures, in which different monolayers are freely mixed and matched, further expands the opportunities for exploring new physics and applications [38, 50].
Besides graphene, which is the first and most studied 2D material, this thesis will focus on the following TMDCs: MoS_2, WS_2, $MoSe_2$ and WSe_2.
The general formula of TMDCs is MX_2, where M is a transition metal atom (like Mo and W) and X a chalcogen atom (like S and Se). Their structure consists of a layer of M atoms sandwiched between two layers of X atoms, as depicted in fig. 1.

Layered transition metal dichalcogenides have shown high potential due to their intriguing semiconducting properties. In fact, while pristine graphene has no band gap, the above mentioned monolayer TMDCs exhibit direct band gap, making them ideal for a wide range of potential applications in electronics, optoelectronics and photovoltaics. Moreover, they present high electron mobility and a unique layer-dependent band gap tunability, with a transition from indirect gap (multilayer) to direct gap (monolayer) [72].
More recently these materials have attracted increased attention in the prospect of thermoelectricity on both theoretical [1, 85, 88] and experimental sides. [90, 95].
The aim of this thesis is to investigate the thermoelectric properties of MoS_2, WS_2, $MoSe_2$ and WSe_2.

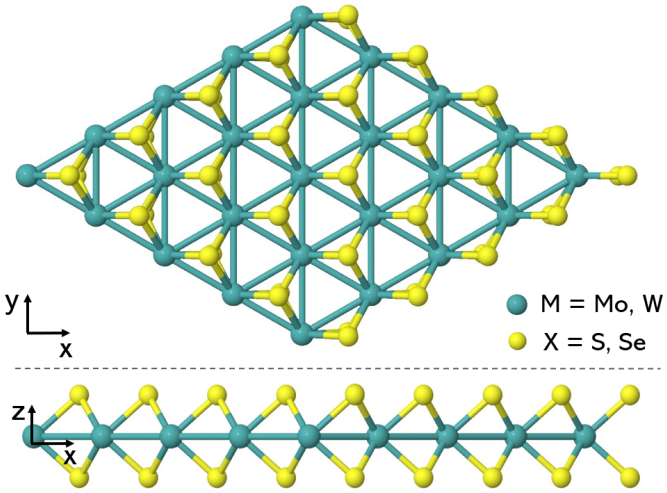

Figure 1: Structure of monolayer transition metal dichalcogenides. MoS_2, WS_2, $MoSe_2$ and WSe_2 are studied in this thesis.

0.2 Thermoelectric Materials

At this point, a few words about thermoelectrity are needed.
Thermoelectric (TE) materials can convert heat into electricity (Seebeck effect) or viceversa (Peltier effect). Recently, these materials have been attracting attention for the development of devices for power generation from waste heat or as solid-state Peltier coolers.
Radioisotope Thermoelectric Generators are lightweight, compact spacecraft power systems that are extraordinarily reliable. For example, they were used to power NASA's Voyager and Cassini missions [61]. Nowadays power generation applications are being studied by the automotive industry with the aim to develop electrical power from waste engine heat.
A thermoelectric generator uses heat flow across a temperature gradient to power an electric load through the external circuit. The physical principle at the basis of thermoelectric power generators is known as the Seebeck effect. When a temperature gradient is applied to a TE material, an electrostatic potential builds up due to the diffusion of free charges from the hot end to the cold end. An equilibrium is thus reached between the chemical potential for diffusion and the electrostatic repulsion caused by the separation of charges. The Seebeck coefficient S, also known as thermopower, is defined as the ratio between the build-up voltage and the applied temperature difference ($S = \frac{\Delta V}{\Delta T}$). Hence, in thermoelectric generators, the heat flow drives the electrical current and supplies power to an external circuit. Vice versa in Peltier coolers, the d.c. power, which is supplied by the external circuit, drives the electric current (I) and the heat flow (Q). The result is the cooling of the top surface thanks to the Peltier effect ($Q = ST\,I$) [70].
Thermoelectric refrigeration is an environment-friendly method of small-scale localized cooling in computers, infrared detectors, electronics, optoelectronics as well as many other applications. If significant economical cooling is achieved, the resulting "cold computing" would produce large

speed gains in some CMOS computer processors [79].
The usual design of TE devices corresponds to many thermoelectric couples (fig. 2, bottom) consisting of n-type and p-type thermoelectric elements wired electrically in series and thermally in parallel (fig. 2, top).

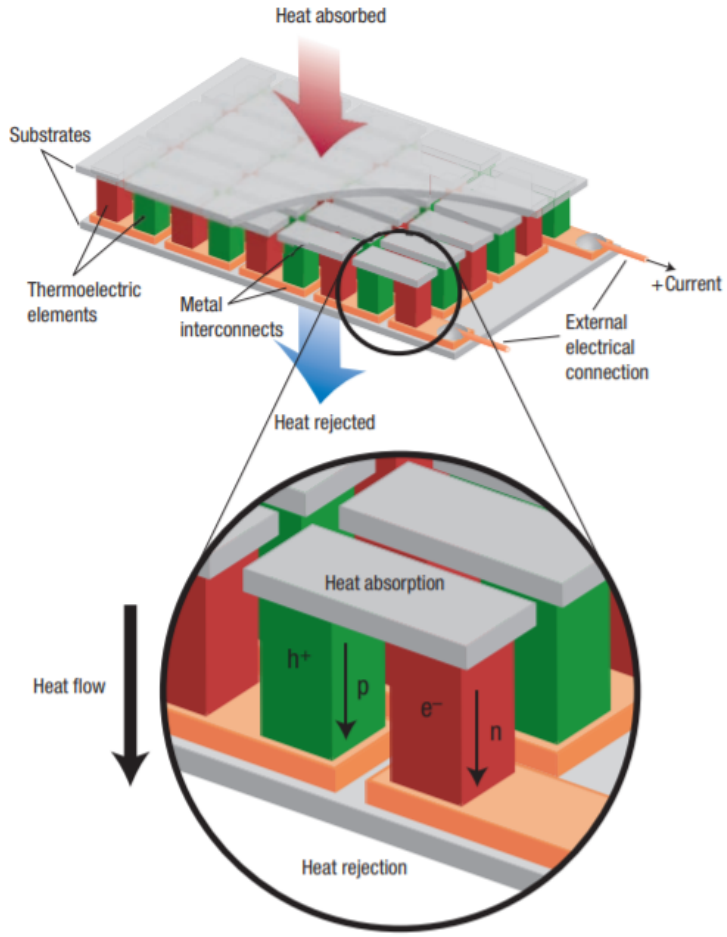

Figure 2: Thermoelectric module showing the direction of charge flow on both cooling and power generation. From ref. [70]

The efficiency of thermoelectric conversion is characterized by the dimensionless figure of merit ZT:

$$ZT = \frac{\sigma_{el}\, S^2}{\kappa_{el} + \kappa_{ph}}\, T \tag{1}$$

where S is the Seebeck coefficient, σ_{el} the electrical conductivity, T the absolute temperature, κ_{el} and κ_{ph} the thermal conductivity contributed by electrons and phonons respectively. Materials with $ZT \sim 1$ are nowadays considered as good thermoelectrics, while their ZT values need to be at least 3 so that the conversion efficiency could be competitive with conventional power generators and refrigerators [91].
To maximize the thermoelectric figure of merit of a material, a large Seebeck coefficient, high electrical conductivity and low thermal conductivity

are required.
Thus, it is fundamental to optimize a series of conflicting parameters.
Metals own a high electrical conductivity, but their Seebeck coefficient is very low (only a few mV/K). S is much larger for semiconductors (typically a few 100 mV/K) [79]. Furthermore, their σ_{el}, which is several orders of magnitude lower than the metals' one, can be improved by doping. Hence, good material candidates for thermoelectricity are highly doped semiconductors with a narrow band gap.
Moreover, the most common approach to improve ZT embraces the minimization of the phonon contribution to the thermal conductivity.
The heat flow is carried by a spectrum of phonons with widely varying wavelengths and mean free paths (from less than 1 nm to greater than 10 μm), creating a need for phonon scattering agents at a variety of length scales. Therefore, suitable thermoelectrics are crystalline materials that manage to scatter phonons without significantly disrupting the electrical conductivity. The ideal TE material behaves like a "phonon-glass electron-crystal"(Slack 1995). The electron-crystal requirement arises from the fact that crystalline semiconductors provide the best electronic properties (Seebeck coefficient and electrical conductivity). The phonon-glass requirement originates from the need for as low a lattice thermal conductivity as possible.

During the past decades, it has been proved that low-dimensional or micro-nano systems tend to exhibit better thermoelectric performance than traditional bulk materials [14, 91]. In fact, the thermal conductivity of these nanostructures could be significantly lowered compared with their bulk counterparts. Several ways have been tried to tune the phonon spectrum and engineer the thermal properties of low-dimensional materials (via ribbon edges, grain boundaries, isotope composition, defect concentration, and atomic-plane orientation).

0.3 Motivations and Goals

This thesis focuses on the computational study of the thermal transport properties in bidimensional systems, in particular, graphene and single-layer (SL) TMDCs. The first results, shown in Ch. 4, regard a comparison between the phonon dispersion relation and the lattice thermal conductance of graphene, MoS_2, WS_2, MoS_2 and WSe_2. This first analysis is conducted on pristine (defectless) materials and aims to understand the phonon transport properties in ballistic regime.
Graphene is known for having extremely high thermal conductivity (2000-5000 $\mathrm{W\,m^{-1}\,K^{-1}}$) and a low Seebeck coefficient. Hence it is a promising material for heat removal applications, but not for thermoelectric devices. However, the study of pristine graphene in this thesis is interesting for two principal reasons: firstly because it is the most studied 2D material; it is the model for understanding transport phenomena in a series of low-dimensional

systems (e.g. carbon nanotubes). Secondly, graphene nanoribbons present a gap due to size-confinement effects. This paves the way to their application in thermoelectricity, provided that suitable ways are found to reduce the high thermal conductivity.
Diversely, large Seebeck coefficient and low thermal conductivity were found in SL TMDCs, both with computational simulations and experimental measurements.
Theoretical estimates for the TMDCs' thermal conductivity span from the ultralow value of 3.9 $\mathrm{W\,m^{-1}\,K^{-1}}$ for WSe_2 [102] to 33.6 $\mathrm{W\,m^{-1}\,K^{-1}}$ for MoS_2 [57].
Experimental measurements on 2D systems are extremely complex due to the dependence on a series of conditions, such as the particular measurement technique, the sample's quality, edge-roughness and interactions with the substrate. This difficulty is reflected in different values reported in literature: for example, by utilizing micro-Raman thermometry, room temperature thermal conductivity of 34.5 ± 4 $\mathrm{W\,m^{-1}\,K^{-1}}$[93] and 62.2 $\mathrm{W\,m^{-1}\,K^{-1}}$ [73] was measured for MoS_2 monolayer flakes exfoliated by bulk crystal.

Because of the simple crystal structure of 2D materials and the increased computational power, atomistic simulations are valuable tools to understand the underlying phonon transport mechanisms and predict their thermal conductivity. In order to study thermal transport in a crystal with periodic lattice structure, one can model the lattice vibration and thermal conductivity from either real space or reciprocal space. In both the approaches, the potentials or force-fields that describe the interatomic interactions are essential.
In the real space approach, such as molecular dynamics (MD) simulations, the thermal conductivity of the crystal is obtained by monitoring the movement of each atom. In the classical MD simulations, empirical interatomic potentials with simplified analytical expressions are used. They are usually obtained by fitting only a few physical properties of the materials, such as lattice constant, elastic constants or interatomic forces. As a matter of fact, it is challenging to reproduce phonon properties accurately [22].
In the reciprocal space approach, the interatomic force-constants are computed from first-principles (*ab initio*) by density functional theory (DFT) calculations. The lattice vibrations are then decomposed to normal modes, i.e. phonons in the quantum mechanics' point of view. The contribution of each phonon mode to the thermal conductivity is determined by the calculation of the phonon dispersion and the phonon scattering matrix [22]. Finally, the thermal conductivity can be calculated by using the kinetic theory such as Peierls-Boltzmann transport equation (PBTE) based method or with the atomistic Green's function (AGF) technique [96]. The Peierls-Boltzmann approach is often applied within the relaxation time approximation. It consists in a semi-classical theory with no quantum effects, which describes scattering mechanisms by an effective relaxation time. This method is suitable to study diffusive transport, but it is impractical to analyse the specific contribution brought by different scattering mechanisms, as it occurs

in presence of defects in the lattice.
The AGF technique is based on the Landauer formalism for transport in ballistic or semiballistic regime. This method allows to fully investigate scattering by a disordered distribution of defects in the lattice, since it relies on *ab initio* calculations including realistic defects.

In this thesis, the interatomic force constants have been computed using *ab initio* calculations, based on the *SIESTA* DFT package [71]. *SIESTA* is both a method and its computer program implementation. It allows to perform efficient electronic structure calculations and *ab initio* molecular dynamics simulations of molecules and solids. *SIESTA*'s efficiency stems from the use of strictly localized basis sets and from the implementation of linear-scaling algorithms which can be applied to suitable systems.[1]
An introduction on DFT and on the main features to perform phonon calculations with *SIESTA* is provided in Ch. 1. The transport properties have been obtained using the AGF technique on the basis of the Landauer formalism, which is extensively described in Ch. 2.

This approach turned out to be fundamental to study the effect of a disordered distribution of sulphur vacancies in SL MoS_2. The aim in this part was twofold: firstly to understand if the thermal conductance in presence of sulphur vacancies is lower than in the pristine material; secondly to evaluate the overall effect on the thermoelectric figure of merit by combining my analysis on the thermal conductance with the electronic properties computed by Christophe Adessi. A similar study has been performed by Yongchun Wang *et. al.* [87], who found that the lattice thermal conductivity of MoS_2 nanoribbons is significantly suppressed by sulphur vacancies and substitutional oxigens as well. It was also claimed that sulphur vacancies are helpful to enhance the thermoelectric performance of MoS_2. However, no ZT values were given in the paper to support this information. Moreover, the study was based on non-equilibrium molecular dynamics and not on fully *ab intio* calculations. Other works about the impact of sulphur vacancies on the thermal conductivity of monolayer TMDCs are present in literature [55, 94]. In these studies, which are based on first principles calculations and on PBTE, the defective monolayers were generated by removing one or two atoms in the simulated lattice. None of them evaluated the effect of a realistic disordered distribution of vacancies, for which the AGF method is required. The goal of the second part of this thesis is to examine the figure of merit by changing the concentration of the defects and the length of the samples. The analysis is based on a technique that allows to generate random distributions of defects and to average over the data obtained for different configurations.
This treatment, able to deal with disordered distribution of defects, is also

[1] *SIESTA* official web page: https://departments.icmab.es/leem/siesta/
SIESTA's backronym is Spanish Initiative for Electronic Simulations with Thousands of Atoms.

promising in the prospective of future studies. For example, a combination of different kinds of defects can be inserted in the material, or the concentration of defects can be tuned locally, with the purpose of finding better and better strategies to achieve a good "phonon-glass electron-crystal" behaviour via defect engineering.

The last part of the thesis is dedicated to the implementation of a method to evaluate the effect of phonon-phonon Umklapp scattering on the thermal conductivity. Taking inspiration from works published in literature [28, 57, 7, 85], I proposed a mixed approach that combines the Landauer formalism with the calculation of the phonon life time as it is done within PBTE in relaxation time approximation. The scattering due to the roughness of the boundary was included in a qualitative way as well. This method is illustrated in details in Ch. 3. The main problem which has been faced consisted in the calculation of the mode Grüneisen parameter, which characterises the strength of the Umklapp phonon-phonon scattering and is fundamental to evaluate the phonon life time according to the expression given by Klemens [35]. This approach is based on the Landauer formalism; hence, it is compatible with the AGF method, which is necessary to evaluate the effect of scattering by defects and treat disordered systems.
This work has the merit to provide a technique to account for inelastic scattering, which has never been done before by the team. Its reliability has been tested by computing the thermal conductivity of graphene as a function of the temperature and of the size of the sample. This study is presented in Ch. 6.
Even if the recent availability of high quality single-layer graphene samples has allowed for a high number of experimental studies [17], a large variety of estimates are reported in literature, spanning a rather wide range of values between 1500 and 5000 $\mathrm{W\,m^{-1}\,K^{-1}}$ at room temperature. On the theoretical side, the estimates are equally uncertain and vary in an even larger range of κ between 1000 and 10000 $\mathrm{W\,m^{-1}\,K^{-1}}$ [48, 22].
The employed approach provided estimates in the same order of magnitude of those reported in literature, therefore being able to treat the transition between ballistic and diffusive regime.

0.4 Structure of the Thesis

This thesis is organised in two parts. The first one presents an overview of the theoretical methods and of the formalisms which have been used. In particular:

- In Chapter 1 a review of Density Functional Theory is discussed, paying particular attention to the main features of the *SIESTA* method which has been fundamental for the types of calculations performed. A description of the procedure employed to optimize the unit cell structure is given. In addition, the main steps necessary in order to obtain the phonon dispersion relation are examined.

- Chapter 2 focuses on the Landauer formalism to study transport phenomena at the mesoscopic scale. A brief introduction gives an overview of the relevant length scales to distinguish among different transport regimes. The first part treats the case of electronic transport, deriving the formalism to compute the thermoelectric transport coefficients, while the second part deals with the transport of phonons. Great attention is devoted to the meaning of the transmission function which is the key quantity of the formalism. The two methods to compute the transmission are described and compared: the first one is based on the direct calculation of the density of modes from the dispersion relation and can be applied to pristine materials, the second one relies on the atomistic Green's functions technique, which is essential to treat systems with a disordered distribution of defects.

- In Chapter 3, one can find a detailed description of the method that I have implemented in order to include the effect of phonon-phonon and phonon-boundary scattering mechanisms in the derivation of the thermal conductivity. A brief introduction discusses the Normal and Umklapp phonon-phonon scattering processes. Then, the procedure to compute the phonon mean free paths and evaluate the transmission coefficient is examined; a key point regards the calculation of the mode Grüneisen parameter. A final section is dedicated to explain the differences of the approach used in this thesis with others presented in literature.

In the second part of the thesis the results of the calculations are presented:

- In Chapter 4 the thermoelectric transport properties of graphene and TMDCs (MoS_2, WS_2, $MoSe_2$, WSe_2) are investigated. The electronic band structure and the density of states of these materials are calculated as first step. Furthermore, the phonon dispersion relations and the phonon density of states are discussed. Afterwards, the phonon transmission is computed. Finally, the curves of the ballistic thermal conductance per unit width as a function of the temperature are presented and compared.

- Chapter 5 aims to evaluate the impact of a disordered distribution of sulphur vacancies on the lattice thermal conductivity of MoS_2. By using the atomistic Green's functions technique, two analyses are shown: the first one considers a variable concentration of vacancies with fixed length of the device; the second one takes into account different lengths of the device by keeping the concentration of vacancies constant. Furthermore, the information regarding the lattice thermal conductivity are combined with the electrical properties in order to obtain the thermoelectric figure of merit of the considered systems.

- In Chapter 6, the method introduced in Chapter 3 is applied in the case of graphene in order to include phonon-phonon Umklapp scattering and phonon-boundary scattering in the calculation of the thermal conductivity. Before achieving the final results, all the steps of the method are presented, showing the calculations of phonon group velocities, mode Grüneisen parameter, phonon life times and mean free paths.

Finally the conclusions of these studies are summarized in Chapter 7.

Part I

Theoretical Methods

Chapter 1

The *SIESTA* method for *ab initio* calculations

This chapter describes the procedure used to perform calculations with *SIESTA* [71, 2], aiming to compute the electronic band structure and the phonon dispersion relation of materials from first principles. The first section provides an introduction to density functional theory (DFT) and explains the main features of the *SIESTA* method with respect to other programs for DFT calculations.
In addition, the main steps necessary to compute electronic and phononic properties will be discussed.

1.1 Introduction to Density Functional Theory

The aim of a theoretical *ab initio* study is to describe properties of matter starting from fundamental principles and without empirical input.
To investigate the steady state electronic and vibrational properties of materials, the first step consists in solving the many-body time-independent Schrödinger equation that, in non-relativistic approximation, is written as follows:

$$\hat{H}\Psi\Big(\{\mathbf{x}_i\},\{\mathbf{R}_\alpha\}\Big) = E\Psi\Big(\{\mathbf{x}_i\},\{\mathbf{R}_\alpha\}\Big) \tag{1.1}$$

where $\mathbf{x}_i$ represents the coordinates of electron i (both spatial coordinates $\mathbf{r}_i$ and spin[1] coordinates σ_i), $\mathbf{R}_\alpha$ are the spatial coordinates of nucleus α and $\hat{H}$ is the many-body hamiltonian, which takes into account all the interactions:

$$\hat{H} = \hat{T}_e + \hat{T}_n + \hat{V}_{e-n} + \hat{V}_{n-n} + \hat{V}_{e-e} \tag{1.2}$$

with[2]:

[1] In this thesis, spin is considered purely to include the Pauli exclusion principle in the computation of the density of states. In absence of magnetic fields, the dependence on spin of the transport properties studied can be neglected with good approximation. Thus, the spin coordinates will be left out hereafter to simplify the notation.

[2] Energies expressed with the CGS system of units.

$$\hat{T}_e = -\sum_i \frac{\hbar^2}{2m_e}\nabla^2 \qquad \text{kinetic energy operator for the electrons}$$

$$\hat{T}_n = -\sum_\alpha \frac{\hbar^2}{2M_n}\nabla^2 \qquad \text{kinetic energy operator for the nuclei}$$

$$\hat{V}_{e-n} = -\sum_{i,\alpha} \frac{Z_\alpha e^2}{|\mathbf{r}_i - \mathbf{R}_\alpha|} \qquad \text{electron-nuclei interaction}$$

$$\hat{V}_{n-n} = \frac{1}{2}\sum_{\alpha\neq\beta} \frac{Z_\alpha Z_\beta e^2}{|\mathbf{R}_\alpha - \mathbf{R}_\beta|} \qquad \text{nucleus-nucleus interaction}$$

$$\hat{V}_{e-e} = \frac{1}{2}\sum_{i\neq j} \frac{e^2}{|\mathbf{r}_i - \mathbf{r}_j|} \qquad \text{electron-electron interaction}$$

Since the studied systems are infinite crystals, the electronic wave function must respect Bloch's theorem. The Schrödinger equation must be solved with appropriate boundary conditions, which for a regular bulk solid are typically the Born-Von Karman periodic boundary conditions.
Once the problem has been solved, knowing the many-body wave function, it is possible to compute the expectation values of all the thermodynamic observables:

$$\langle \hat{A} \rangle = \frac{\langle \Psi | \hat{A} | \Psi \rangle}{\langle \Psi | \Psi \rangle} = \frac{\int \Psi^\dagger \hat{A} \Psi d\mathbf{r} d\mathbf{R}}{\int \Psi^\dagger \Psi d\mathbf{r} d\mathbf{R}} \tag{1.3}$$

The total energy, which is a functional of the many-body wave function, is the expectation value of the hamiltonian:

$$E[\Psi] = \langle \hat{H} \rangle = \frac{\langle \Psi | \hat{H} | \Psi \rangle}{\langle \Psi | \Psi \rangle} \tag{1.4}$$

It is worth to note that the ground state energy, E_0 can be obtained by diagonalization of the eigenvalue problem solving (1.4), but also by minimization of the energy functional, according to the variational principle [20]:

$$E_0 = \min_\Psi E[\Psi] \tag{1.5}$$

This second method is useful to compute the ground state properties of the system when the exact many-body wave function is unknown. In fact, the many-body Schrödinger equation can be solved analytically only for two particles or for the harmonic oscillator; furthermore, numerical solutions are possible only for systems of very few particles. Thus, the challenge is to

deal with the complex many-body problem by introducing suitable approximations, which will be demonstrated in the following paragraphs.

Firstly, within the adiabatic (or Born-Oppenheimer) approximation, the nuclei can be considered as "frozen" in their equilibrium position[3]. This allows to decouple the electronic and nuclear degrees of freedom. [20]
Hence, the total wavefunction Ψ is taken as the product of two independent contributions of the electrons and the nuclei:

$$\Psi(\mathbf{r}, \mathbf{R}) = \psi_e(\mathbf{r}|\mathbf{R})\phi_n(\mathbf{R}) \tag{1.6}$$

with the nuclei coordinates acting as parameters in the electronic wave function expression[4].
Therefore, the full many-body Schrödinger equation is reduced to two independent equations for the electrons (1.7) and the nuclei (1.8):

$$\begin{aligned} &\hat{H}_e(\mathbf{r}|\mathbf{R})\psi_e(\mathbf{r}|\mathbf{R}) = E_e(\mathbf{R})\psi_e(\mathbf{r}|\mathbf{R}), \\ &\hat{H}_e(\mathbf{r}|\mathbf{R}) = \hat{T}_{e-e}(\mathbf{r}) + \hat{V}_{e-e}(\mathbf{r}) + \hat{V}_{e-n}(\mathbf{r}|\mathbf{R}) \end{aligned} \tag{1.7}$$

$$\begin{aligned} &\hat{H}_n(\mathbf{R})\phi(\mathbf{R}) = E_{tot}\phi(\mathbf{R}), \\ &\hat{H}_n(\mathbf{R}) = \hat{T}_n + \hat{V}_{n-n}(\mathbf{R}) + \hat{E}_e(\mathbf{R}) \end{aligned} \tag{1.8}$$

In this way, given a static configuration of the nuclei, the Schrödinger equation for the electrons (1.7) is solved. At this point, the electronic energy $E_e(\mathbf{R})$, coming from the solution of the electronic problem, is inserted in (1.8), where it acts as a mean potential generated by the electrons.
It should be noted that the energy eigenvalue E_{tot} represents the total energy of the system, including nuclear and electronic contributions.

In order to deal with the electron-electron interaction term in the electronic hamiltonian, different approaches have been tried, such as the Hartree-Fock method, Perturbation Theory and Density Functional Theory (DFT).
The main feature of DFT consists in passing from solving the Schrödinger electronic problem with respect to the many-electron wave function $\psi_e(\mathbf{r}|\mathbf{R})$ to considering all the properties of the systems as unique functional of the ground state electron density $n(\mathbf{r})$. This provides an efficient and general method to treat the many-body electron-electron interaction potential. The fundamental of this approach lies in the first theorem of Hohenberg-Kohn (H-K) [25], which proves that, given a system of interacting electrons in an external potential $V_{ext}(\mathbf{r})$ (equivalent in our case to the nuclei electrostatic potential $\hat{V}_{e-n}$), there exist a one to one correspondence between the ground

[3]Because of the nucleus-electron difference in mass and the conservation of total linear momentum, the nuclei kinetic energy term $\hat{T}_n$ in (1.2) becomes negligible when one wants to evaluate its effect on electrons dynamics.

[4]The key point of the demonstration is that the nuclei coordinates act as parameters in the electron-nuclei potential: $\hat{V}_{e-n}(\mathbf{r}_i, \mathbf{R}_\alpha) \rightarrow \hat{V}_{e-n}(\mathbf{r}_i|\mathbf{R}_\alpha)$. [20]

state electron density $n(\mathbf{r}|\mathbf{R})$ and the external potential up to a trivial additive constant. Moreover, the second theorem of H-K [25] states that the ground state many-body wave function is a unique functional of the ground state electron density, valid for any number of particles and any external potential:

$$\psi_0 = \psi[n_0] \tag{1.9}$$

Therefore, any observable can be written as a density functional:

$$O[n] = \langle \psi[n] | \hat{O} | \psi[n] \rangle \tag{1.10}$$

and in particular the total electronic energy reads:

$$E[n] = \langle \psi[n] | \hat{H}_e | \psi[n] \rangle = F[n] + \int V_{e-n}(\mathbf{r}|\mathbf{R}) n(\mathbf{r}|\mathbf{R}) d\mathbf{r} \tag{1.11}$$

where $F[n] = \langle \psi[n] | \hat{T}_e + \hat{V}_{e-e} | \psi[n] \rangle$ is a universal functional, in the sense that it only depends on the nature of the electron-electron interaction potential.

From this remarkable result, using the variational principle (1.5), it follows that minimization of $E[n]$ with respect to variations of the density would determine the exact ground state density n_0 and ground state energy $E_0 = E[n_0]$.

At this point, it must be noted that the universal functional is unknown, because it depends on the nature of the interaction among particles.
The milestone Kohn and Sham (K-S) *ansatz* [36] comes to the rescue of this impasse, giving an approximation method[5] for treating an inhomogeneous system of interacting electrons. This *ansatz* states that, instead of solving the complex interacting problem, it is possible to consider a gas of non-interacting particles in an effective potential:

$$\hat{V}_{eff} = \hat{V}_{e-n} + \hat{V}_H + \hat{V}_{xc} \tag{1.12}$$

where the classical electron-electron Coulomb interaction is contained in the Hartree potential:

$$\hat{V}_H = \int \frac{n(\mathbf{r}')}{|\mathbf{r} - \mathbf{r}'|} d\mathbf{r}' \tag{1.13}$$

and all the non-trivial parts are recast in the exchange-correlation potential, defined as:

$$\hat{V}_{xc}(\mathbf{r}) = \frac{\partial E_{xc}[n]}{\partial n(\mathbf{r})} \tag{1.14}$$

This allows to rewrite the H-K functional (1.11) as follows:

$$E_{K-S}[n] = T_s[n] + \int \left\{ V_{ext}(\mathbf{r}) n + E_H[n] + E_{xc}[n] \right\} d\mathbf{r} \tag{1.15}$$

[5] The method is exact for systems of slowly varying or high density, but errors can occur due to rapid variation of density and boundary effects for finite systems. [36]

where T_s is the Kohn-Sham kinetic energy of the fictitious non-interacting system and E_{xc} is the unknown exchange-correlation energy term, which is assured to be an universal functional by the H-K theorems.
As a result, given an effective external potential, the electron density of the complex interacting system is found by the solution of an auxiliary one-electron Schrödinger equation, the Kohn-Sham equation:

$$\underbrace{\Big(-\frac{\hbar^2}{2m_e}\nabla^2 + \hat{V}_{eff}[n(\mathbf{r}|\mathbf{R})_i] \Big)}_{\hat{H}_e} \psi_i[n(\mathbf{r}|\mathbf{R})_i] = \varepsilon_i \psi_i[n(\mathbf{r}|\mathbf{R})_i] \tag{1.16}$$

According to the *Aufbau* principle, the electron density can be computed:

$$n(\mathbf{r}|\mathbf{R}) = \sum_i f_{FD}(\mu - \varepsilon_i)|\psi_i(\mathbf{r})|^2 \tag{1.17}$$

where f_{FD} is the Fermi-Dirac distribution and μ is the Fermi level.

These two equations are interdependent and they must be solved in a self-consistent way, as described in the following steps and schematised in fig. 1.1:

1) An initial guess is made for the electron density $n(\mathbf{r}|\mathbf{R})$

2) The effective potential is computed as function of the electron density

3) The K-S equation is solved for the given $\hat{V}_{eff}$

4) The final electron density is computed by averaging the square modulus of the eigenstates of the K-S equation, with weights given by the Fermi-Dirac distribution.

5) The new density is inserted in the energy functional (1.15), which must be minimized. If the difference between the evaluation of this functional for the initial and final density lies within an acceptable tolerance value δE, the ground state density has been found and all the properties can be computed as (1.10). Otherwise, a new configuration is obtained by mixing the two previously calculated densities and a new loop starts.

1.1.1 Exchange-Correlation Functional

In the previous section, the general structure of a DFT calculation, based on solving the K-S equation in a self-consistent way, was shown. What still needs clarification is the expression of the exchange-correlation (xc) potential (1.14), containing all the unknown terms which allow to handle the many-body problem by solving the much easier one-electron K-S equation. If the exact dependence of the exchange-correlation energy upon the electron density was known, this method would predict the exact ground-state energy and density of a many-electron system. In practice approximations are

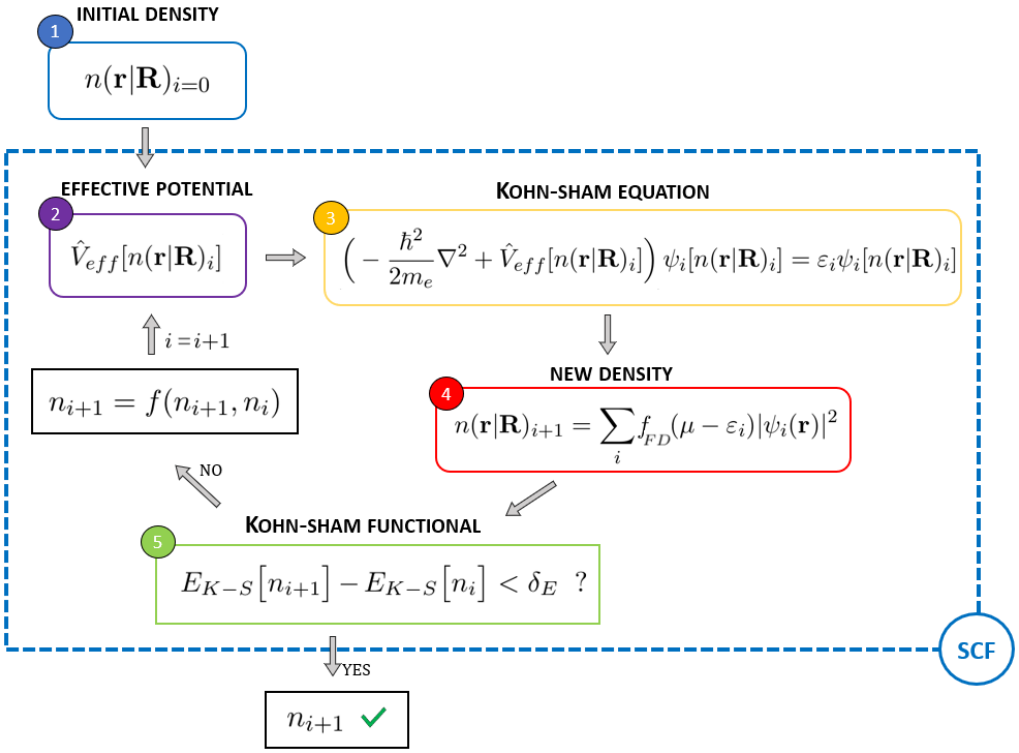

Figure 1.1: Flow diagram of the self-consistent field (SCF) procedure.

needed.
The most popular functionals have a form appropriate for slowly varying densities [58]: the local density approximation (LDA)

$$E_{xc}^{LDA} = \int n\epsilon_{xc}^{unif}(n)d\mathbf{r} \tag{1.18}$$

and the generalized gradient approximation (GGA)

$$E_{xc}^{GGA} = \int f(n, \nabla n)d\mathbf{r} \tag{1.19}$$

LDA approximation relies on the assumption that at each point in the system, the xc energy is given by the xc energy of an homogeneous electron gas with density equal to the local density [36]. While this model works well with some solids, it is problematic with localised charge distributions, due to the presence of defects.
An improvement is brought by the GGA, where the xc potential is a functional of the density and of the gradient of the density as well. In most cases it tends to overcompensate LDA [31, 58].
Other hybrid methods have been tried (for more details see reference [16]).
All the calculations that will be shown in this work have been performed under the generalized gradient approximation of Perdew, Burke and Ernzerhof [58]. The choice between GGA and LDA is solely based on the comparison with experimental results.

1.1.2 The Supercell Approach

Translational invariance in crystals allows to fully describe the properties of the whole system by considering only the unit cell subjected to Born-Von Karman periodic boundary conditions. However, one should be careful when dealing with defects, since their distribution in the material will result periodical as well.
For this reason, the primitive cell must be extended ("supercell approach") in such a way that, after a certain distance from the defect, the atoms will show the same spatial distribution of the pristine material and will feel the same forces.

A similar concept is at the base of the treatment of 2D materials too. In fact, *SIESTA* automatically applys periodic boundary conditions in the three dimensions of space. Since the third dimension is automatically considered also for 2D systems, the unit cell must include a vacuum region in the out of plane direction (fig. 1.2). This vacuum region should be large enough that periodic images, corresponding to adjacent replicas of the supercell, do not interact significantly.

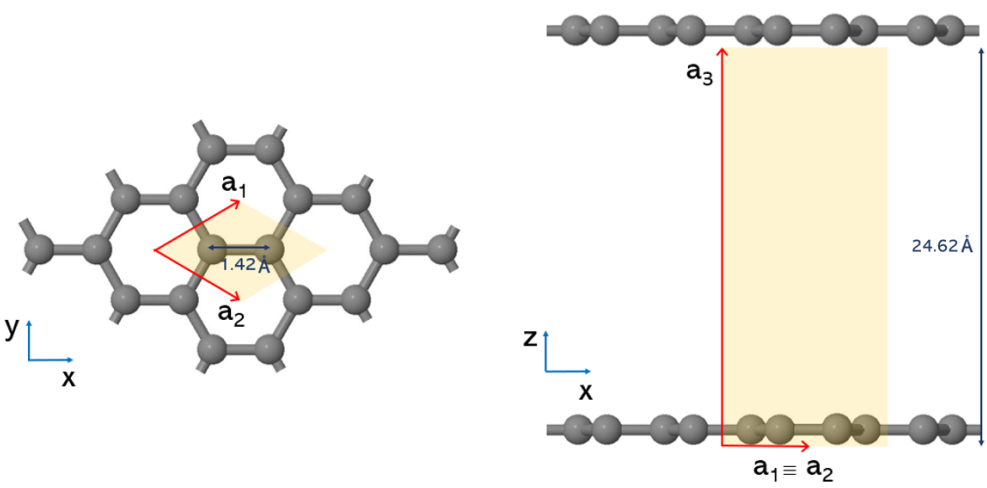

Figure 1.2: Representation of the unit cell of graphene for DFT calculation (yellow area). The top view (left) displays the usual primitive cell for graphene. The side view (right) shows instead the presence of a primitive vector in the out-of-plane direction, a_3, which is much longer than a_1 and a_2. Hence, this is a supercell in which the vacuum region is included to avoid interactions between the replicas of the graphene sheets along z that are a consequence of the periodic boundary conditions. If the vacuum was not be included, the system studied would be graphite.

1.1.3 Basis and Pseudopotentials

In order to solve the one particle Kohn-Sham equation 1.16, the eigenvectors must be expanded in terms of a basis made of an appropriate set of functions with known properties: $\psi_i(\mathbf{r}) = \sum_j c_{ij}\phi_j(\mathbf{r})$.

An expansion in a basis set of orthogonal plane waves, characterised by a wave vector $\mathbf{k}$, is one of the most convenient and used choices, which profits of the periodicity of the crystal via the Bloch's theorem:

$$\phi_{i,\mathbf{k}}(\mathbf{r}) = \sum_{\mathbf{q}} c_i(\mathbf{q}) \frac{1}{\sqrt{\Omega}} e^{i(\mathbf{k}+\mathbf{q})\cdot\mathbf{r}} \tag{1.20}$$

where the sum is extended over all the reciprocal lattice vectors $\mathbf{q}$ and the $c_i(\mathbf{q})$ are the expansion coefficients.
Many DFT methods use several different kinds of bases, like Augmented Plane Waves (APW), Muffin-Tin Orbitals (MTO), Gaussians, Slater type orbitals and others. Calculations in this thesis were performed with *SIESTA*, which uses localised atomic orbitals as basis set. This choice is valuable when dealing with interfaces, defects and in case of 2D systems, where many additional plane waves would be necessary to describe the vacuum.

The reason why plane waves methods are the most common is that they have the advantage of being asymptotically complete and allowing systematic convergence. However, a large number of plane waves per atom are needed to achieve a good accuracy. This affects the computation time, which for most codes scales as N^3, where N is the dimension of the basis.[5] Therefore, the expansion has to be truncated in such a way to include only plane waves with associated kinetic energy lower than a cutoff energy E_{cut}.

Furthermore, to reduce the computational cost, the rapid oscillations of the potential close to the nuclei are treated with pseudopotentials. The pseudopotential is an effective potential constructed to replace the atomic all-electron potential so that core states are eliminated and the valence electrons are described by pseudo-wavefunctions with significantly fewer nodes. This allows for the pseudo-wavefunctions to be described with far fewer Fourier modes, thus making plane-wave basis sets practical to use [16].
There are several kind of pseudopotentials. Methods based on plane waves usually employs ultra-soft pseudopotentials. Within *SIESTA*, norm-conserving pseudopotentials are used, which are characterised by the following desirable properties: [23]

1) Real and pseudo valence eigenvalues match for a chosen atomic configuration.

2) Real and pseudo atomic wave functions match beyond a chosen "core radius" r_c.

3) The integrals from 0 to r of the real and pseudo charge densities match for $r > r_c$, for each valence state (norm conservation).

4) The logarithmic derivatives of the real and pseudo wave function and their first energy derivatives agree for $r > r_c$.

Properties (3) and (4) are crucial for the pseudopotential to have optimum transferability among a variety of chemical environments.

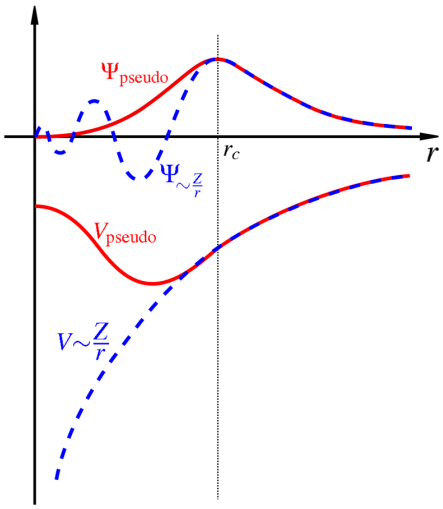

Figure 1.3: Comparison of a wavefunction in the Coulomb potential of the nucleus (blue) to the one in the pseudopotential (red). The real and the pseudo wavefunction and potentials match above a certain cut-off radius r_c. From https://en.wikipedia.org/wiki/Pseudopotential

Why *SIESTA*?

As mentioned above, methods based on plane waves are less efficient for 2D systems, where several additional basis functions are needed to reproduce the vacuum.
Moreover, for the systems studied in this thesis, the presence of defects breaks the perfect translational symmetry of the crystal, implying the need for a further extension of the basis set.
For these reasons, the *SIESTA* method was used. In fact, *SIESTA* is based on finite-support numerical atomic orbitals, i.e. numerical solution of the K-S hamiltonian for the isolated pseudo-atoms with the same approximations (xc functional, pseudopotential) as for the condensed system. [2, 32]
The basis functions are composed of an angular and a radial part:

$$\phi_{i,nlm}(\mathbf{r}) = R_{i,nl}(|\mathbf{r}|)Y_{i,lm}\left(\frac{\mathbf{r}}{|\mathbf{r}|}\right) \tag{1.21}$$

where Y are the well-known spherical harmonics and R a radial function that becomes 0 beyond a critical radius r_c.
Analytical operations are possible for the angular part, while for the radial terms they are performed in the reciprocal space using a finite mesh. [5]
In addition, Troullier-Martin norm-conserving pseudopotentials are employed. [71, 80]
This has the advantage to require a very small number of basis functions, resulting in reduction of CPU time and memory[6].

[6] *SIESTA* was also implemented to be an Order-N method [5], for which the computational load scales linearly with the system size. Since a large number of plane waves per atom are needed to achieve high accuracy, a plane wave basis set would be intrinsically inadequate for Order-N scaling.

The major drawback consists in a lack of systematic, since there is not a unique way to enlarge the basis set. [5, 30] As a consequence, physical understanding and convergence tests are necessary to search for a suitable basis set before focusing on a realistic project.
In fact, to model correctly the changes which occur to the electronic structure on formation of bonds in the condensed system, variational freedom for the valence electrons is required both for the radial and the angular parts. Thus, the following features have to be wisely chosen to optimize the efficiency-accuracy dichotomy: [2, 32]

- The size, i.e. the number of atomic orbitals per atom. The radial functions in a given angular momentum channel can be increased (known as multiple zeta), so that one radial channel is notated Sζ ("double-zeta") and two radial channels Dζ ("double-zeta").
  Moreover, angular flexibility is obtained by adding shells of higher angular momentum than the valence states, resulting in the so-called polarized atomic orbitals. Another way to obtain polarized orbitals is to apply a small electric field. [71]

- The range of the radial function, which depends on the critical radius r_c. A strict localization of the basis functions is ensured either by imposing a boundary condition, by adding a confining (divergent) potential, or by multiplying the free-atom orbital by a cutting function. [32]
  It is worth to note again that the localized extension of the radial part results in a remarkable reduction of the computational time. In particular, the numerical cost to deal with the vacuum surrounding 2D systems becomes almost free with this basis choice.

- The radial shape, which must keep the consistency between the pseudopotential and the form of the pseudoatomic orbitals in the core region. This is done by using as basis the orbitals coming from the solutions of the same pseudopotential in the free atom. The shape of the orbitals at larger radii depends on the cutoff radius (see above) and on the way the localization is enforced. [32]

The optimizations of pseudopotentials and basis parameters were performed by Christophe Adessi. The electronic band structure and the phonon dispersion relation of MoS_2, which were computed in this thesis with *SIESTA*, were compared with calculations performed by Silvana Radescu[7] using the *VASP* package, which is based on plane waves. The match between the calculations testified the reliability of the analysis performed in this work with *SIESTA*.

[7] Private communication

1.2 Structure Optimization and Electronic Band Structure Calculation

At this point, the process to optimize the input structure of the unit cell will be discussed. The key point consists in varying the location of the nuclei in the lattice in order to minimize the energy functional (1.15) with respect to the nuclei positions.
The procedure consists in the following steps:

1) By virtue of the Bloch's theorem, the starting input consists only in the data of the unit cell structure, which is built knowing the chemical composition of the system (types and number of atoms) and from a rough enough knowledge of the nuclei positions in the lattice[8].

2) A self-consistent field step is performed. As a result, $n_0(\mathbf{r}|\mathbf{R}_i)$, $\hat{H}_e(n_0)$, $E_{K-S}[n_0]$ are known for the given set of nuclei positions $\mathbf{R}_i$.

3) According to the Hellman-Feynman theorem [15], the atomic forces and stresses are obtained by direct differentiation of the energy expression:

$$\mathbf{F_I} = -\frac{\partial E_{K-S}}{\partial \mathbf{R}_I} \tag{1.22}$$

$$\sigma_{\alpha\beta} = \frac{\partial E_{K-S}}{\partial \epsilon_{\alpha\beta}} \tag{1.23}$$

where the subscript I stands for the I-th nucleus and $\epsilon_{\alpha\beta}$ are the strain tensor elements.

4) The values of the atomic forces and the stresses are compared to tolerance values (typically $F^* = 10^{-4}$ eV/$\mathring{A}$ for the forces and $\sigma^* = 0.1$ MPa for the stresses). If they are greater than the tolerance values, a Conjugate Gradient (CG) iteration starts as described at point 5. Otherwise the given configuration corresponds to the optimized structure.

5) The CG method is a technique that allows to update all the nuclei position simultaneously. This is done by moving the atoms along the direction of an energy gradient which is constructed to be conjugate to the directions of all the previous iterations. The convergence to the energy minimum employing the CG method is much more rapid than using the simpler Steepest Descent approach, for which atoms are moved along the local steepest gradient.[54, 67]
Once obtained a new set of coordinates $\mathbf{R}_{i+1}$, another iteration starts from point 2).

[8] These data can come from literature, experimental results or previous calculations. It should be noted that an ideal perfectly symmetrical arrangement of the atoms does not correspond to the minimum of the energy functional. This is related to the intrinsic error due to the discretization of the space in numerical calculations ("eggbox effect"). Therefore, structure optimization is always required with a target accuracy so that the eggbox effect becomes negligible.

The procedure described above is outlined in fig. 1.4.

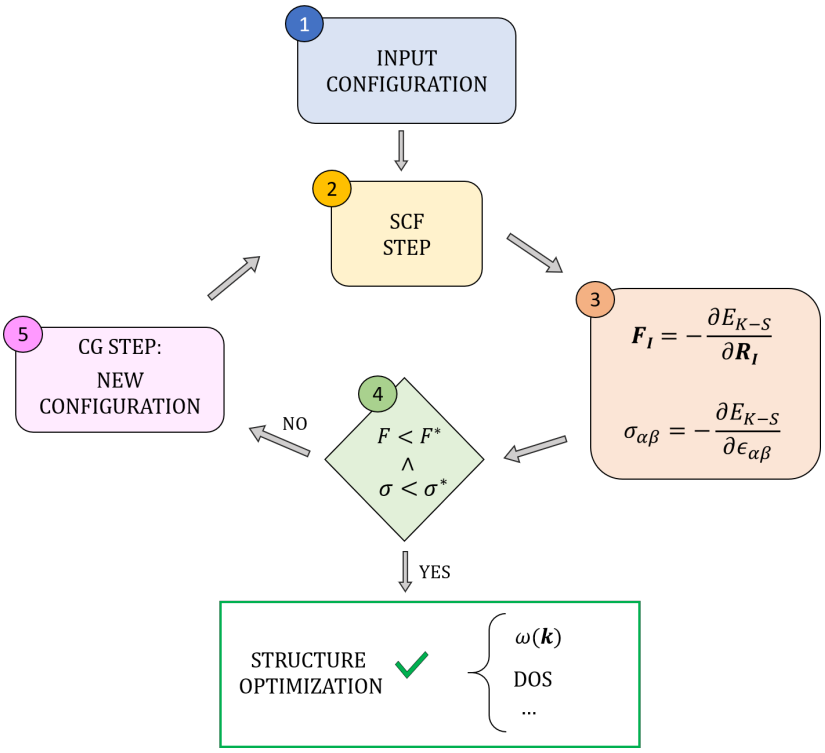

Figure 1.4: Flow diagram of the procedure to optimize the structure of the unit cell.

The Monkhorst-Pack scheme [45] is used to set the mesh-grid to compute quantities in the reciprocal space. For solving integrals in direct space the mesh is specified by an energy cutoff value. The number of k-points and the energy cutoff have been chosen in order to obtain a full convergence of the calculations (typically 10x1x10 k-points and 600 Ry, respectively). Technical details on the simulation parameters can be found on the *SIESTA User's Guide*, available on the official webpage of *SIESTA* [9].

At the end of this structure relaxation phase, the ground state electronic Hamiltonian $\hat{H}_e$ of the system is known with accuracy. By diagonalization of $\hat{H}_e$, *SIESTA* provides the electronic band structure, the density of states (DOS) and the projected density of states (PDOS)[10].

[9] https://departments.icmab.es/leem/siesta/Documentation/Manuals/siesta-4.0.pdf

[10] The projected density of states gives information on the contribution to the DOS of the states of each atom of the basis. It does not have to be confused with the phonon density of states.

1.3 Calculation of the Phonon Dispersion Relation

This section is devoted to the calculation of the phonon dispersion relation, which is the starting point to derive the thermal transport properties within the Landauer Formalism.

Previously it was demonstrated how to obtain the electronic ground state density, $n(\mathbf{r}|\mathbf{R})$ related to a fixed ionic configuration $\mathbf{R}$. A key point in the derivation consisted in the separation of the electronic and nuclei problems thanks to the adiabatic approximation, which allows to consider the electrons in their ground state for any instantaneous ionic configuration.
In crystals, the atoms are not frozen and they move around their mean equilibrium positions $\mathbf{R}_k^a$ with displacements $u_{k\alpha}^a$, where a and k are the labels of unit cells and atoms of the basis respectively, $\alpha = x, y, z$ is one of the three cartesian directions (see fig. 1.5).

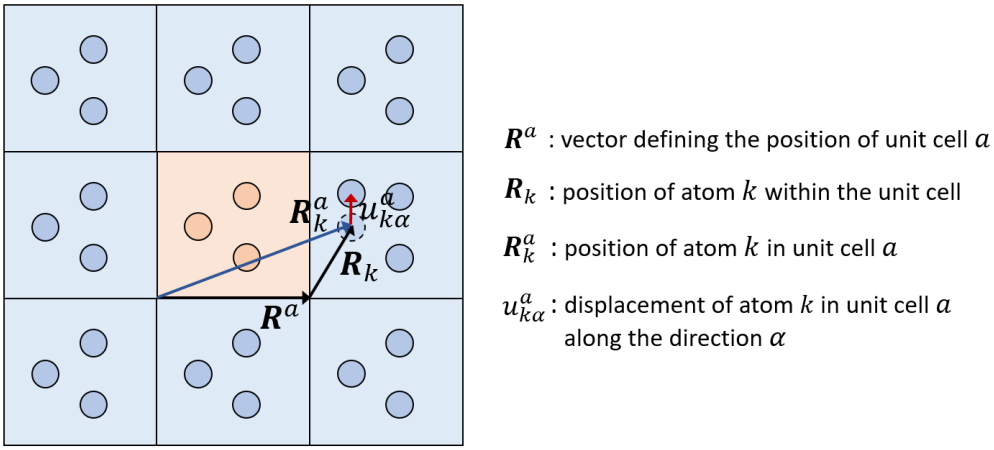

Figure 1.5: Representation of atom displacement in a generic lattice. The central orange cell is the unit cell of reference. The ensemble of the nine cells, orange and blue, constitutes a 3x3 supercell for phonon calculation.

The interactions among ions of the lattice are treated as a system of coupled oscillators with a total potential energy E_{tot}, which includes nuclear and electronic contributions (see eq. 1.8). With small displacements at constant volume, the problem of atomic vibrations can be solved in harmonic approximation, expanding the potential around the equilibrium position and arresting the expansion at second order:

$$E_{tot}^{harm}\left(\{\mathbf{R}_k^a(t)\}\right) \approx E_{tot}\left(\{\mathbf{R}_k^a\}\right) + \sum_{ak\alpha}\sum_{bk'\beta}\frac{1}{2}\left(\frac{\partial^2 E_{tot}}{\partial u_{k\alpha}^a \partial u_{k'\beta}^b}\right)u_{k\alpha}^a u_{k'\beta}^b \qquad (1.24)$$

The second derivatives of the energy coupling constants are defined as the

interatomic force constants:

$$C_{k\alpha,k'\beta} = \left(\frac{\partial^2 E_{tot}}{\partial u^a_{k\alpha} \partial u^b_{k'\beta}} \right) \tag{1.25}$$

They must satisfy a number of conditions that arise from

- isotropy of space
- point group symmetry
- translation invariance upon displacement of the lattice by an arbitrary lattice constant

From this last property it follows that the second derivative of the energy can only depend on the distance between cells a and b:

$$\frac{\partial^2 E_{tot}}{\partial u^a_{k\alpha} \partial u^b_{k'\beta}} = \frac{\partial^2 E_{tot}}{\partial u^0_{k\alpha} \partial u^{b-a}_{k'\beta}} \tag{1.26}$$

The motion of the ions is ruled by classical Newton's equations:

$$\begin{aligned} M_k \frac{\partial^2 u^a_{k\alpha}}{\partial t^2} &= -\frac{E^{harm}_{tot}}{\partial u^a_{k\alpha}} \\ &= -\sum_{bk'\beta} \left(\frac{\partial^2 E_{tot}}{\partial u^a_{k\alpha} \partial u^b_{k'\beta}} \right) u^b_{k'\beta} \end{aligned} \tag{1.27}$$

For each atom there are three equations of motion of this type, one for each cartesian direction. These equations are coupled. In order to know the displacement of atom k, in unit cell a, along cartesian direction $u^a_{k\alpha}$, it is required the displacement of atom k', in unit cell b, along cartesian direction $u^b_{k'\beta}$.

In order to solve the system a first *ansatz* is introduced regarding the temporal dependency of all the displacements. Hence, one seeks for general solutions of the form $e^{-i\omega_\lambda t}$, being λ the index of mode:

$$u^a_{k\alpha}(t) = \eta^a_\lambda(k\alpha) e^{-i\omega_\lambda t} \tag{1.28}$$

For periodic structures, it is possible to write the displacements in terms of a plane wave with respect to cell coordinates[11]:

$$u^a_{k\alpha}(t) = \eta_{\lambda\mathbf{q}}(k\alpha)\ e^{i\mathbf{q}\cdot\mathbf{R}_a}\ e^{-i\omega_{\lambda\mathbf{q}} t} \tag{1.29}$$

In contrast to a normal plane wave, this wave is only defined at the lattice points.

[11] In order to avoid a confusion with the notation of the atoms of the basis, the reciprocal space vectors will be denoted by $\mathbf{q}$

$\eta_{\lambda\mathbf{q}}(k\alpha)$ is the component along direction α of a vector called the polarization vector of the normal mode.
Inserting the *ansatz* solution in the equation of motion 1.27, and considering the translation invariance for the interatomic force constants, leads to :

$$M_k\ \omega^2_{\lambda\mathbf{q}}\ \eta_{\lambda\mathbf{q}}(k\alpha) = \sum_{k'\beta}\left[\sum_b C_{k\alpha,k'\beta}(0,b)\ e^{i\mathbf{q}\cdot\mathbf{R}_b}\right]\eta_{\lambda\mathbf{q}}(k'\beta) \tag{1.30}$$

The term in brackets is the discrete Fourier transform of the interatomic force constant in real space. Therefore, the movement of the atoms can be defined in terms of the following dynamical equation:

$$M_k\ \omega^2_{\lambda\mathbf{q}}\ \eta_{\lambda\mathbf{q}}(k\alpha) = \sum_{k'\beta}\tilde{C}_{k\alpha,k'\beta}(\mathbf{q})\ \eta_{\lambda\mathbf{q}}(k'\beta) \tag{1.31}$$

For each $\mathbf{q}$ vector, we have a linear homogeneous system of equations.
We can recover a standard eigenvalue problem redefining the displacements in eq. 1.29 by incorporating the square root of the mass:

$$u^a_{k\alpha}(t) = \frac{1}{\sqrt{M_k}}\gamma_{\lambda\mathbf{q}}(k\alpha)\ e^{i\mathbf{q}\cdot\mathbf{R}_a}\ e^{-i\omega_{\lambda\mathbf{q}}t} \tag{1.32}$$

In this way, the dynamical equation reduces to:

$$\sum_{k'\beta}\tilde{D}_{k\alpha,k'\beta}(\mathbf{q})\ \gamma_{m\mathbf{q}}(k'\beta) = \omega^2_{\lambda\mathbf{q}}\ \gamma_{\lambda\mathbf{q}}(k\alpha) \tag{1.33}$$

where the dynamical matrix is defined as:

$$\begin{aligned}\tilde{D}_{k\alpha,k'\beta}(\mathbf{q}) &= \frac{1}{\sqrt{M_k M_{k'}}}\tilde{C}_{k\alpha,k'\beta}(\mathbf{q}) \\ &= \frac{1}{\sqrt{M_k M_{k'}}}\left[\sum_b C_{k\alpha,k'\beta}(0,b)\ e^{i\mathbf{q}\cdot\mathbf{R}_b}\right]\end{aligned} \tag{1.34}$$

In matrix form:

$$\begin{array}{cccc}\left[\tilde{D}(\mathbf{q})\right] & \left(\gamma(\mathbf{q})\right) & = & \omega^2(\mathbf{q}) \qquad \left(\gamma(\mathbf{q})\right) \\ \text{Dynamical} & \text{Phonon} & & \text{Phonon} \quad \text{Phonon} \\ \text{matrix} & \text{eigenvectors} & & \text{frequencies} \quad \text{eigenvectors} \\ (3N_b \times 3N_b) & (1 \times 3N_b) & & (1 \times 3N_b)\end{array}$$

The dynamical matrix represents the key quantity in the computation of phonon properties. Through its diagonalization the phonon eigenfrequencies and eigenvectors are found.
From eq. 1.34, it is possible to compute the dynamical matrix for every q-point knowing the force constants matrix in real space, which reads:

$$C_{k\alpha,k'\beta}(0,b) = \left(\frac{\partial^2 E_{tot}}{\partial u^0_{k\alpha}\partial u^b_{k'\beta}}\right) = -\frac{\partial F^b_{k'\beta}}{\partial u^0_{k\alpha}} \tag{1.35}$$

The forces acting on each atom when they are all in their equilibrium position is known by the standard calculation of the electronic hamiltonian and electronic density via the procedure explained in the previous section.
The force constants are computed using a simple finite difference formula. Hence, to find the interatomic force constant $C_{k\alpha,k'\beta}(0,b)$, one has to displace the atom k in the unit cell 0 along direction α, and repeat the SCF procedure for the displaced atomic configuration. From the new electronic density, the forces acting on each atom are computed. Finally, the derivative in eq. 1.35 is computed by finite differences, allowing to evaluate how the force on atom k' in unit cell b along direction β changes upon the displacement $u^0_{k\alpha}$.

1.3.1 Supercell for Phonon Calculation

In principle, the atoms in the unit cell 0 should be displaced one by one in all the three cartesian directions to account for variations in the forces with all the atom of the crystal. From a practical point of view, the values of the force constants matrix in real space decay with the distance between the atoms. Hence, the sum over b in eq. 1.34 can include only a given number of distant neighbours.
This is done by defining a supercell through the repetition of the primitive cell to create adjacent replicas. All the distant neighbours, with no negligible forces with the central primitive cell, must be included (see fig. 1.5). The range in real space in which the force constants matrix decays to zero varies widely from system to system, depending on the structure of the unit cell. This is why the size of the supercell used will be indicated for each system studied in the *Results* part.
Provided that the main time cost for running DFT calculations is associated to the SCF procedure, which scales with the number of atoms of the systems, it follows that a phonon calculation is much more time demanding because it requires the use of a supercell. This supercell is different from the one mentioned in section 1.1.2, when speaking about the optimization of the unit cell in presence of defects. The study of phonons in systems with defects requires in fact a "supercell of the supercell" (see fig. 1.6). As a consequence, calculations become very time demanding when studying systems with defects. Furthermore, a supercell built for dealing with a realistic disordered distribution of defects would consist of millions of atoms, making any calculation impracticable. For these systems it is necessary to use the Green's function technique, which will be introduced in the next chapter. An analysis including disorder is presented in Ch. 5.2.
The procedure for computing the phonon dispersion is implemented within *SIESTA* in a suite called *VIBRA* [51]. In the next chapter it will be explained how to start from the dispersion relation to obtain the phonon transport properties of the system, namely lattice thermal conductance.
All transport calculations performed in the team relies on codes developed by Christophe Adessi, which are based on the *VIBRA* codes, but add further

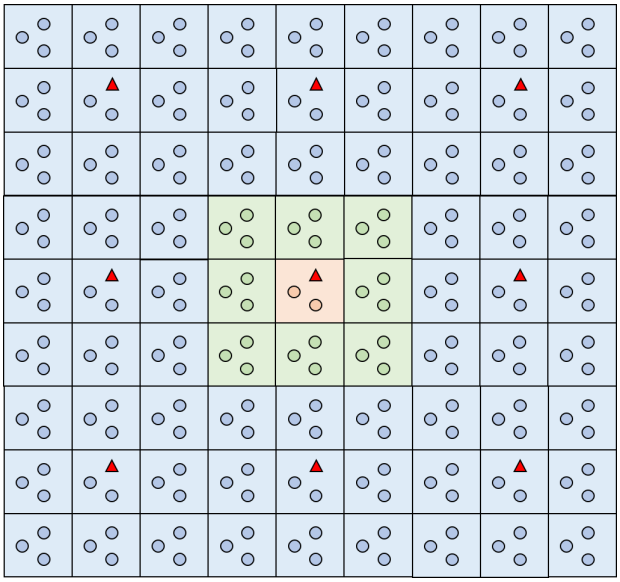

Figure 1.6: Example of the supercell needed to compute the phonon dispersion of systems whose unit cell includes a defect (red triangle). The orange + green cells represent the supercell necessary to compute the electrical transport properties; namely it is equivalent to the unit cell of the Structure Optimization procedure in the case of no defects. The ensemble of orange + green + blue cells is instead the supercell required for phonon calculations ("supercell of the supercell").

routines such as the one to compute the transmission within the Landauer formalism.
During my internship I have learnt how to use the open source package for phonon calculation *PHONOPY* [75, 77]. This software contains functions that are not implemented in *VIBRA* and which turned out to be useful for the evaluation of phonon-phonon inelastic scattering. One disadvantage is the need to interface it with *SIESTA*.
My work consisted in understanding how to use a combination of *SIESTA* for the DFT calculation and of *PHONOPY* to compute quantities such as phonon group velocities and the Grüneisen parameter (more information will be provided in Ch. 3 and 6).

Chapter 2

Transport of Electrons and Phonons at the Mesoscopic Scale: The Landauer Formalism

2.1 Relevant Length Scales

In order to study the thermoelectric properties of a material, the charge and heat transport phenomena must be investigated. Different models are available to describe the transport mechanisms and refer to different regimes. Important features of these transport regimes can be understood by comparing the length scales of the carriers with the device dimension.

Concerning electron transport, the relevant length scales are the following [44]:

- The De Broglie wavelength λ_{DB}, which in a semiconductor with effective mass m^* is defined as:
$$\lambda_{DB} = \frac{2\pi\hbar}{\sqrt{2m^*E}} \tag{2.1}$$

- The mean free path of the electrons between two elastic collisions Λ_{el}. Elastic scattering is due to collisions with static defects. An essential property of an elastic collision is that it changes the momentum k of the carrier, but does not destroy its phase. Therefore the quantum coherence of the electron motion is maintained.

- The mean free path between two inelastic collisions Λ_{in}.
Inelastic scattering is associated to dynamics alteration of the the perfect periodicity of the lattice. It is the case of electron-phonon scattering and electron-electron scattering. These processes change the momentum of the carriers and introduce a random phase.
Hence, inelastic collisions destroy the coherence of the electron motion.

An analogous classification is provided for phonons, whose wavelength is:

$$\lambda_{ph} = \frac{2\pi\, v_g}{\omega} \tag{2.2}$$

where $v_g = \frac{d\omega(q)}{q}$ is the phonon group velocity.
Also phonons may lose their phase after inelastic scattering events, such as Umklapp phonon-phonon scattering, phonon-impurity scattering and diffusive phonon-boundary scattering. These scattering mechanisms are said "incoherent ", in contrast to "coherent scattering " like phonon-phonon Normal scattering in which the phase is preserved[1]. Most of the conventional approaches to reduce thermal conductivity, such as introduction of rough surface and impurity scatterings, are based mainly on incoherent mechanisms by shortening the mean free path of phonons [92].
These lengths characterising the motion of the carriers, must be compared with the sizes of system. If the sizes of the system are macroscopic ($L >> \Lambda_{in}$), the transport will be diffusive, due to the presence of both elastic and inelastic scattering mechanisms. This case corresponds to the *classic regime*, in which charge and heat conduction are effectively described by Ohm's and Fourier's law respectively.
Diversely, if the system dimensions are comparable to λ_{DB} and λ_{ph}, quantum mechanical effects, like tunneling, arise. This is the *quantum regime*.
The intermediate regime, for which $\Lambda_{in} > L > \lambda_{DB}$, is called *mesoscopic regime*.

Furthermore, in the case where no scattering events occur during the transport ($L << \Lambda_{in}$), the regime is called *ballistic*, otherwise it is *diffusive*.
Diffusive transport has been often described by the Boltzmann transport equation (BTE) and simplifications of it, such as drift-diffusion equation for electrons or Fourier's Law for phonons [27].
A physically insightful description of ballistic transport is provided by the Landauer approach, which has been widely used to describe quantized electrical and thermal transport in nanostructures. Moreover, it is nowadays well recognised that the Landauer approach describes diffusive transport as well and provides a simple way to treat the ballistic to diffusive transition [27].

This chapter is devoted to the study of electrons and phonons transport at the mesoscopic scale based on the Landauer approach. This formalism will be introduced following as guideline the description made by S. Datta in the book "Quantum Transport: Atom to Transistor" (ref. [11]).
The dissertation will be divided in two parts: the first will focus on the calculation of the electrical conductance and the second on the thermal conductance. The transport of phonons will be treated in analogy with the formalism developed for electrons.

[1] Phonon scattering phenomena will be treated in Ch. 3

2.2 Electronic Transport

2.2.1 Ballistic Transport in Small Dimensional Conductors: Failure of the Ohm's Law

What is the electrical conductance G of a wire if the contacts were perfect and its length is reduced to very small dimensions? Based on Ohm's law, one may reply that the conductance will increase indefinitely as the length of the wire is reduced, since the conductance is inversely proportional to the length:

$$\begin{aligned} I &= GV \\ G &= \frac{1}{R} = \sigma \frac{A}{l} \end{aligned} \tag{2.3}$$

where l and A are the length and the section of the wire respectively and σ is the electrical conductivity, which is an intrinsic property of the material. Instead, it has been established experimentally [82] that, once the length of a wire has been reduced sufficiently that an electron can cross the wire without an appreciable chance of scattering (ballistic transport regime), the conductance will approach a maximum value given by:

$$G = G_0 \; M(E)|_{E=E_f} \tag{2.4}$$

where G_0 is a fundamental constant given by $G_0 = q^2/h = 38.7\mu\text{S}$ and $M(E)$ expresses the number of conductive modes, or subbands, at an energy E. The meaning of $M(E)$ will be deepen soon.
This behaviour proves that, at the mesoscopic scale, a quantum mechanical treatment is necessary and that Ohm's laws are only valid when the dimensions of the conductive channel are much greater than the length characterising the inelastic scattering processes, Λ_{in} [44].

2.2.2 Conductive Modes

The general setup for the study the transport properties within the Landauer framework is schematised in figure 2.2.
The sample of the studied material is often called *device* and it is represented by a channel between two contacts. The contacts, or *leads*, are semi-infinite perfect conductors, acting as charge reservoirs. When a positive potential is applied at the right lead, the electrons are injected into the device from the left lead and collected by the right lead.
The scheme is similar to the structure of a field effect transistor (FET), where the left and right leads are called source and drain respectively and the channel is sandwiched between an insulator that is attached to the gate contact.

In this thesis, the transport direction coincides with the z axis. The device is characterised by a length L_z, a width L_x, perpendicular to the transport

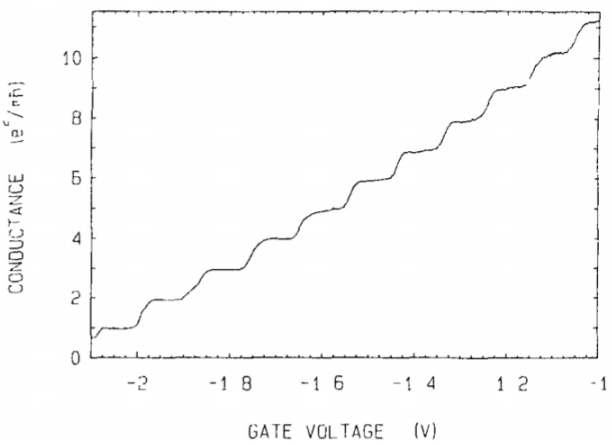

Figure 2.1: In [82], ballistic point contacts, defined in the two-dimensional electron gas of a GaAs-AlGaAs heterostructure, have been studied in zero magnetic field. The conductance changes in quantized steps of $2G_0$ when the width, controlled by a gate on top of heterojunction, is varied. Up to sixteen steps are observed when the point contact is widened from 0 to 360 nm. An explanation was proposed, which assumes quantized transverse momentum in the point-contact region.
The figure shows the point-contact conductance as a function of gate voltage at 0.6K. The conductance presents plateaus at multiples of $2q^2/h$. From ref. [82].

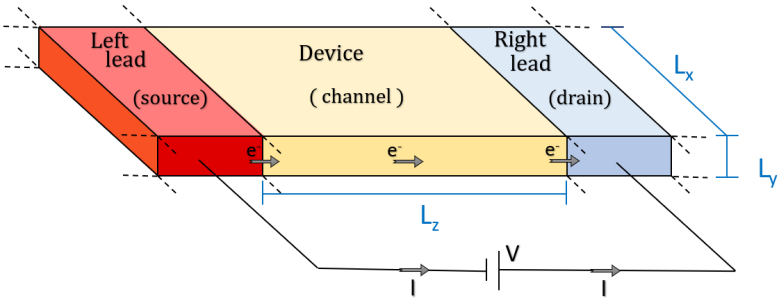

Figure 2.2: General scheme of a system treated within the Landauer Formalism. The sample to study (or device) is represented by a channel between two perfect semi-infinite metallic contacts (also called "leads").

direction, and a thickness L_y. In 2D materials, the channel has the thickness of few atomic layers, so that:

$$L_y \approx \text{nm} << L_z, L_x \approx \mu\text{m}$$

In the case of ballistic transport, L_z and L_x are short as well ($L_{z,x} << \Lambda_{in}$), but since electrons can flow in and out the contacts, a bulk description can still be used by applying cyclic periodic boundary conditions.
Therefore, the electronic band structure in the channel is described by a dispersion relation of the kind $E(k_x, k_y, k_z)$, with k_z and k_y ranging continuously in the first Brillouin Zone and with k_y assuming quantised values depending on the integer number n_y

$$k_y = \frac{2\pi}{L_y} n_y$$

Such a system can be described as a quantum well where electrons are free to move in the z-x plane and they are confined in the y direction. Hence, the band structure for the channel displays 1D subbands, each having a 2D dispersion relation E(k_z,k_x).
Within effective mass approximation, the dispersion relation close to the bottom of the conduction band reads

$$E_{n_y}(k_z, k_x) = E_c + n_y^2 \varepsilon_y + \frac{\hbar^2(k_x^2 + k_y^2)}{2m^*}, \tag{2.5}$$

with

$$\varepsilon_y = \frac{\hbar^2 \pi^2}{2m^* L_y^2} \tag{2.6}$$

A representation of this subbands scheme is shown in fig. 2.3.
The key point is that each subband represents a conductive channel and each of these gives a contribution equal to $2G_0$ to the total conductance [2].

The minimum spacing between two subbands is given by ε_y and it increases quadratically with decreasing thickness of the device L_y. In the case of 2D materials, made of few atomic layers, L_y has the dimension of few angstroms. Hence, the spacing between two subbands is very big and only the first subband ($n_y = 1$) is usually occupied by electrons, while the bands corresponding to $n_y > 1$ are much higher in energy than the Fermi level [3].

One has to notice that this "subbands scheme" occurs in correspondence of every valley in the first BZ, since each local minimum in the band structure

[2] The factor 2 is due to the spin degeneracy of each subband.

[3] In this thesis, the materials studied are graphene and monolayer TMDCs. They are pure 2D systems made of a single-plane of atomic thickness L_y (1 atomic layer for graphene and 3 atomic layers for TMDCs), but a 2D Brillouin zone, with the only k_x and k_y as reciprocal vectors. This is mathematically equivalent to consider an infinite spacing between two subbands, so that only the first one can be occupied. This approach is useful to understand the concept of subbands and to extend this procedure to few layers systems.

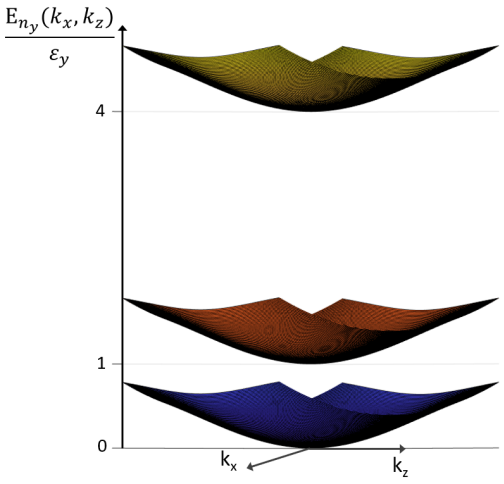

Figure 2.3: Graphical representation of the first three subbands ($n_y = 1, 2, 3$) given by the dispersion relation of eq. 2.5 (E_c set to zero).

can be approximated by a parabolic dispersion relation. For this reason, also in the limit of single-layer materials, many different subbands could be occupied.
Therefore, a full band-treatment is necessary when the studied material present a complex dispersion relation, with many local minima close in energy.

2.2.3 A Single Level Model

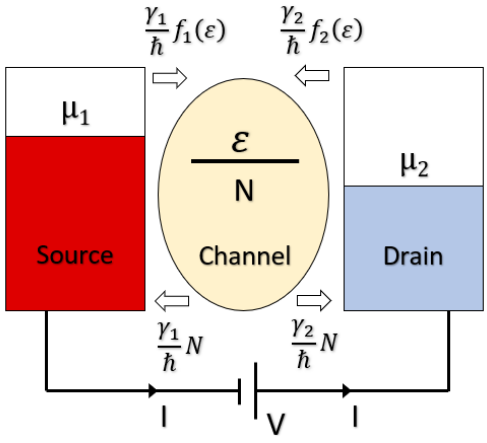

Figure 2.4: Flux of electrons into and out of a one level channel at the source and drain ends.

At this point, the electronic transport will be investigated for a simplified model in which the device has a band structure with a single conduction subband.
An external battery lowers the energy levels in the drain with respect to the

source, such that a constant difference in electrochemical potential is kept between the two leads:

$$\mu_1 - \mu_2 = eV \tag{2.7}$$

Being both the initial electrochemical potentials equal to μ_0, after the applied bias they are:

$$\begin{aligned} \mu_1 &= \mu_0 + \tfrac{eV}{2} \\ \mu_2 &= \mu_0 - \tfrac{eV}{2} \end{aligned} \tag{2.8}$$

For this specific non-equilibrium problem, it is assumed that the two contacts are such large systems that they cannot be driven out of equilibrium. Thus, each lead remains in local equilibrium with its electrochemical potential. As a consequence, the contacts display two different Fermi-Dirac distributions:

$$\begin{aligned} f_1(E) &= f_{FD}(E-\mu_1) = 1/\left[1+\exp\left(\tfrac{E-\mu_1}{k_BT}\right)\right] \\ f_2(E) &= f_{FD}(E-\mu_1) = 1/\left[1+\exp\left(\tfrac{E-\mu_2}{k_BT}\right)\right] \end{aligned} \tag{2.9}$$

The channel is forced into a balancing act between the two reservoirs. Considering the "one level system" in fig. 2.4, ε is the energy of the single state which lies in between the electrochemical potentials of the two leads and N is the average number of electrons in the device at the steady state. N is expected to be in between $f_1(\varepsilon)$ and $f_2(\varepsilon)$ [4]. It is possible to write the net fluxes across the left junction:

$$I_1(\varepsilon) = \frac{q\gamma_1}{\hbar}(f_1(\varepsilon) - N), \tag{2.10}$$

and the right junction:

$$I_2(\varepsilon) = \frac{q\gamma_2}{\hbar}(f_2(\varepsilon) - N) \tag{2.11}$$

The fluxes are proportional to the difference between the Fermi-Dirac distribution at ε of the lead and N.
$\gamma_1/\hbar$ and $\gamma_2/\hbar$ are the rates at which an electron occupying the level ε in the device will escape into the source and drain contacts respectively. γ_1 and γ_2 have the dimension of an energy and they are linked to the energy coupling of the level in the device and the leads.
At the steady state there is not a net flux ($I_1 + I_2 = 0$). It follows that the average number of electrons in the device is:

$$N = \frac{\gamma_1 f_1(\varepsilon) + \gamma_2 f_2(\varepsilon)}{\gamma_1 + \gamma_2}, \tag{2.12}$$

which is a weight average of the Fermi-Dirac distributions of the leads, with the weights given by the rates.
The steady state current is:

$$I(\varepsilon) = I_1 = -I_2 = \frac{2q}{\hbar}\frac{\gamma_1\gamma_2}{\gamma_1+\gamma_2}[f_1(\varepsilon) - f_2(\varepsilon)], \tag{2.13}$$

[4] Because of the Pauli principle and without considering the spin degeneracy, only one electron can occupy the single energy state in the device.

where the factor 2 comes from including the spin degeneracy.
The flow of a current is the result of the difference in Fermi distribution between the leads. It is also clear that the process of conduction requires the presence of states in between the electrochemical potentials of the leads. For fully periodic systems (no defects), the couplings between the device and both the leads can be considered the same, $\gamma_1 = \gamma_2 = \gamma^\star$. Equation 2.13 reduces to:

$$I(\varepsilon) = \frac{q\gamma^\star}{\hbar}[f_1(\varepsilon) - f_2(\varepsilon)] \tag{2.14}$$

In this case one could expect the conductance to increase indefinitely with the energy coupling, since the current is proportional to $\gamma^\star$. This is not in agreement with what was found experimentally and the reason lies in the broadening of the energy level when coupled with the leads.

2.2.4 Broadening of the Energy Level

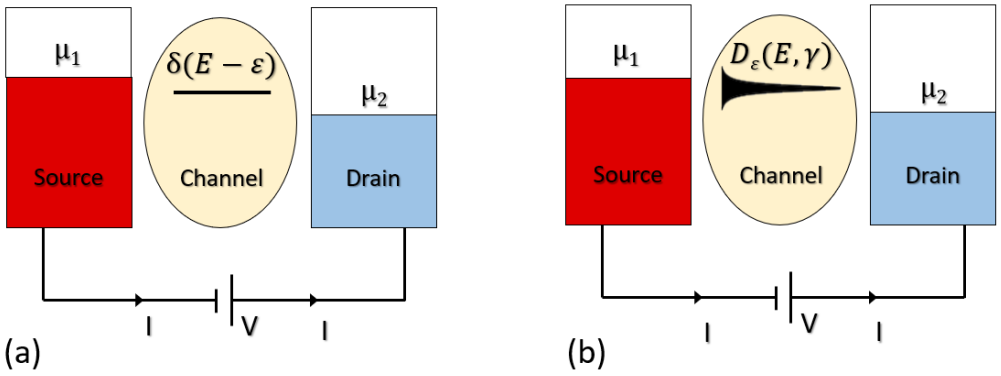

Figure 2.5: (a) A single level system with $\mu_1 > \varepsilon > \mu_2$. The density of state in the device corresponds to a Dirac delta. (b) The process of coupling to the channel broadens the energy level. The broadened DOS is represented by a Lorentzian function centred in ϵ and of width γ.

The broadened DOS could in principle have any shape, but in the simplest situation it is described by a Lorentzian function of unitary area and centred in $E = \varepsilon$:

$$D_\varepsilon(E) = \frac{\gamma/2\pi}{(E-\varepsilon)^2 + (\gamma/2)^2} \tag{2.15}$$

The width of this Lorentzian is equal to the broadening γ. It turns out that $\gamma = \gamma_1 + \gamma_2$ [5].
The single "sharp" state can be found from 2.15 in the limit $\gamma \to 0$, i.e in absence of couplings:

$$D_\varepsilon(E) \xrightarrow[\gamma\to 0]{} \delta(E-\varepsilon) \tag{2.16}$$

[5]This results from a quantum mechanical treatment where γ_1 and γ_2 represent the coupling Hamiltonians of the device with source and drain respectively (Ch. 8 of reference [11]).

Hence, the expression of the current of eq. 2.13 has to be modified to account for the broadened density of states. By integration over $D_\varepsilon(E)dE$, it results:

$$I = \frac{2q}{\hbar}\int_{-\infty}^{+\infty} dE \underbrace{D_\varepsilon\,(E)\frac{\gamma_1\gamma_2}{\gamma_1+\gamma_2}}_{\bar{T}(E)}\,[f_1(E)-f_2(E)] \tag{2.17}$$

This expression is exact and it can be solved once the coupling energies and the DOS related to the broadening of the single level ε are known.
$\bar{T}(E)$ is the transmission, the key quantity of the Landauer formalism, which will be extensively investigated. It is often thought as the probability of an electron to be transmitted from source to drain and it contains the dependence on the band structure of the device and on the couplings with the contacts.

2.2.5 Linear Response Approximation

To recover the I-V relation for this single level system, the "linear response" approximation is used: the problem consists in considering the variation of the current in the case of an applied bias $V << \mu_0$. In this limit, the Fermi-Dirac distributions of eq. 2.9 can be Taylor expanded at the first order as:

$$\begin{aligned} f_1(E) &\approx f_0(E) + (-\tfrac{\partial f_0}{\partial E})\,(\mu_1-\mu_0) \\ f_2(E) &\approx f_0(E) + (-\tfrac{\partial f_0}{\partial E})\,(\mu_2-\mu_0) \end{aligned} \tag{2.18}$$

From 2.18 and 2.7 it follows that

$$f_1(E) - f_2(E) \approx \left(-\frac{\partial f_0}{\partial E}\right) qV \tag{2.19}$$

Substituting this expression in the integral of eq. 2.17 and dividing by V at both the sides, one finds the conductance for this single level system in linear response approximation:

$$G = \frac{I}{V} = \frac{2q^2}{\hbar}\int_{-\infty}^{+\infty} dE\; D_\varepsilon(E)\frac{\gamma_1\gamma_2}{\gamma_1+\gamma_2}\left(-\frac{\partial f_0}{\partial E}\right) \tag{2.20}$$

2.2.6 Low Temperature case

In the low temperature limit, $k_BT << E-\mu_0$,

$$\begin{aligned} f_1(E) &\to \theta(E-\mu_1) \\ f_2(E) &\to \theta(E-\mu_2) \end{aligned} \tag{2.21}$$

where θ is the Heaviside step function. As a consequence eq. 2.17 becomes equal to

$$I = \frac{2q}{\hbar}\,\frac{\gamma_1\gamma_2}{\gamma_1+\gamma_2}\int_{\mu_2}^{\mu_1} dE\; D_\varepsilon(E) \tag{2.22}$$

Using again the linear response approximation, the DOS can be considered constant over the range $\mu_1 > E > \mu_2$ and equal to $D_\varepsilon(\mu_0)$, giving

$$I = \frac{2q}{\hbar} \frac{\gamma_1\gamma_2}{\gamma_1+\gamma_2} \overbrace{(\mu_2 - \mu_1)}^{qV} \underbrace{\frac{(\gamma_1+\gamma_2)/2\pi}{(\mu_0-\varepsilon)^2 + ((\gamma_1+\gamma_2)/2)^2}}_{D_\varepsilon(\mu_0)} \tag{2.23}$$

From this expression it is clear that the current is maximum if $\varepsilon = \mu_0$, which means that the energy level in the channel lies in between the electrochemical potentials of the two contacts.
If the coupling between the contacts and the channel are the same, $\gamma_1 = \gamma_2$, the maximum conductance for the single channel is 2 G_0 [6], with:

$$G_0 = \frac{I}{V} = \frac{q^2}{h} = 38.7\mu\text{S} = 1/(25.8 \times 10^3\Omega) \tag{2.24}$$

Despite what was found in 2.14, this result is consistent with the experimental observations and G_0 represents the quantum of conductance.
Furthermore, if more conductive levels are present in the range $\mu_1 > E > \mu_2$, the total conductance can be written as[7]:

$$G = M(E)|_{E=E_f}\, G_0, \tag{2.25}$$

with $M(E)$ being the density of modes (DOM), which gives the number of conductive channels when evaluated at $E = E_f$[8].
This expression, known as Landauer formula, is very powerful because it states that there exist a quantised conductance per channel and it reduces the problem to the knowledge of the function $M(E)$. While the conductance per mode is independent of the dispersion relation $E(\mathbf{k})$, the density of modes $M(E)$ is very dependent on the details of the problem at hand.

2.2.7 Elastic Resistors

In the previous section, it was shown that the flow of electrons is driven by the difference in the Fermi-Dirac distributions of the two contacts. This is a general truth for all the conductors independently on their size. However, the simple relationship given by eq. 2.17 is possible in the case of elastic resistors, i.e. in absence of inelastic scattering. For this reason, the model is valid not only in ballistic regime, with electrons travelling in the channel from source to drain in a straight trajectory ("like a bullet"), but also in presence of elastic scatterers, like static defects.

[6] The factor 2 comes from considering the spin degeneracy of the level.

[7] The levels are here supposed to be independent from each others. This is a strong assumption, whose validity will be discussed in the following section.

[8] In linear response approximation, $\mu_1 \approx \mu_2 \approx \mu_0$ and μ_0 is equal to the Fermi level of the device, E_f. It follows that the number of modes can be considered as a function of the Fermi level.

Energy conservation of the charge carriers in a resistor may appear like a contradiction, since it is well known that a dissipation of Joule heat is associated with every resistance. The point is that in absence of inelastic scattering mechanisms, the electrons do not loose energy in the channel, but they do loose energy in the contacts by thermalisation: $(\mu_1 - \varepsilon)$ energy is dissipated at the source and $(\varepsilon - \mu_2)$ at the drain. Thus, the total energy dissipated is $(\mu_1 - \mu_2)$ that is equal to the potential difference supplied by the battery. This energy is dissipated at the interface between the leads and the device by Joule effect

$$Q = I^2 (R_s + R_d) \tag{2.26}$$

with R_s and R_d that are the so-called "contact resistances"(see fig. 2.6).

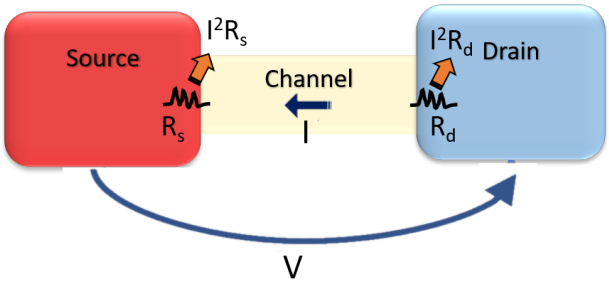

Figure 2.6: Representation of the energy dissipation in an "elastic resistor" by Joule effect. The resistances are localized in the contacts.

2.2.8 The Transmission

In presence of inelastic scattering, the density of modes is substituted by the transmission function, $\bar{T}(E)$, obtained by multiplying the DOM by a factor which includes the effect of the inelastic scattering mechanisms:

$$\bar{T}(E) = M(E)\,\mathcal{T}(E) \tag{2.27}$$

$\mathcal{T}(E)$ is the transmission coefficient and takes values in between 0 and 1, acting like a modulation function for the DOM.
If $\mathcal{T}(E) = 1$, it means that there are no scattering phenomena (the resistor is elastic) and the transmission coincides with $M(E)$.
The nature of $\mathcal{T}(E)$ will be further explained when speaking about thermal conduction and, in particular, about phonon-phonon scattering (Ch. 3 and Ch. 6). For further information about $\mathcal{T}(E)$ related to electron-electron and electron-phonon scattering refer to [28, 11].

2.2.9 Thermoelectric Transport Coefficients

The Landauer formalism in the linear response regime allows to find all the thermoelectric parameters. The electrical conductance, Seebeck coefficient and the electronic thermal conductance can be find with the following relations[28, 69]:

$$G = \frac{2q}{h}\, I_0 \qquad [1/\Omega], \tag{2.28a}$$

$$S = -\frac{k_B}{q}\,\frac{I_1}{I_0} \qquad [V/K], \tag{2.28b}$$

$$K_e = -\frac{2\,k_B^2\,T}{h}\left(I_2 - \frac{I_1^2}{I_0}\right) \qquad [W/K], \tag{2.28c}$$

where

$$I_j = \int_{-\infty}^{+\infty} \left(\frac{E - E_f}{k_B T}\right)^j \bar{T}(E)\left(-\frac{\partial f_0}{\partial E}\right) dE, \tag{2.29}$$

Hence, all the coefficients can be calculated if the transmission $\bar{T}(E)$ is known. Thus, in ballistic regime the problem reduces to compute the DOM. Two procedures are available to numerically evaluate the DOM.

2.2.10 Calculation of the Density of Modes

The "Counting Bands" method

First af all one has to identify a transport direction. In the case of graphene and TMDCs, which have a honeycomb like structure, the two conventional transport directions are pictured in fig. 2.7 and correspond to the so-called "Zig-Zag" and "Armchair".

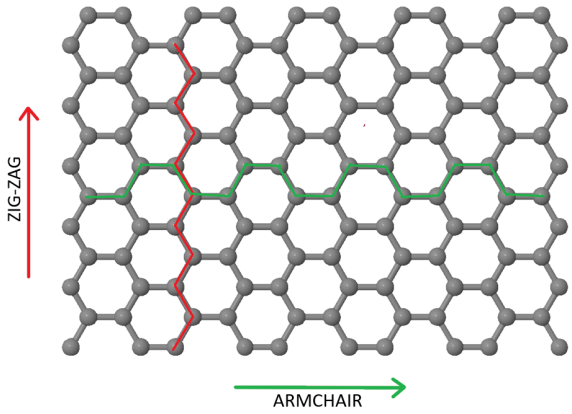

Figure 2.7: Zig-Zag (red) and Armchair (green) directions for crystals with honeycomb like structures

Then, it is necessary to define a conventional unit cell, in such a way that the first Brillouin Zone results to be rectangular. In this way one reciprocal vector will be parallel to the transport direction (z) and the other perpendicular (x).

Transport through a periodic system (no defects) corresponds to ballistic transport. In this case the DOM can be directly linked to the band structure.

Known the dispersion relation $E(k_\perp, k_\parallel)$, one has to fix a value of $k_\perp$ and count the number of bands crossing the energy of interest, E. Averaging over all the $k_\perp$ one finds the density of modes $M(E)$, i.e. total number of conductive channels of the system at a given energy E.

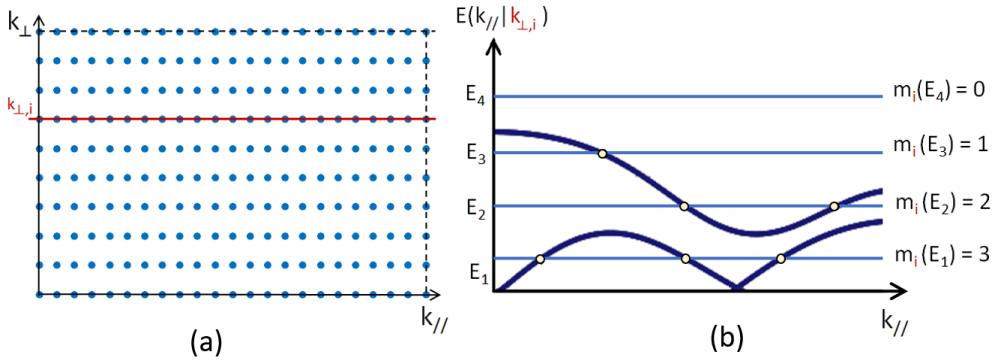

Figure 2.8: Example of the "counting modes" procedure: (a) the positive quadrant of the rectangular first BZ. (b) the band structure plotted along the path in the first BZ corresponding to the red line in (a). $m_i(E)$ is the number of band crossings at energy E in the direction given by $k_{\perp,i}$. The total number of modes $M(E)$, is obtained averaging the $m_i(E)$ over all the $k_{\perp,i}$.

It is clear from this procedure, that $M(E)$ is proportional to the the width L_x of the unit cell that was chosen for the calculation.
Therefore, the relevant quantities to make comparisons among different systems are the DOM per unit width and the conductance per unit width. From now on, $M(E)$ and $G(E)$ will refer to quantities per unit width, making the following change in notation:

$$M(E) \rightarrow M(E)/L_x$$
$$G \rightarrow G/L_x$$

As said, this "counting bands "procedure for the DOM calculation is valid in the case of ballistic transport, when the system is fully periodic.
Instead, when the symmetry of the system is broken, as in the case of transport through a material presenting a disordered distribution of defects, another method based on Green's functions is needed.

The Green's Functions Technique

To deal with disordered systems, the trick is to divide the system into semi-periodic contacts (leads) and a central part containing the defects (device). The setup is shown in fig. 2.9.
The two leads are constituted of the pristine material. They are semi-infinite and fully periodic. The device may have an arbitrary geometry and contains all the non-periodic parts of the system. In Ch. 5.2, this scheme is used to

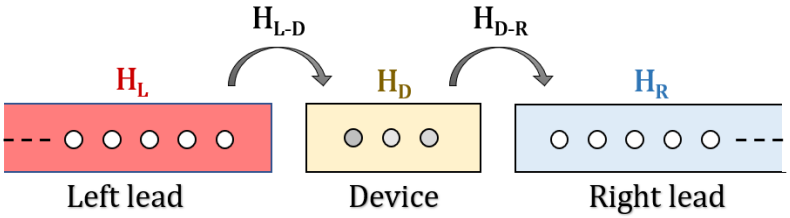

Figure 2.9: Schematic diagram for a general contact-device-contact setup. The contacts (leads) are semi-infinite and fully periodic. The device contains all the non-periodic parts of the system.

investigate single-layer MoS_2 with sulphur vacancies positioned in random sites of the lattice. In that case, the leads are made of pristine MoS_2 and the device contains unit cells with a missing S-atom in different positions, in order to reproduce a disordered distribution of vacancies.
With this decomposition, it is possible to define the Green's function of the infinite system by mean of a finite matrix equation. In this equation the semi-infinite leads comes as the so-called *surface Green's functions*, which are finite. In order to solve this matrix problem for a very long device (and thus to obtain the transmission), it is mandatory to have couplings only between neighbouring blocks. This means that there are non-zero coupling hamiltonians between each lead and the device (H_{L-D}, H_{D-R}) and zero-coupling between the two leads ($H_{L-R} = \varnothing$).
Only a code like *SIESTA* based on localised orbitals allows to obtain this kind of hamiltonian in which distant blocks are not coupled. In fact, the use of a basis set of plane waves, which spread infinitely in space, would result in the presence of couplings among all the blocks.

A detailed explanation of the Green's functions method can be found in references [53] and [24]. Reference [11] provides the parallelism between the detailed formulation of the Landauer Formalism, based on the Green's functions method, and the simplified way adopted to introduce the Landauer formula in the previous sections.

At this point, assuming to have solved the Green's functions problem, the final formula to compute the transmission in presence of non-periodical systems is given by [28]:

$$\bar{T} = Tr\left(\Gamma_1 \, G \, \Gamma_2 \, G^{\dagger}\right), \tag{2.30}$$

where G and $G^{\dagger}$ are respectively the retarded and advanced Green's function of the system [53] and

$$\Gamma_{1,2} = i(\Sigma_{1,2} - \Sigma_{1,2}^{\dagger}), \tag{2.31}$$

being $\Sigma_{1,2}$ the *self-energies* of the leads, which account for the coupling of the device with the leads [9].

[9] The *self-energies* are somehow related to the coupling energies γ_1 and γ_2 that were introduced in the treatment of the simple single level model (see ref. [11]).

In the ballistic case, the leads and the device are made exactly of the same material, hence the whole system is periodic and computing the transmission with the "counting bands" method or with the Green's functions technique is equivalent.

2.3 Phonon Transport

In this section the Landauer formalism will be used to evaluate the phonon thermal conductance. In fact, the procedure developed previously for electronic transport can be extended to phonon transport. A scheme of the system is shown in fig. 2.10.

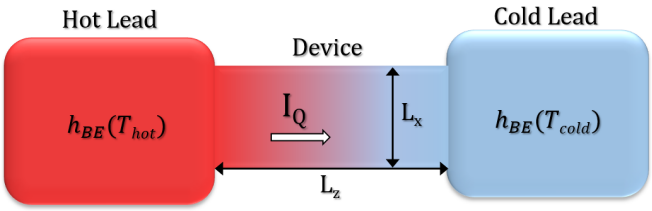

Figure 2.10: General scheme describing the study of the phonon transport within the Landauer Formalism. The device is between two thermal reservoirs at different temperatures. A heat flux crosses the device driven by the difference in Bose-Einstein distribution from the hot lead to the cold one.

The setup is analogous to the one for electronic transport: there are two leads kept at different temperatures (T_{hot} at the source and T_{cold} at the drain). The leads act as thermal reservoirs and a heat flux crosses the device from the source to the drain.
The carriers of heat are phonons, which are bosons. Thus, the right statistics to use is the Bose-Einstein (BE) distribution and not the Fermi-Dirac (FD) as for electrons:

$$\begin{aligned} h_1(\omega) &= f_{BE}(T_{hot}) = 1/\left[\exp\left(\frac{\hbar\omega}{k_B T_{hot}}\right) - 1\right] \\ h_2(\omega) &= f_{BE}(T_{cold}) = 1/\left[\exp\left(\frac{\hbar\omega}{k_B T_{cold}}\right) - 1\right] \end{aligned} \tag{2.32}$$

While for electronic transport the driving force was a gradient in electrochemical potential, which determines a difference in the FD distributions of the leads, the phonon motion is driven by a temperature gradient that originate different BE distributions in the hot and cold leads.
The channel is characterised by its phonon dispersion relation $\omega(\mathbf{k})$, which is found with *ab initio* calculations as explained in Ch. 1.3.
The couplings between the device and the contacts is given by the matching in their phonon dispersion relations, in analogy with the matching in

electronic band structures in the case of electron transport.

2.3.1 Phonon Thermal Conductance

With respect to eq. 2.17, the heat current can be obtained by making the following substitutions:

- $\underbrace{2q}_{\text{Charge carried per electronic state}} \rightarrow \underbrace{\hbar\omega}_{\text{Energy carried per phonon}}$
- $\underbrace{f_{1,2}(E)}_{\text{Fermi-Dirac distribution}} \rightarrow \underbrace{h_{1,2}(\omega)}_{\text{Bose-Einstein distribution}}$
- $\underbrace{\bar{T}(E)}_{\text{Transmission for electrons}} \rightarrow \underbrace{\bar{T}(\omega)}_{\text{Transmission for electrons}}$

So the heat current is expressed by:

$$I_Q = \frac{1}{h}\int_0^{+\infty} (\hbar\omega)\ \bar{T}(\omega)\ [h_1(\omega) - h_2(\omega)]\ d(\hbar\omega) \tag{2.33}$$

In linear response approximation, i.e. assuming that the temperature of the two leads are only slightly different from each other ($T_{hot} \approx T_{cold} \approx T$) [10], it is possible to write:

$$h_2 \approx h_1 + \frac{\partial h}{\partial T}\,\Delta T, \quad \text{with}$$
$$\Delta T = T_{cold} - T_{hot}$$

It follows that

$$[h_1 - h_2] \approx -\frac{\partial h}{\partial T}\Delta T \tag{2.34}$$

where,

$$\frac{\partial h(\omega)}{\partial T} = \frac{\hbar\omega}{k_B T^2}\frac{1}{(e^{\frac{\hbar\omega}{2k_BT}} - e^{-\frac{\hbar\omega}{2k_BT}})} = \frac{\hbar\omega}{k_B T^2}\frac{1}{\sinh^2(\frac{\hbar\omega}{2k_BT})}$$

Eq. 2.33 becomes

$$I_Q = \frac{\hbar^2}{8\pi k_B T^2}\ (-\Delta T)\ \int_0^{+\infty} d\omega\ \bar{T}(\omega)\ \frac{\omega^2}{\sinh^2(\frac{\hbar\omega}{2k_BT})} \tag{2.35}$$

[10] In linear response regime, the temperature of the two leads is considered to be almost equal to the lattice temperature in the channel. As a consequence, the device can be considered at constant temperature T, neglecting the temperature gradient originated by the temperature difference between the hot and cold leads.

Finally, the phonon thermal conductance is:

$$G_{ph} = -\frac{I_Q}{\Delta T} = \frac{\hbar^2}{8\pi k_B T^2} \int_0^{+\infty} d\omega \, \bar{T}(\omega) \, \frac{\omega^2}{\sinh^2(\frac{\hbar\omega}{2k_B T})} \tag{2.36}$$

In order to visualize the difference in the expressions of the electric and phonon conductance, it is useful to define the following "window functions" for electrons and phonons [27]:

$$\begin{aligned} W_{el}(E) &= \left(-\frac{\partial f_0}{\partial E} \right) \\ W_{ph}(\hbar\omega) &= \left\{ \frac{3}{\pi^2} \left(\frac{\hbar\omega}{k_B T} \right)^2 \left(-\frac{\partial h_0}{\partial(\hbar\omega)} \right) \right\} \end{aligned} \tag{2.37}$$

Their trend with respect to temperature is shown in fig. 2.11 and gives an idea of the energy range of the electrons (phonons), which contribute to the electric (phonon) conductance at different temperature T.

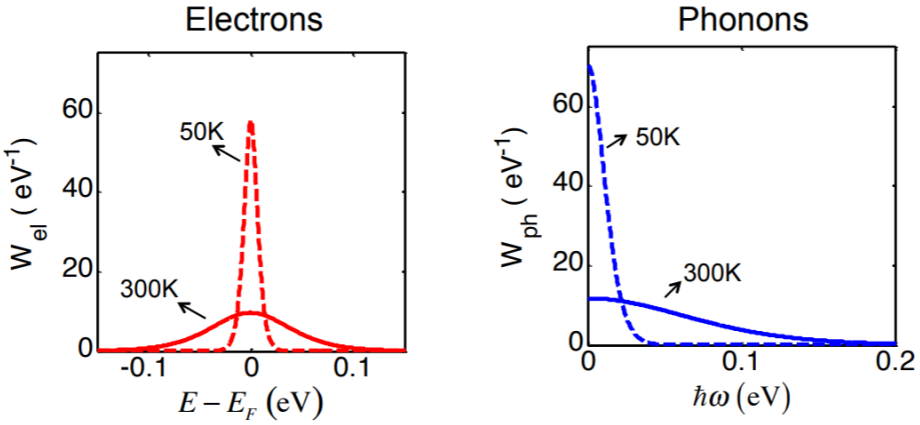

Figure 2.11: Comparison between the window function for electrons and phonons. From ref. [40]

2.3.2 Phonon Transmission

In analogy with the electrons case, the phonon transmission $\bar{T}(\omega)$, is equal to the product of the phonon density of modes $M(\omega)$, and the transmission coefficient $\mathcal{T}(\omega)$:

$$\bar{T}(\omega) = M(\omega)\,\mathcal{T}(\omega) \tag{2.38}$$

$M(\omega)$ represents the number of conductive channels (phonon branches) available to carry phonons with frequency ω.
$\mathcal{T}(\omega)$ is the transmission coefficient, which takes values in between 0 and 1 according to the influence of scattering phenomena. In absence of scattering $\mathcal{T}(\omega)$=1, hence $\bar{T}(\omega) = M(\omega)$.
In Ch. 3, it will be explained how to deal with Umklapp phonon-phonon scattering and with scattering by imperfections of the boundaries. The impact of these inelastic scattering mechanisms on the lattice thermal conductance was calculated as well. The results are provided in Ch. 6.

Phonon Density of Modes by "Counting Bands" Method

While the derivation of the electronic DOM is based on the electronic band structure $E(\mathbf{k})$, the phonon DOM is computed from the phonon dispersion relation $\omega(\mathbf{k})$.
In this thesis, the full dispersion relations of the studied materials are considered. $\omega(\mathbf{k})$ is computed by diagonalization of the the dynamical matrix, which represents the key quantity to study phonons[11].
Knowing the phonon dispersion relation in the whole Brillouin zone, $M(E)$ can be computed counting the bands crossing the energy of interest.[12]
A graphical example of the method is depicted in fig. 2.12

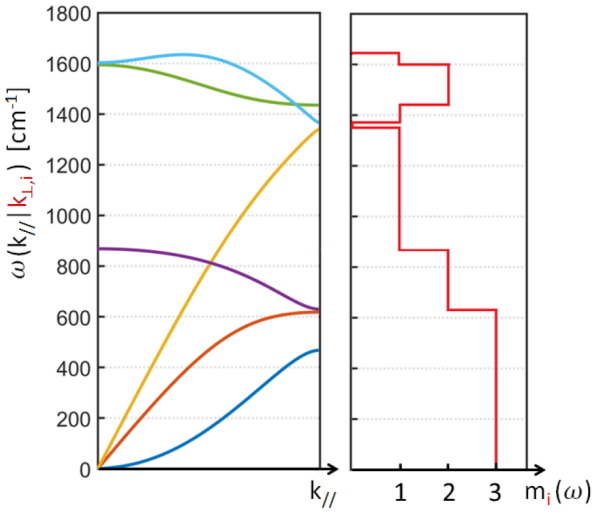

Figure 2.12: Example of the "counting modes" procedure for the phonon DOM calculation. The phonon dispersion relation is plotted along a path in the first BZ. In this case, with the solely aim to make an example, it corresponds to the phonon dispersion of graphene along the path $\Gamma \rightarrow M$. $m_i(E)$ is the number of branches crossing the energy E in the direction given by $k_{\perp,i}$. The total number of modes $M(E)$, is obtained averaging the $m_i(E)$ over all the $k_{\perp,i}$.

Phonon Transmission with the Green's Functions Technique

The Green's functions formalism introduced in the case of electronic transport can be extended to the study of phonon transport. This is essential to investigate the effect of defects, which introduce non-periodicity in the studied systems. A detailed description of the method can be found in references [96, 83, 84].

[11] The dynamical matrix can be seen as the analogous of the electronic hamiltonian for electrons. The method to compute the it with *SIESTA* is described in Ch. 1.3.

[12] The procedure is analogous to the one explained for the electronic density of modes (see. section 1.2.10)

2.3.3 Comparison between Full-Dispersion and Debye Model Evaluation of Phonon DOM

According to the largely used Debye Model, the phonon dispersion relation is approximated with a linear and isotropic dispersion, $\omega = v_s k$. Thus, $M(\omega)$ per polarization is given as follows [27]:

$$\begin{aligned} M_\lambda(\omega) &= (L_x\, L_y)\, \frac{\omega^2}{4\pi v_{S,\lambda}^2} \quad (3D) \\ M_\lambda(\omega) &= L_x\, \frac{\omega}{\pi v_{S,\lambda}} \quad (2D) \end{aligned} \tag{2.39}$$

where $v_{S,\lambda}$ is the speed of sound (phonon group velocity at the Γ point) and λ is the index related to the three possible polarizations of the acoustic modes, $\lambda =$ ZA, TA, LA.
While for 3D materials, the isotropic assumption could be reasonable for many systems, it leads to a criticality dealing with 2D materials. The reason lies in the differences between in-plane (TA, LA) and out-of-plane (ZA) modes. The sound velocities of the TA and LA modes are high[13], while the one of the ZA mode is low (it is zero for pristine 2D materials [47]). However, far from the Γ point, the group velocity of the ZA phonons is not negligible. As a consequence, the ZA branch does contribute to heat transport. Indeed, the thermal conductance of the 2D systems studied will result strongly affected by ZA phonons with $\mathbf{k}$ far from the Γ point.
Moreover, also for the TA and LA in-plane modes, the dispersion relation deviates from the linear trend predicted by the Debye model. Hence the 2.39 are valid only when the temperature is low enough that only phonons with $\mathbf{k}$ close to Γ are populated.
A similar argument is valid for the optical branches. In fact, it is known that the acoustic modes dominate the heat conduction, since the group velocity of optical branches is zero at Γ. Optical phonons are less dispersed as well. However, their group velocity is not-zero in all the Brillouin zone.
In references [28] and [27] the *full-band* versus *effective mass* evaluation of the electronic DOM and the *full-dispersion* versus *Debye model* evaluation of the phonon DOM are widely treated. It results that the effective mass description works quite well for electrons, while the Debye model for phonons does not lead to the same accuracy. The reason is that the relevant energy range for electrons lies near the bottom of the band, but for phonons the entire phonon dispersion is important (see fig. 2.11).

2.4 Counting Bands or Green's Functions?

In Ch. 4 the transport properties of graphene and TMDCs are studied in ballistic regime. In Ch. 5.1 a monolayer of MoS_2 is analysed in presence of

[13] for graphene they are $\approx$ 14 and 24 Km/s, respectively

a single elastic scatterer (a sulphur vacancy). In these studies, the transmission is equal to the DOM, because $\mathcal{T}(\omega) = 1$, since there are no inelastic scatterers. The leads and the device are made of the same material. Therefore the systems are fully periodic and it was possible to employ the "counting bands" method to compute the phonon transmission.

In Ch. 6, the "counting bands" method is used as well, with the difference that phonon-phonon Umklapp scattering is included. So, $\mathcal{T}(\omega)$ will be evaluated according to a procedure described in Ch. 3.

Diversely, in Ch. 5.2, the effect of a disordered distribution of defects in MoS_2 was investigated. The systems consist of a single-layer of MoS_2 with sulphur vacancies disposed in randomised positions of the lattice.
The device is modelled by joining different blocks as in fig. 2.13. Here P stands for a "pristine block", i.e. a monolayer without defects, and S_i stands for a block whose unit cell present an S-vacancy at the i-th site of the lattice. Four different locations were considered for the S-vancancy ($i = 1, 2, 3, 4$).

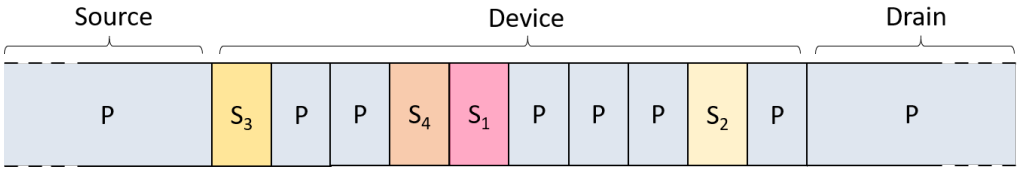

Figure 2.13: Device with a disordered distribution of defects. P stands for a "pristine block", i.e. a monolayer without defects, and S_i stands for a monolayer whose unit cell present an S vacancy in a lattice site labelled as i.

By changing in a random way the number, type and relative position of the blocks, two analysis were done: the first varying the length of the device L_z, at fixed concentration of S vacancies; the second varying the concentration at fixed L_z.
The presence of such a random distribution introduces an asymmetry in the transport property of the system and, in turn, different couplings. Therefore, a matrix treatment with the Green's functions formalism was necessary.

Chapter 3

Effect of Inelastic Scattering on Phonon Transport

This chapter is devoted to the effect of intrinsic inelastic scattering phenomena on phonon transport. In particular, it will deepen the impact of phonon-phonon Umklapp scattering (U-scattering) and diffusive phonon-boundary scattering (B-scattering) on the phonon transmission.
Considering these inelastic scattering phenomena marks a transition to a mixed ballistic-diffusive transport regime: the Landauer formalism continues to be valid, provided that the scattering effects are included in the transmission coefficient. In other words, the phonon thermal conductance is still given by eq. 2.36, but $\bar{T}$ does not coincide with the only phonon density of modes $M(\omega)$, as for the ballistic case, because the transmission coefficient $\mathcal{T}(\omega, T)$ is not unitary. Therefore, the full expression $\bar{T}(\omega) = M(\omega)\,\mathcal{T}(\omega, T)$ must be considered to evaluate the phonon transmission.
This approach was used in the study of the thermal conductance of graphene presented in Ch. 6, where it is investigated how the phonon transmission changes with respect to the pure ballistic case (Ch. 4).
A suitable expression for the transmission coefficient, taking into account the above mentioned scattering mechanisms, will be discussed hereafter.

3.1 Anharmonic Crystal Interactions

The calculation of phonon dispersion described in Ch. 1.3 relies on the harmonic approximation: the expansion of the potential energy is arrested to terms quadratic in the interatomic displacements. Considering higher order anharmonic terms is necessary to explain phenomena like thermal expansion, interactions between lattice waves and dependence of the interatomic force constants on pressure and temperature [34].
Including anharmonic terms, and thereafter calculating the dynamic matrix (see Ch.1.3), would in principle allow to evaluate these effects purely *ab initio*. In practice this is not viable from a computation-time point of view. Hence, suitable physical models are needed to describe anharmonic phenomena without passing through the direct calculation of the dynamic

matrix.
According to ref. [28] the transmission coefficient reads:

$$\mathcal{T}(\omega, T) = \frac{\Lambda(\omega, T)}{L_z + \Lambda(\omega, T)} \tag{3.1}$$

where $\Lambda(\omega, T)$ is the phonon mean free path and L_z is the length of the device in the transport direction.
Looking at this formula, the transmission coefficient can be physically interpreted as the probability of a phonon with frequency ω to propagate from one contact to the other without being annihilated by some inelastic scattering processes. In fact, if $\Lambda(\omega, T) >> L_z$ then $\mathcal{T}(\omega, T) \to 1$ and one recover the ballistic case, meaning that there is a negligible probability that the phonon is scattered along his way from the hot to the cold lead.
Diversely, if $\Lambda(\omega, T) << L_z$ then $\mathcal{T}(\omega, T) \to \Lambda(\omega, T)/L_z$. This corresponds to the diffusive limit, in which phonons with frequency ω are scattered in inelastic way before reaching the cold contact.[1]

Thus one has to find an expression for Λ accounting for all the relevant inelastic scattering phenomena. According to Matthiessen's rule, which assumes that different scattering mechanisms are independent, the reciprocal of the mean free path can be derived as [87]

$$\Lambda^{-1} = \Lambda_U^{-1} + \Lambda_B^{-1} + \Lambda_D^{-1} \tag{3.2}$$

where λ_U, λ_B and λ_D are the mean free path for Umklapp scattering, boundary scattering and point defect scattering respectively.
In this thesis, the effect of point defect scattering is included in the *ab initio* calculation of the dynamic matrix by use of the Green's function technique (see 2.4). Thus, Λ_D is neglected in the sum in order not to count it twice, while Λ_U and Λ_B have to be computed.

The final expression for the phonon thermal conductance is found plugging eq. 3.1 into 2.36:

$$G_{ph}(T) = \frac{\hbar^2}{8\pi k_B T^2} \int_0^\infty \underbrace{\left[M(\omega) \frac{\Lambda(\omega, T)}{L_z + \Lambda(\omega, T)} \right]}_{\bar{T}(\omega)} \frac{\omega^2}{\sinh^2(\frac{\hbar\omega}{2K_B T})} d\omega \tag{3.3}$$

from which the lattice thermal conductivity is derived:

$$\begin{aligned} \kappa(T) &= \frac{L_z}{L_x L_y} G_{ph}(T) \\ &= \frac{\hbar^2}{8\pi k_B T^2} \frac{L_z}{L_x L_y} \int_0^\infty \left[M(\omega) \frac{\Lambda(\omega, T)}{L_z + \Lambda(\omega, T)} \right] \frac{\omega^2}{\sinh^2(\frac{\hbar\omega}{2K_B T})} d\omega \end{aligned} \tag{3.4}$$

[1] Other works, like [100], used directly the formulation $\mathcal{T}(\omega, T) = \Lambda(\omega, T)/L_z$ instead of the 3.1. Since the phonon mean free path can in principle exceed the length of the device, then one should exclude the phonons with $\Lambda(\omega, T) > L_z$ in order to avoid $\mathcal{T}(\omega, T) > 1$. In any case, the form of eq. 3.1 is preferable. As a proof, it is sufficient to consider that a phonon with $\Lambda = L_z$ must have probability 1/2 to be transmitted.

It is useful to remark that in the ballistic case, $\Lambda(\omega, T) >> L_z \ \forall\omega$, the conductance is independent on the length of the sample in the transport direction L_z, while the conductivity is proportional to L_z. Viceversa, in the diffusive case $\Lambda(\omega, T) << L_z \ \forall\omega$, the conductance is proportional to L_z^{-1} and the conductivity is independent of L_z (macroscopic systems).
The distinction between these two regimes is due to both the length of the device and the strength of scattering phenomena, which affects phonons with different ω in a dissimilar way. Since phonon-phonon inelastic scattering is an intrinsic resistive mechanism, independent on the quality of the sample (defects, edge roughness), a regime where all the phonons propagate in a pure ballistic way is possible only for $L_z \to 0$. In this limit, equivalent to consider a system of atomic size, all the periodic properties of the crystal are lost, making meaningless the formalism developed so far that does not include finite effects.
This mixed approach, based on the transmission function from the Landauer formalism and on a mean free path to include the scattering processes[2], is instead very effective in the case of mesoscopic systems.

It is now the moment to understand how to deal with Umklapp and edge-roughness scattering.

3.2 Phonon-Phonon Scattering: Normal and Umklapp processes

If the forces between atoms were purely harmonic, there would be no mechanism for collisions between different phonons, and the mean free path would be limited only by collisions of a phonon with the crystal edges and by lattice imperfections. With anharmonic lattice interactions, there is coupling between different phonons limiting the value of the mean free path [34].
The effect of anharmonic terms can be understood with this argument by Ziman [103]: Suppose that there is moving through the solid a disturbance of wave vector $\mathbf{q}$. As the lattice vibrates, some atoms come closer than their equilibrium distance and others move farther apart. Another phonon of wave vector $\mathbf{q}'$, attempting to pass through the medium, will see the elastic properties slightly altered. The phonon $\mathbf{q}$ will thus generate a periodic variation in the refractive index of the medium, and the phonon $\mathbf{q}'$ will be reflected as if from a diffraction grating.

An important concept introduced by Peierls (1929) is that of *normal* (N) vs *umklapp* (U) phonon-phonon scattering. N scattering conserves the phonon momentum and induces no thermal resistance by itself, and it merely redistributes momentum among different phonon modes. In comparison, U

[2]This is somehow similar to a treatment based on solving Peierls-Boltzmann Transport Equations (PBTE) in relaxation time approximation. A parallelism between Landauer Formalism and PBTE can be found in reference [28].

scattering is a momentum-destroying process that leads to thermal resistance. The standard explanation [34, 3, 103] of the distinction between the N and U process is illustrated in fig. 3.1.

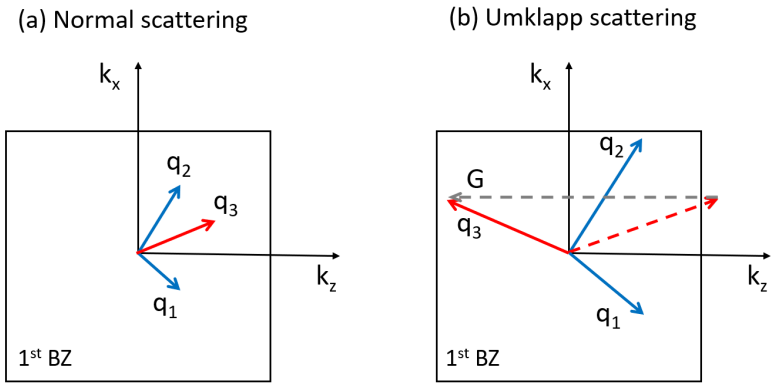

Figure 3.1: Schematic illustration of Normal process (a) and Umklapp process (b), as conventionally defined in the case of three-phonons absorption scattering.

Considering a three-phonon absorption scattering process, in which two phonons of angular frequencies ω_1 and ω_2 merge into one of angular frequencies ω_3, energy conservation takes the form:

$$\hbar\omega_1 + \hbar\omega_2 - \hbar\omega_3 = 0 \tag{3.5}$$

In an N-process, momentum conservation expressed in terms of corresponding phonon wave vectors takes the form:

$$\mathbf{q}_1 + \mathbf{q}_2 - \mathbf{q}_3 = 0 \tag{3.6}$$

whereas in a U-process there is a non-zero reciprocal lattice vector $\mathbf{G}$ on the right hand-side:

$$\mathbf{q}_1 + \mathbf{q}_2 - \mathbf{q}_3 = \mathbf{G} \tag{3.7}$$

The generally accepted statement that phonon-phonon scattering processes consist of momentum-conserving normal scattering and momentum-destroying Umklapp scattering has raised some questions; a complete understanding of their contribution to thermal conductivity requires further studies and clarifications.
In [42] it is emphasized that no rigid line between N and U processes can be drawn because their definition depends on the choice of the primitive cell of the reciprocal lattice. N-processes alone do not create thermal resistance, but they do contribute to thermal resistance when U-processes (or scattering from defects or impurities) are present.
Recently, Ding *et al.* [13] observed that Umklapp scatterings are not necessarily resistive : no thermal resistance is induced if the projected momentum is conserved in the direction of heat flow. Looking at the scheme for Umklapp scattering of fig. 3.1, it is clear that U scattering induces resistance in

the z direction but not in the x direction. This distinction becomes particularly relevant in systems with strong anisotropy and it is not supposed to have a strong impact when considering in-plane transport in bi-dimensional TMDCs, since the thermal conductance in the armchair and zig-zag directions is almost isotropic.

In this thesis, the phonon life time related to phonon-phonon inelastic scattering was evaluated according to a formulation introduced by Klemens based on time-dependent perturbation theory [19, 18], but introducing separate life-times for different phonon branches (τ_λ^U), as reported in many works on graphene [46, 48] and TMDCs [85, 102, 100, 7]:

$$\tau_\lambda^U(\omega, T) = \frac{M\ v_\lambda^2(\omega)\ \omega_\lambda^{max}}{\gamma_\lambda^2(\omega)\ k_B T\ \omega^2} \tag{3.8}$$

Here γ_λ is the Grüneisen parameter, which characterizes the strength of the Umklapp phonon-phonon scattering process for branch λ. T is the temperature, M the sum of the masses of the basis atoms of the unit cell, and ω_λ^{max} is the highest frequency[3] of branch λ. $v_\lambda(\omega)$ is the modulus of the phonon group velocity, given by the modulus of the phonon dispersion slope:

$$v_\lambda(\omega) = \left| \frac{\partial \omega(\mathbf{q})}{\partial \mathbf{q}} \right| \tag{3.9}$$

Once known the life time, it is straightforward to obtain the Umklapp mean free path:

$$\Lambda_\lambda^U(\omega, T) = v_\lambda(\omega) \cdot \tau_\lambda^U(\omega, T) = \frac{M\ v_\lambda^3(\omega)\ \omega_\lambda^{max}}{\gamma_\lambda^2(\omega)\ k_B T\ \omega^2} \tag{3.10}$$

The properties such as phonon dispersion relation, phonon group velocity and Grüneisen parameter were calculated by using *SIESTA* combined with the open source package for phonon calculation *PHONOPY* [75, 77].

3.2.1 Grüneisen parameter

The Grüneisen parameter describes the thermal expansion of a crystal on its vibrational properties and it is related to third-order force constants directly [77]. The larger the Grüneisen parameter, the stronger anharmonic vibrations. The expression for the Grüneisen parameter is given by [57]:

$$\gamma = \frac{3\alpha B V_m}{C_V} \tag{3.11}$$

[3] In some papers [102, 85, 7] ω_λ^{max} is referred to as the Debye frequency of the branch λ. This comes probably from a diffuse use in the past years of the Debye-Callaway model for lattice thermal conductivity [64, 99]. Therefore, only acoustic branches were considered, in which a linear phonon dispersion relation is assumed and the maximum frequency allowed coincides with the Debye frequency. Diversely, a full band treatment is used in this thesis, hence the definition of highest frequency of the branch, given by Nika and Balandin [48], seems more appropriate.

where α is the linear thermal expansion coefficient, B is the bulk modulus, V_m is the molar volume and C_V is the isometric heat capacity.
This formulation is based on macroscopic quantities and it is useful to evaluate γ from empirical data. Otherwise, the bulk modulus B and linear thermal expansion coefficient α can be calculated using the quasi-harmonic approximation (QHA), which takes into account the first order anharmonicity [76]. However, a more suitable approach for this thesis comes from the definition of the so-called mode Grüneisen parameter, which is linked to the variation of the phonon dispersion relation of the λ-th mode with the size of the lattice parameter a [7]:

$$\gamma_\lambda(\mathbf{q}) = -\frac{a_0}{\omega_\lambda(\mathbf{q})}\frac{d\omega_\lambda(\mathbf{q})}{da} \tag{3.12}$$

where a_0 is the relaxed equilibrium lattice constant.
The mode-averaged Grüneisen parameter can be obtained subsequently as:

$$\gamma_{ave}^{mode} = \frac{1}{C_V}\sum_{\lambda,\mathbf{q}} \gamma_\lambda(\mathbf{q}) C_{V,\lambda}(\mathbf{q}) \tag{3.13}$$

In [57] it is shown that the two approaches 3.11 and 3.13 lead to the same results.
This second approach is preferred in this work because it computes the mode Grüneisen parameter from the knowledge of the phonon dispersion relation, keeping track of the dependence on every $\mathbf{q}$ in the first BZ. Hence, it is in line with the full-band treatment used in all the thesis.

To compute the mode Grüneisen parameter *ab initio* it is necessary to run three phonon calculations with different values of the lattice parameter.
At first, the usual structure optimization process is performed in order to find the lattice parameter a_0. The phonon dispersion relation corresponding to this relaxed structure is computed as well.
In addition, other two runs are performed by dilating and contracting the lattice parameter a_0 of $\pm 0.5\%$, equivalent to consider the application of a biaxial strain. Thus, two other dispersion relations are found corresponding to the lattice parameters $a_{1,2} = a_0 \pm 0.5\%$.
Finally, provided the three dispersion relations, the 3.12 can be solved by finite differentiation to find the Grüneisen parameter $\gamma_\lambda(\omega(\mathbf{q}))$.
In this process *SIESTA* was used to perform the DFT calculations; namely to compute the interatomic force constants of the three configurations and, hence, the phonon dispersions for the different lattice parameters. The *PHONOPY* code was used to compute the Grüneisen parameter by finite differentiation.
Moreover, *PHONOPY* takes advantage of the system's symmetry to optimize the direction of the atomic displacements for the calculation of forces. This is an advantage with respect to *VIBRA* because it allows to reduce the number of displacements[4] and so the number of SCF steps. As a con-

[4]Within *VIBRA*, every atom is displaced six times, corresponding to the positive and negative directions of the three cartesian axis.

sequence, in highly symmetrical systems (without defects) it is possible to strongly reduce the computation time. In the calculation of the Grüneisen parameter, which requires three phonon calculations as mentioned above, symmetry is a valuable friend.

3.3 Diffusive Boundary Scattering

The presence of boundaries is not included in the treatment based on the Landauer formalism due to the application of periodic boundary conditions. In real samples, boundaries are imperfect and they are reason for inelastic scattering.
Phonon-boundary scattering can be evaluated as [48, 47, 102, 18, 103]:

$$\tau_{\lambda}^{B}(\omega) = \frac{D}{v_{\lambda}(\omega)} \frac{1+p}{1-p} \tag{3.14}$$

where D is the nanostructure or grain size and p is the specularity parameter, defined as the probability of specular scattering at the boundary. The specularity parameter ranges from 0 for a completely rough boundary to 1 for a perfectly smooth boundary. In the case $p = 1$, the scattering process at the boundary is completely elastic, while it becomes progressively inelastic moving to lower p. The mean free path associated to scattering at the boundaries is therefore:

$$\Lambda_{\lambda}^{B}(\omega) = v_{\lambda}(\omega)\ \tau_{\lambda}^{B} = D\ \frac{1+p}{1-p} \tag{3.15}$$

that does not depend on the phonon group velocity. The dependence on ω is instead preserved because included in the specularity parameter p, which can be found fitting experimental data or from the surface roughness [48, 103].

3.4 Approximations and Differences with Other Works

Calculating the Umklapp scattering life time in this way is usually associated with the following simplifications [47]:
1) substitution of the phonon velocities and Grüneisen parameters with effective values obtained by averaging over the acoustic phonon polarization branches;
2) omission of the Umklapp processes characterized by the reciprocal-lattice vectors that are not parallel to the heat flux direction;
3) approximate accounting of the phonon selection rules and simplified description of the regions of the allowed phonon transitions in the Brillouin zone.
A more rigorous study of the lattice thermal conductivity of graphene was

performed by Nika *et. al* [47], using the phonon dispersion obtained with the valence-force field (VFF) method. The authors treated the three-phonon Umklapp scattering considering all phonon relaxation channels allowed by the energy and momentum conservation in graphene BZ.

Moreover, in the majority of articles the contribution of optical branches to the thermal conductivity is considered negligible due to the short phonon life time [102]. From the phonon dispersion relations calculated *ab initio* and showed in Ch. 4, it is indeed found that the optical branches have a zero group velocity at the Γ point and they are poorly dispersed throughout the BZ with respect to the acoustic modes. However, calculations for pristine graphene and TMDCs show that the phonon transmission function is significantly higher than zero in the range of frequencies corresponding to the optical modes. This means that optical branches do contribute to the thermal conductance in pristine bi-dimensional materials. Moving to more realistic systems with defects, as for MoS_2 calculations in Ch. 5, it is found that the transmission in the optical range of frequencies is lowered more than in the acoustic one. In any case, the contribution of optical modes to thermal conductivity is not negligible.
For these reasons, the choice has been made to use eq. 3.8 to evaluate the phonon life times of the acoustic modes as well. The goal is to verify *a posteriori* whether the acoustic branches do not contribute to thermal conductance, because of extremely short mean free paths, or if a full-band treatment may evidence a contribution that was not considered in previous works based on a Debye-like model [27].

Together with considering optical modes, an original contribution of this thesis consists in calculating τ_λ^U as a function of $\omega(\mathbf{q})$, so that, for each phonon, the corresponding life time, mean free path and transmission coefficient are known. In works based on PBTE [102, 85, 46], it is instead common to employ an effective value $\bar{\Lambda}_\lambda$ for the λ-branch by averaging over the wave-vectors $\mathbf{q}$ in the BZ for a given mode λ.
To understand why this is important, one should notice that every integral over ω corresponds in the codes to a finite sum over all the q-points in the first BZ. Remembering that separate life-times were introduced for different phonon branches, eq. 3.3 is rewritten to show the dependence on λ and $\mathbf{q}$:

$$\begin{aligned} G_{ph}(T) &= \frac{\hbar^2}{8\pi k_B T^2} \sum_\lambda \int_0^\infty \left[M_\lambda(\omega) \, \frac{\Lambda_\lambda(\omega,T)}{L_z + \Lambda_\lambda(\omega,T)} \right] \frac{\omega^2}{\sinh^2(\frac{\hbar\omega}{2K_B T})} d\omega \\ &= \frac{\hbar^2}{8\pi k_B T^2} \sum_\lambda \sum_{\mathbf{q}\in BZ} \left[M_\lambda(\omega(\mathbf{q})) \, \frac{\Lambda_\lambda(\omega(\mathbf{q}))}{L_z + \Lambda_\lambda(\omega(\mathbf{q}))} \right] \frac{\omega^2}{\sinh^2(\frac{\hbar\omega(\mathbf{q})}{2K_B T})} \\ &\approx \frac{\hbar^2}{8\pi k_B T^2} \sum_\lambda \frac{\bar{\Lambda}_\lambda}{L_z + \bar{\Lambda}_\lambda} \sum_{\mathbf{q}\in BZ} M_\lambda(\omega(\mathbf{q})) \, \frac{\omega^2}{\sinh^2(\frac{\hbar\omega(\mathbf{q})}{2K_B T})} \end{aligned} \tag{3.16}$$

Averaging phonon life times over the BZ to take the transmission coefficient out of the integral introduces a numerical error. Moreover, keeping the wave-vector dependence was necessary for technical details in the code that Christophe Adessi and I wrote to compute the transmission. In fact, a code was needed which combines the calculation of the density of modes $M(\omega)$, based on *VIBRA*, with the transmission coefficient $\mathcal{T}$ that is function of the group velocities and Grüneisen parameters computed with *PHONOPY*.

Finally, in the analysis developed in Ch. 6, arbitrary values were assigned to the specularity parameter, neglecting the dependence on ω hidden in its formulation, and with the only aim to visualize its impact on the lattice thermal conductance. p is seen simply as an indicator of the effect of the irregularities of the boundaries in real samples, in order to help comparing *ab initio* results with experimental data.

Part II

Results

Chapter 4

Thermoelectric Transport Properties in Ballistic Regime

The first goal of this work is to determine the phonon transport properties of graphene and of single-layer (SL) transition metal dichalcogenides (MoS_2, WS_2, $MoSe_2$ and WSe_2) in ballistic regime, i.e. considering pristine materials in absence of any scattering phenenomenon.
The study of phonon properties in graphene and TMDC has attracted strong attention of the physics and engineering community due to many unique properties and potential applications [48, 102].

Graphene is known to have a very high thermal conductivity κ, with values included in the interval $3080 - 5300\ \mathrm{W\,m^{-1}\,K^{-1}}$ according to experimental optical (non-contact) measurements near room temperature and in diffusive regime [22]. This extremely high thermal conductivity could find interesting applications for heat removal, which is a crucial issue especially for continuing progress in electronic industry owing to increased levels of dissipated power density and speed of electronic circuits [48].

Unlike zero-band gap graphene, TMDCs possess a direct band gap which allows potential applications such as field effect transistors (FETs) [59] and electroluminescent devices [72]. In addition, TMDCs monolayers are known for large Seebeck coefficient (S) and low thermal conductivity (κ), which is mandatory in thermoelectric application to improve the thermoelectric energy conversion efficiency [102]. Experimentally measured values of κ in few-layers (FL) MoS_2 are from 0.4-1.59 $\mathrm{W\,m^{-1}\,K^{-1}}$, to around 52 $\mathrm{W\,m^{-1}\,K^{-1}}$ by Raman spectroscopy approach. This large discrepancy may originate from different sample quality, measurement methods and accuracy. Thus numerical simulations has the potential to facilitate the understanding of heat conduction in SL MoS_2 [7].
The investigation of the thermal properties in two-dimensional systems has many peculiarities not present in the study of bulk materials. In addition, theoretical studies suggested that phonon transport in strictly two-dimensional and one-dimensional systems can reveal exotic behaviour, leading to infinitely large intrinsic thermal conductivity [48].

For instance, once the conductance of a sample is obtained experimentally or computationally, the thickness of the monolayer L_y has to be defined in order to determine the conductivity. Unfortunately, this thickness has not a unique definition for 2D materials. Indeed, the height of the unit cell adopted for the calculation has the only purpose to reproduce the vacuum; hence, it is not the measure of the layer thickness. In this thesis L_y has been taken equal to the interlayer distance of the bulk materials (e.g. the distance between two graphene layers in graphite).
In addition, the calculations employ periodic boundary conditions. Therefore, all the samples consist in an infinite plane of atomic thickness, reproduced by periodical repetition of the selected primitive cell.
The relevant quantity to compare the phonon transport properties of ideal pristine materials is the conductance per unit width:

$$G_{ph} = C_{ph}/L_x \tag{4.1}$$

where C_{ph} is the conductance and L_x is the width of the unit cell.
Furthermore, in the ballistic regime the conductance does not depend on the length of the device (L_z) [1].
A different behaviour will be observed in the next chapters, which face the transition to the diffusive regime. There, the conductance will strongly depend on L_z[1] due to the inclusion of scattering mechanisms, such as the collisions with a distribution of lattice defects (Ch. 5.2) and phonon-phonon Umklapp scattering (Ch. 6). In these cases, the usual thermal conductivity (κ) can be defined as:

$$\kappa_{ph} = \frac{L_z}{L_x L_y} C_{ph} \tag{4.2}$$

All the calculations presented in this thesis have been performed using the *SIESTA ab initio* package [71] under the generalized gradient approximation (GGA) of Perdew, Burke and Ernzerhof [58] and by using Troullier-Martin norm-conserving pseudopotentials [80]. The basis set used for the calculations of this chapter correspond to a dζp ("double-zeta-polarized") basis, which have been optimized using the simplex tool of the SIESTA package[2].

4.1 Graphene

4.1.1 Electronic Band Structure and Density of States

As discussed in Ch. 1, the first step in any *ab-initio* calculation consists in computing the Kohn-Sham hamiltonian. From its diagonalization it is straightforward to obtain the electronic band structure and the density of states. The study of these properties is important not only to compute S and σ_{el}. In fact, they provide important information to find a strategy for

[1] The room temperature thermal conductivity of SL WSe_2 can be decreased by about 95% passing from a $1\mu m$ sized sample to one with 10 nm size [102].
[2] This step was performed by Christophe Adessi for previous works [1].

reducing the phonon thermal conductivity without affecting too much the power factor.

For the structure optimization step of pristine materials, the unit cell used as input coincides with the primitive cell. A representation of graphene's primitive cell with its first Brillouin zone is given in fig. 4.1.

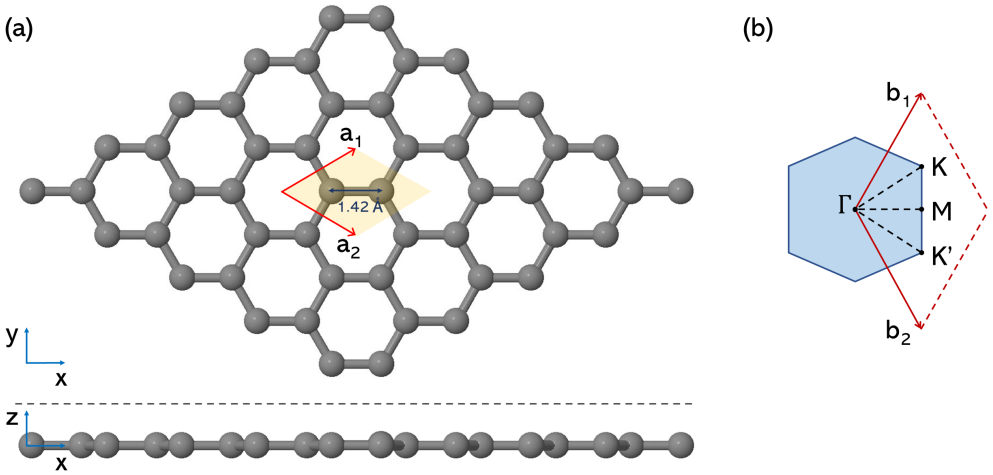

Figure 4.1:
(a) Frontal and side view of graphene's unit cell and of the 5x5x1 supercell used for the computation of the phonon dispersion relation. The unit cell, highlighted in yellow, coincides with the primitive cell of the lattice. The distance between the two C atoms of the basis is equal to 1.42 Å.
(b) First Brillouin zone with its high symmetry points and the reciprocal vectors.

The atomic structure was optimized up to forces less than 10^{-4} eV/Å and stresses less than 0.1 MPa. The Monkhorst-Pack scheme [45] was used for the integration of the Brillouin zone with a k-mesh of 10x1x10 k-points. A mesh-grid with energy cutoff of 600 Ry was employed for solving integrals in direct space with fast Fourier transforms.
Very restrictive tolerance parameters are needed to compute accurately the dynamic matrix. In particular, high accuracy is required to reproduce the correct trend of the phonon out-of-plane modes in 2D materials, which are very susceptible to tiny variations in the structure geometry [77]. For this reason, a series of test calculations have been carried out to identify the best combination of parameters.[3]

The electronic band structure is plotted in fig. 4.2 along the path in the first Brillouin zone connecting the high symmetry points $\Gamma - M - K - \Gamma$. This plot is restricted to the range of energy close to the Fermi level (E_f), which

[3]Another method is possible in order to use less restrictive relaxation parameters and reduce the computation time. It requires an application of a post-calculation correction on the inter-atomic force constants, based on the symmetry invariance under rotation of the crystal [86]. Therefore, I wrote a code in Fortran to apply this correction.

is the one of interest for transport properties. On the right, the density of states (DOS), computed by using a mesh of 200x1x200 k-points, is shown.

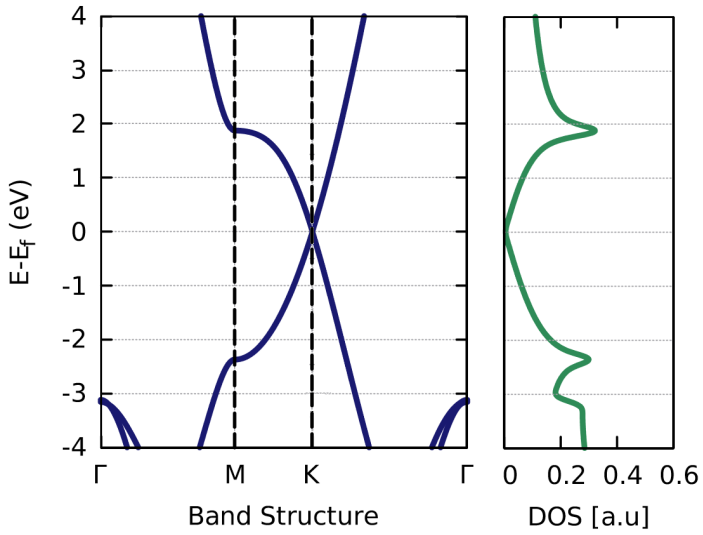

Figure 4.2: Electronic band structure and density of states (DOS) of graphene in proximity of the Fermi level (E_f).

The following observations can be deduced from the plot of graphene's electronic band structure:

1) The conduction and valence band touch each other at the K points (Dirac cones [39]). This is the most characteristic feature of graphene, responsible for its ambipolar conductivity. The density of states is linear for both the conduction and the valence band. The effective mass approximation is not able to describe the conduction of carriers, which behave like massless particles. This concept is at the base of the extremely high electronic (and thermal) conductivity of graphene.

2) Graphene is not suitable to be employed in thermoelectric applications. In fact, despite its huge electrical conductivity, the Seebeck coefficient is extremely low, due to the absence of a band gap (semimetallic behaviour). However, graphene nanoribbons are semiconductors because a band gap is opened through the presence of confinement effects. This is why graphene nanoribbons are also promising for thermoelectric applications [91]. Hence, the study of methods to reduce the lattice thermal conductivity is a promising research field[4].

3) According to the Wiedemann-Franz law, an extremely high electrical conductance implies a very high thermal conductance contributed by electrons. Furthermore, the phonon contribution to the thermal conductance is extremely high as well.

[4]For example, Cheng *et. al.* proposed the use of heavy adsorbed atoms and nanopores to enhance the thermoelectric properties of graphene nanoribbons, predicting a ZT value of 3 at low temperature (T=40 K) [9]

Its extremely high electrical and thermal conductance make graphene a material full of interest for electronics and heat removal applications. Even if an ideally infinite graphene sheet is unsuitable for thermoelectrics, its study is interesting to better understand the thermoelectric properties of its derivatives. The presence of extensive studies make it a valuable reference for testing the procedure that will be applied to the study of single-layer TMDCs.

4.1.2 Phonon Dispersion Relation and Phonon Density of States

To compute the phonon dispersion relation, a 5x5x1 supercell has been used (see fig. 4.1). Such a large supercell was required in order to reproduce the correct parabolic trend of the out-of-plane acoustic phonon mode (ZA) close to the Γ point. Indeed, the forces between the two C atoms in the primitive cell and those in the outer shells, even if very small, cannot be approximated to zero. Calculations both with SIESTA and VASP were performed with a 3x3x1 supercell, but the ZA mode displayed a linear dispersion relation at low frequencies and negative eigenvalues for q-points in the neighbourhood of the Γ point.
The forces have been measured as described in Ch. 1.3. The displacement of the atoms was 0.04 Bohr (1 Bohr = 0.529177249 $\AA$) and all the mesh parameters in direct and reciprocal space were the same as in the structure optimization run.

The phonon dispersion relation is plotted in fig. 4.3 along the path in the first Brillouin zone connecting the high symmetry points $\Gamma - M - K - \Gamma$.

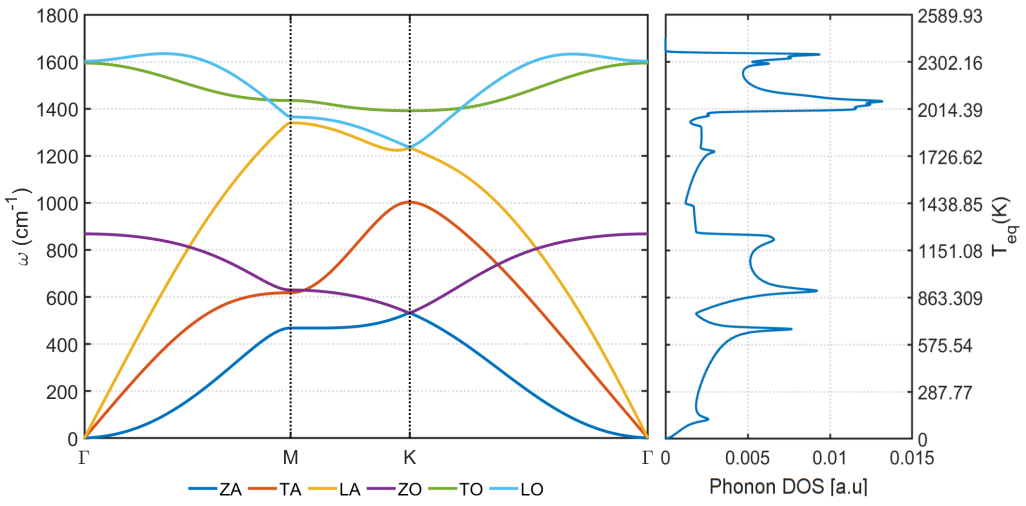

Figure 4.3: Phonon dispersion relation of graphene.

Figure 4.4: Oscillation patterns for the six normal modes of graphene at the Γ point.

	ZA	**TA**	**LA**	**ZO**	**TO**	**LO**
Γ	0	0	0	868	1602	1602
K	534	1003	1237	534	1391	1237
M	468	629	1340	629	1435	1365

Table 4.1: Phonon frequencies in cm^{-1} *of the six modes at the Γ, K and M points. These values are in good agreement with other theoretical and experimental data (see ref. [48] for a comparison).*

Considerations about the phonon dispersion relation are listed here:

1) The out-of-plane ZA mode shows a parabolic trend in the neighbourhood of the Γ point, due to the 2D nature of graphene. In fact, in the long wavelength limit, the propagation of phonons in the out-of-plane direction is unexpected, since it would consist in a "vertical jump" (translation) of the monolayer.

2) The group velocities for the acoustic modes in proximity of the Γ point (speeds of sound) are reported in tab. 4.2.

	ZA	**TA**	**LA**
This thesis	0.07	14.20	23.27
Experimental, EELS (Ref. [52])	0	≈14	≈24
Ab initio, LDA (Ref. [63])	0	18	24
MD, Tersoff potential (Ref. [104])	≈0	18.0	23.4

Table 4.2: Sound velocities in km/s for the acoustic modes in graphene. The results of this thesis are compared with other experimental ant theoretical estimates.

The sound velocities calculated in this thesis are in good agreement with the values that can be extracted from the experimental data of ref. [52]. TA and LA modes have very high speed of sound and their dispersion relation is linear in a large range of frequencies. Thus, according to the Debye model, a high thermal conductance is expected, due to the high speed of sound of in-plane acoustic modes.

3) Following the same argument, the ZA mode would give a negligible contribution to thermal transport since its sound velocity is about zero. Only a full band treatment can highlight its contribution.

4) At low temperature, only the low frequency phonons are occupied. As a consequence, the thermal transport will be dominated by the acoustic modes. The ZO mode is the first optical mode to be populated, while TO and LO are high in frequency and start to be populated only at high temperatures.

5) The contribution of the optical modes could be relevant only at high temperatures. The propagation of optical phonons is further reduced by Umklapp scattering. This is especially true in absence of a frequency gap, as it will be explained when the case of TMDCs will be treated. A confirmation of this observation will also come from the calculation in Ch. 6, where the effect of Umklapp scattering is evaluated.

6) There is no frequency gap between the acoustic and the optical modes, since the out-of-plane optical mode (ZO) crosses the acoustic branches. This can be seen also by observing the DOS, which was computed considering the whole Brillouin zone. The absence of a frequency gap can be explained by the fact that the basis of graphene is made of two atoms of the same element. It will be shown that a gap is present in TMDCs.

7) At the K point there is a degeneracy between ZA and ZO, and between LA and LO.

The consistency of these results was confirmed by a comparison with the phonon dispersion relation obtained by a calculation with the VASP package[5], which proved that the procedure and the parameter used for the calculation are reliable and transferable for successive calculations.

4.1.3 Phonon Transmission

As discussed in Ch. 2.3.2, the transmission function is the key quantity to investigate the phonon transport within the Landauer formalism. The first step to derive it consists in choosing a transport direction. For graphene and TMDCs, which possess a honeycomb-like atomic structure, the conventional directions are the Armchair and the Zig-Zag ones (fig. 2.7). In this thesis, all the transport calculations refer to the Armchair direction[6]. The unit cell for the calculation is different from the primitive unit cell used to investigate the phonon properties in the previous section. As a matter of fact, a conventional unit cell must be chosen so that the primitive vector coinciding with the transport direction is orthogonal to the other two. Thus, a unit cell of rectangular section with a basis of 8 atoms was used (fig. 4.5). As convention, the transport direction coincides with the z axis and the in-plane vector, perpendicular to the transport one, coincides with the x axis.

[5] courtesy of Silvana Radescu

[6] Test calculations were performed by C. Adessi also with respect to the Zig-Zag direction, finding very similar transmission functions (private communication). Thus the thermal conductance is considered nearly isotropic.

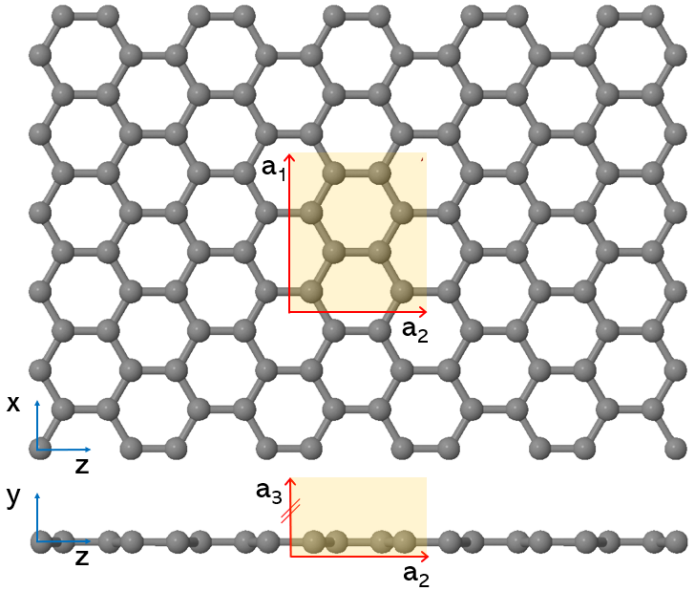

Figure 4.5: Frontal and side views of the 3x1x5 supercell used for the transmission calculation. The primitive cell, having a basis of 8 carbon atoms, is highlighted in yellow.

The atomic structure was relaxed up to forces less than 10^{-4} eV/Å and stresses less than 10^{-4} eV/Å^3. A direct space mesh with energy cutoff of 600 Ry and the Monkhorst-Pack scheme with 10x1x10 k-points were used, both for the unit cell optimization and for the calculation of the forces.
A 3x1x5 supercell was taken to measure the interatomic forces. The choice of the supercell is different from the one used to obtain the phonon dispersion relation in the previous section. The reason lies in the greater number of atoms composing the basis (8 vs the previous 2) and in the requirement of having dimensions along the z and x directions as similar as possible. The atoms' displacements corresponds to 0.04 Bohr.

The transmission shown in this section for pristine graphene is equivalent to the density of modes, since the phonon transport is studied in ballistic regime:

$$\bar{T}(\omega) = M(\omega)\mathcal{T}_{L_z}(\omega) \xrightarrow{\text{Ballistic}} M(\omega) \tag{4.3}$$

where $M(\omega)$ is the density of modes (DOM) and $\mathcal{T}_{L_z}(\omega)$ is the transmission coefficient accounting for inelastic scattering phenomena, which reads[7]:

$$\mathcal{T}_{L_z}(\omega) = \frac{\Lambda(\omega)}{L_z + \Lambda(\omega)} \xrightarrow{\text{Ballistic}} 1 \tag{4.4}$$

being the phonon mean-free-path for backscattering $\Lambda(\omega) \to \infty$ in ballistic regime. Having found out the phonon dispersion, the DOM was calculated within the Landauer formalism with the "counting bands" method, as explained in Ch. 2.3.2. The computation based on the Green's function

[7] A detailed explanation of this formula is provided in Ch. 3.

formalism, which is essential to deal with disordered systems, gave us the same result (the equivalence of the two formalisms is shown in [28]).

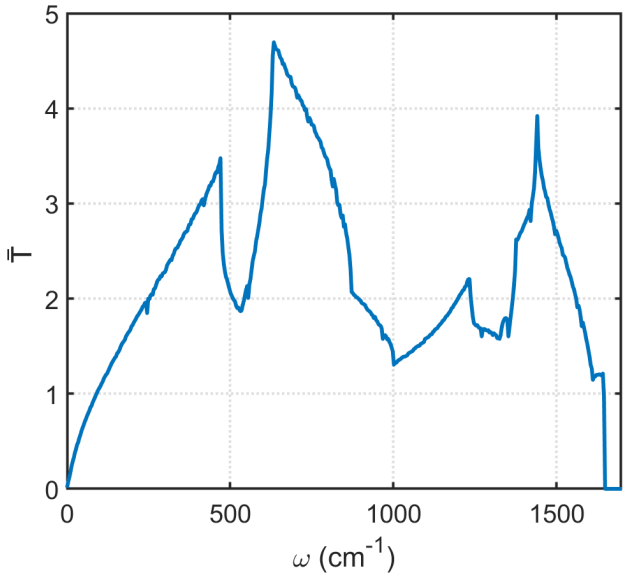

Figure 4.6: Phonon transmission of pristine graphene in ballistic regime.

The maximum frequencies of both the acoustic and optical modes are high and there is no frequency gap. Therefore a large thermal conductivity is expected, confirming what was already observed from the phonon dispersion relation. In this context, it is worth to highlight that, in ballistic regime and at high temperatures, the optical modes contribute significantly to the thermal transport.

4.1.4 Phonon Thermal Conductance

At this point, the conductance can be computed as:

$$C_{ph}(T) = \frac{\hbar^2}{8\pi k_B T^2} \int_0^\infty d\omega M(\omega) \frac{\omega^2}{\sinh^2(\frac{\hbar\omega}{2k_B T})} \tag{4.5}$$

Dividing C_{ph} by the width of the unit cell, L_x the conductance per unit width G_{ph} is obtained (fig. 4.7).

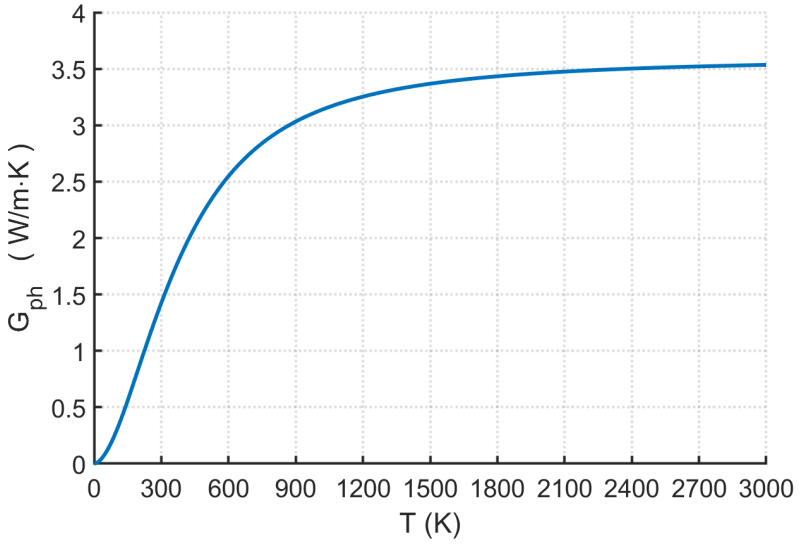

Figure 4.7: Phonon thermal conductance per unit width of graphene in ballistic regime.

Through the observation of the conductance trend as a function of the temperature, one can note that:

1) In the low temperature limit the thermal conductance increases rapidly with increasing temperature as more and more phonons are populated.

2) The growth is much faster until $\sim$ 700 K because the acoustic modes give the greatest contribution. A saturation value of about 3.5 W/(m·K) is reached when all the modes are populated.

3) Since there are no scattering mechanisms included, the conductance does not show a decreasing trend at high temperature. This is a limitation of all the models which analyse the thermo-electronic transport phenomena at high temperatures in ballistic regime. To go beyond this approximative treatment, the effect of Umklapp phonon-phonon scattering will be included in Ch. 6.

4) The conductance per unit width at room temperature is 1.4 W/(m·K). A trend proportional to $\sim T^2$ is observed at very low temperatures. This is a typical feature of 2D materials, while in bulk the low-temperature thermal conductivity is proportional to $\sim T^3$. The difference in the temperature dependence between 2D and 3D materials is related to the different phonon density of states. [47]

4.2 Transition Metal Dichalcogenides: a Comparison among Monolayers of MoS_2, WS_2, $MoSe_2$ and WSe_2

The thermoelectric properties in ballistic regime of SL TMDCs like MoS_2, WS_2, $MoSe_2$ and WSe_2 were analysed and compared. Unlike graphene, where all the C atoms lay in the same plane, TMDCs have a structure made of a layer of M atoms sandwiched between two layers of X atoms.
The unit cell used to investigate the electronic properties and the relative supercell for the phonon dispersion relation step is shown in fig. 4.8. The interatomic distance between two metal atoms d_{M-M} obtained from the calculations are reported in tab. 4.3. As for graphene, the conventional first Brillouin zone of monolayer TMDCs has an hexagonal shape.

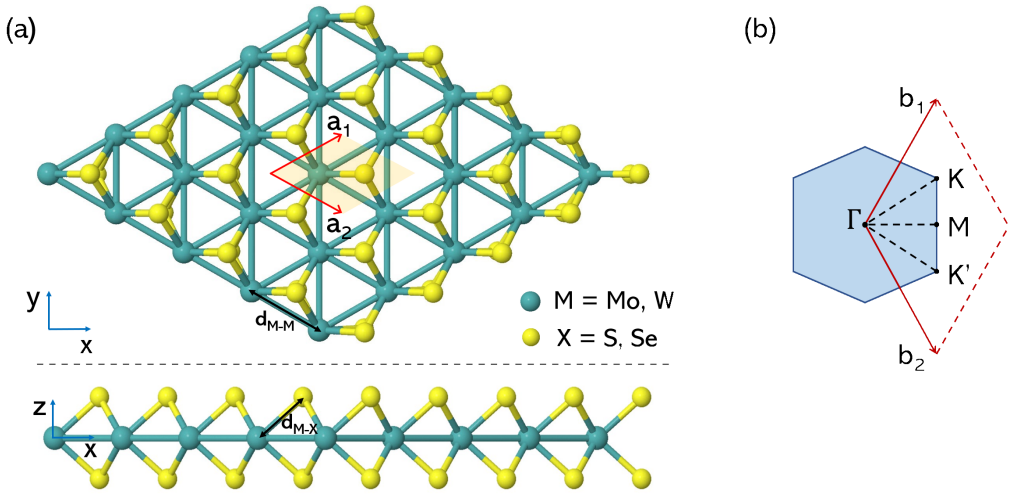

Figure 4.8:
(a) Frontal and side view of the unit cell and of the 5x5x1 supercell used for the computation of the phonon dispersion relation. The unit cell, highlighted in yellow, coincides with the primitive cell of the lattice.
(b) First Brillouin zone, with its high symmetry points and the reciprocal vectors (b_1,b_2).

Table 4.3: Interatomic distances ($d_{M\text{-}M}$) in Å:

	MoS_2	WS_2	$MoSe_2$	WSe_2
This thesis	3.20	3.25	3.33	3.36
Theoretical (ref. [88])	3.179	3.183	3.309	3.319
Experimental (ref. [88])	3.160	3.150	3.289	3.282

The optimized equilibrium lattice constants are slightly larger than the values measured experimentally. Indeed, the generalized gradient approximation for the exchange-correlation functional usually overestimates the lattice constants [56].

4.2.1 Electronic Band Structure and Density of States

A set of calculations have been performed to identify the parameters which allow an optimal convergence for all the four materials studied. The atomic structures were optimized up to forces less than 10^{-4} eV/Å and stresses less than 10^{-4} eV/Å^3 . The Monkhorst-Pack scheme [45] was used for the integration of the Brillouin zone with a k-mesh of 10x1x10 k-points, while a mesh with energy cutoff of 1000 Ry has been used for integrals in direct space.

The electronic band structures for the four TMDCs are plotted along the path in the first Brillouin zone connecting the high symmetry points $\Gamma - M - K - \Gamma$. These plots are limited in the energy range of interest near the Fermi level (E_f), which is the relevant one for transport properties. On the right, it is shown the density of states (DOS), computed by using a mesh of 100x1x100 k-points, and the projected density of states (PDOS). The PDOS gives important information on the contribution of the different atomic species to the band structure.[8]

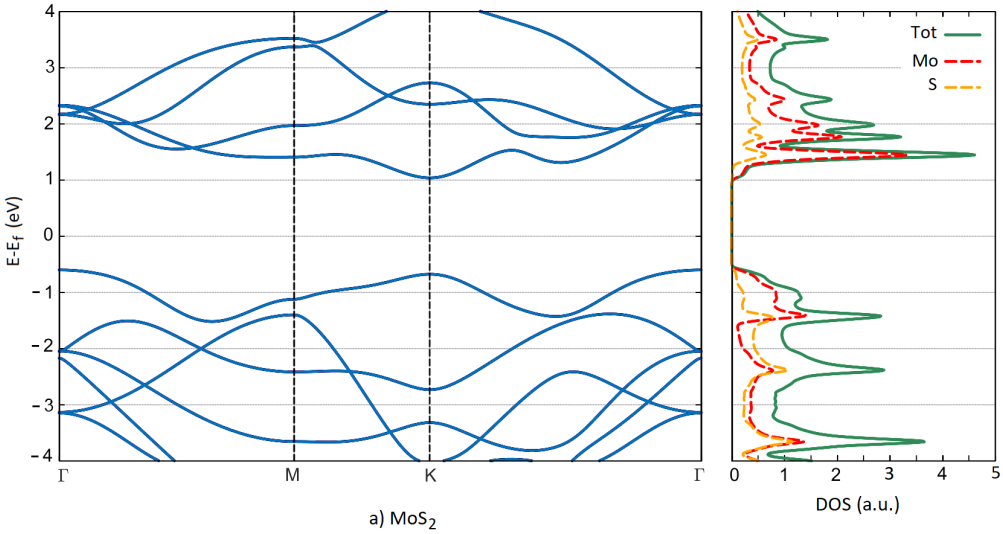

[8]The contribution of the two X atoms is equivalent for symmetry, thus the PDOS is plotted for only one of them. Hence, the total DOS (green line) is the sum of the M contribution (red line) and the double of the X contribution (yellow line).

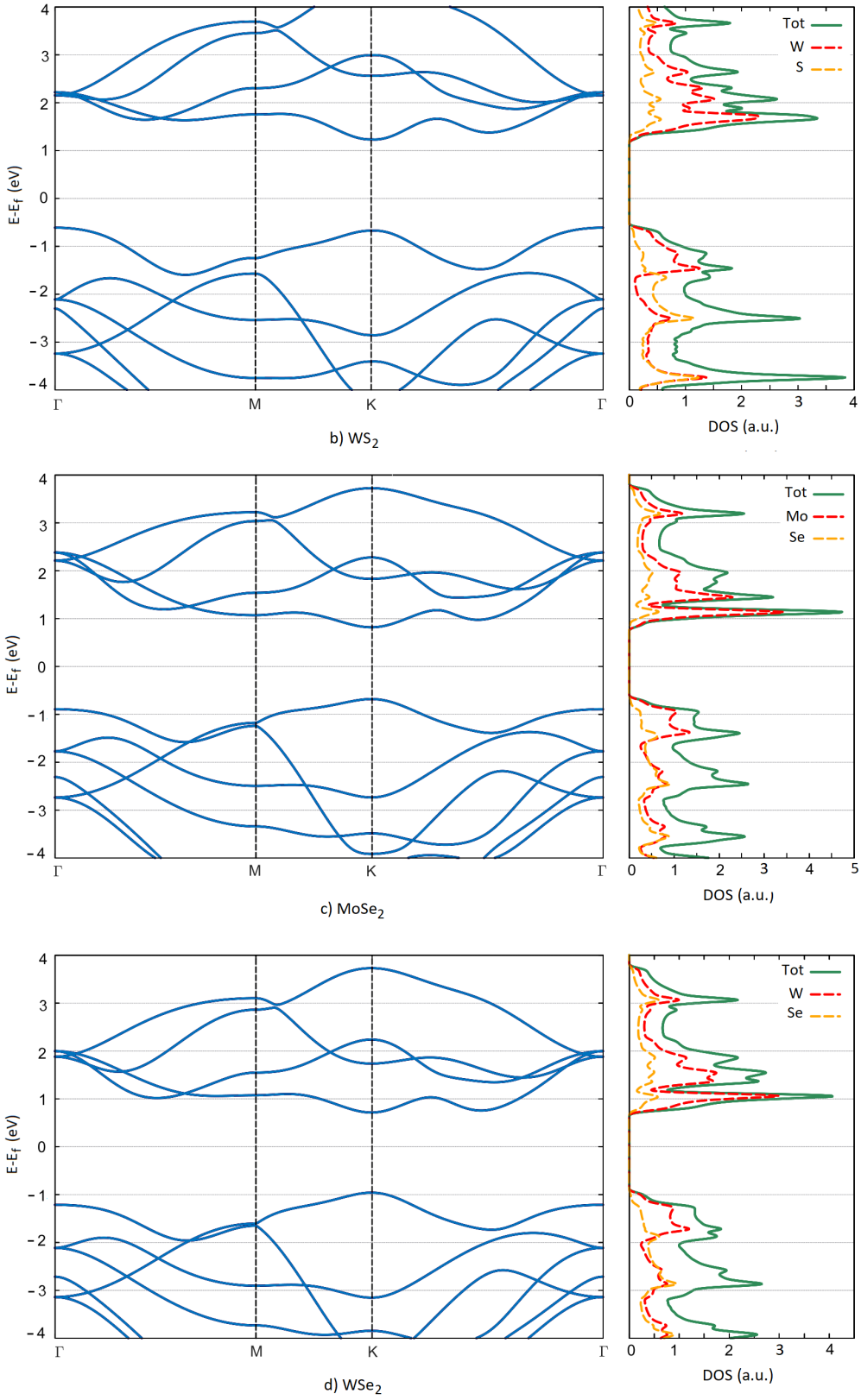

Figure 4.9: Electronic band structure and density of states of MoS_2 (a), WS_2 (b), $MoSe_2$ (c), WSe_2 (d) monolayers. Bands are plotted in proximity of the Fermi level.

The following considerations can be derived by the plots of the electronic band structures:

1) Single-layer TMDCs are direct semiconductors, which is really important for optoelectronic applications. On the contrary, bulk materials are indirect semiconductors [88].

2) The band gaps are not well reproduced by *ab initio* calculations with GGA (PBE) functional. In fact, the predicted values are lower than the experimental data reported in tab. 4.4. In addition, the inclusion of the spin in the calculations would lead to a splitting of the valence band at the K and K' points of the BZ due to the strong spin-orbit coupling in TMDCs [68]. In any case, this is irrelevant for the purpose of this work, since we are not interested in optical transitions. Indeed, the exact magnitude of the gap has no effect on the thermo-electric transport properties. The band gap is large enough that the thermo-electric transport properties are affected uniquely by the shape of the conduction and valence bands in an energy range close to the Fermi level.

	MoS_2	WS_2	$MoSe_2$	WSe_2
This thesis	1.70	2.20	1.48	1.69
Experimental	1.90 (2.05)	1.95 (2.36)	1.66 (1.85)	1.64 (2.04)
Ab initio	1.60 (1.75)	1.57 (1.97)	1.37 (1.56)	1.25 (1.71)

Table 4.4: Band gap energies (eV) between the valence (v) and the conduction (c) band, corresponding to the vertical transition at the K point. The results of this thesis are compared with the ab initio *(GGA-PBE functional) and experimental data reported in ref. [88]. In this work the authors evaluated the splitting of the valence band at the K point due to the strong spin-orbit coupling. The two values associated to each material refer to the transitions* $K_v \rightarrow K_c$ *and* $K'_v \rightarrow K_c$.

3) From the PDOS, it can be seen that, at the bottom of the conduction band and at the top of the valence band, the total DOS is contributed mainly by the transition metal atoms (Mo and W). These states immediately above and below the energy-gap are those available for free electrons and holes to conduct. Therefore, the contribution of chalcogen atoms (S and Se) to the electrons transport is expected to have a secondary impact with respect to the transition metal one. This opens the way to defect engineering: the insertion of S or Se vacancies is expected to slightly affect the electronic transport properties (i.e. the electric conductance G_{el} and the Seebeck coefficient).
The electrical conductivity, Seebeck coefficient and power factor were calculated in a previous work by Adessi *et. al.* [1] and they are presented in fig. 4.10

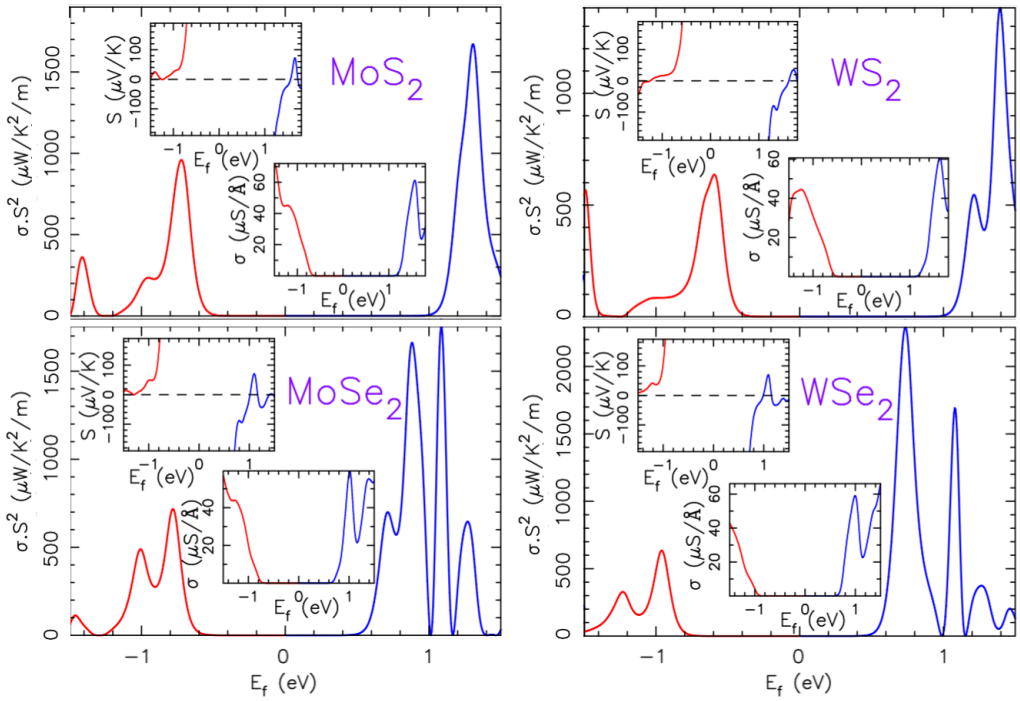

Figure 4.10: Adessi et. al. [1] : Powerfactor for MoS_2, $MoSe_2$, WS_2 and WSe_2 monolayer in ballistic regime. In inset is given the Seebeck coefficient S and the electrical conductivity . Red and blue curves correspond respectively to hole and electron doping. Calculations performed for the armchair transport direction.

4.2.2 Phonon Dispersion Relation and Phonon Density of States

To compute the phonon dispersion relation, a 5x1x5 supercell (75 atoms) has been used (see fig. 4.8). The atoms' displacement was 0.04 Bohr and the mesh parameters in direct and reciprocal space were the same as in the structure optimization run.
The phonon dispersion relations for MoS_2, WS_2, $MoSe_2$ and WSe_2 are plotted along the path $K - M - \Gamma - K$ in the first Brillouin zone (fig. 4.15).

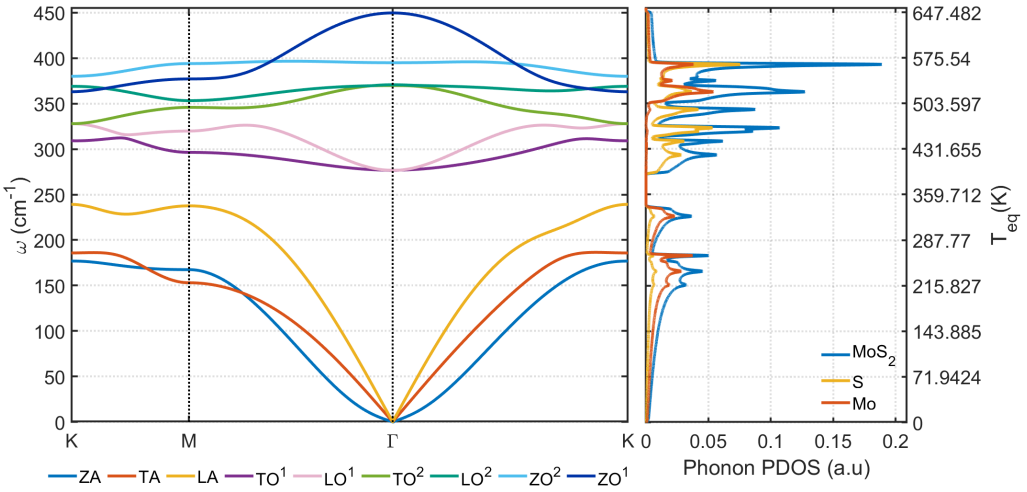

Figure 4.11: Phonon dispersion relation and projected density of states of MoS_2 monolayer.

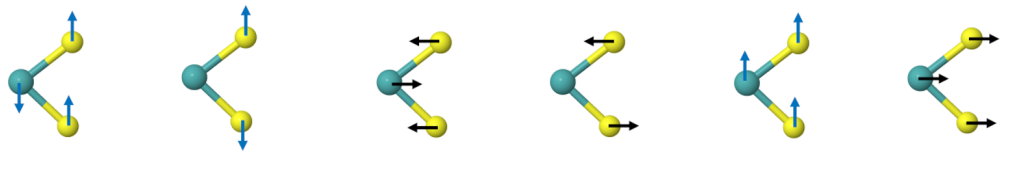

Figure 4.12: Oscillation patterns for the vibrational modes of TMDCs at the Γ point. The mode frequencies of MoS_2 at the Γ point are provided. A_1 and $A_2^{"}$ are out-of-plane modes, while $E^{'}$ and $E^{"}$ are in-plane modes. IR and R denote infrared- and Raman-active modes respectively.

The results listed in tab. 4.5 are in perfect agreement with the calculation of ref. [56], in which the generalized gradient approximation (GGA) was employed as well. The small deviations from experimental measurements are caused by the overestimation of the lattice constant, which is a consequence of the GGA.

	A_1	$A_2^{"}$	$E^{'}$	$E^{"}$
This thesis	450.0	395.0	370.8	276.6
Ab initio	458.24	397.63	373.34	276.72
Experimental	470	402.4	383.5	287

Table 4.5: Phonon frequencies in cm^{-1} of the optical modes of MoS_2 at the Γ point. The results from this thesis are compared with other numerical [56] and experimental [29, 89, 60] data.

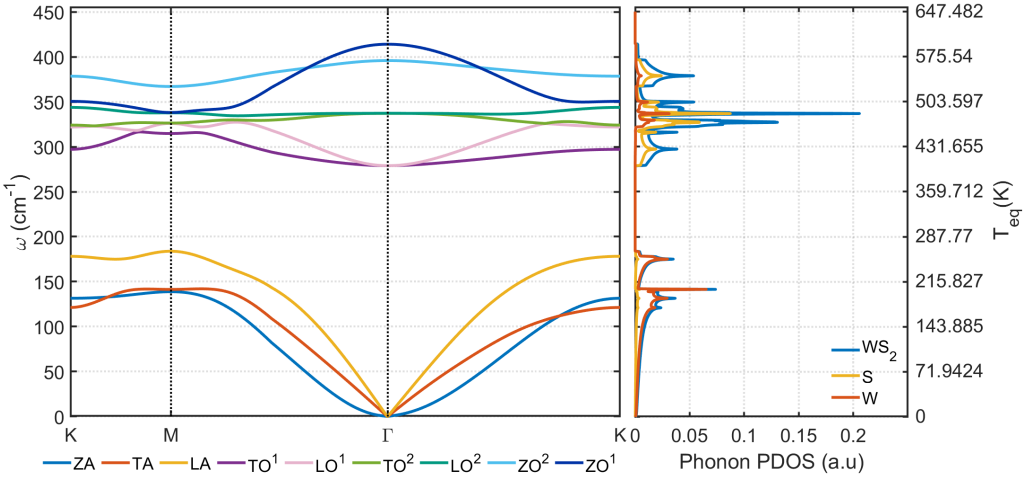

Figure 4.13: Phonon dispersion relation and projected density of states of WS_2 monolayer.

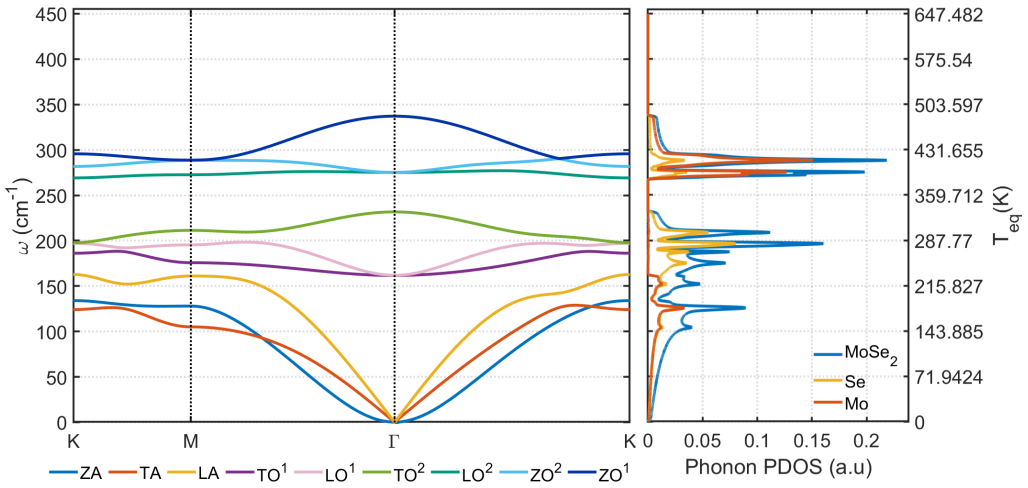

Figure 4.14: Phonon dispersion relation and projected density of states of $MoSe2$ monolayer.

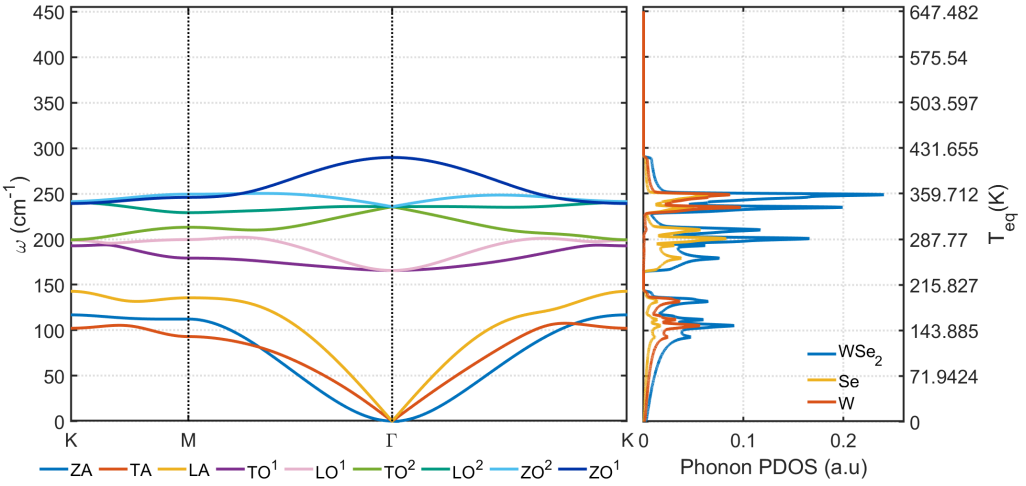

Figure 4.15: Phonon dispersion relation and projected density of states of WSe_2 monolayer.

A series of important considerations are provided by looking and comparing the phonon dispersion relations in the figures above. Firstly, the difference between acoustic and optical modes is evident and, diversely from graphene, a frequency gap is present. There is one question that must be asked: is it possible to predict the contribution of the modes to the thermal conductivity? The following qualitative considerations based on the simple Debye model may be advanced:

1) Acoustic phonons are coherent displacements of the atoms in the lattice. If these collective movements propagate in the transport direction, they will contribute significantly to the thermal conductivity. At very low frequencies, the out-of-plane ZA mode is not as effective as TA and LA modes in transporting heat in 2D materials. Indeed, as seen for graphene, the ZA mode has a parabolic trend in the neighbourhood of the Γ point, with zero speed of sound. A completely coherent transport in the out-of-plane direction is meaningless, since it would signify the propagation of a mechanic wave in the vacuum. However, it is important to remember that this observation is correct only in the neighbourhood of the Γ point, corresponding to the long wavelength limit, where in fact the group velocity tends to zero because of the parabolic trend. On the contrary, at higher frequencies, the ZA mode does contribute to the thermal transport. In fact, the interatomic force constants in the three cartesian directions are coupled.
   Studying the propagation of the ZA phonons within the simple Debye model would result in taking into account only the group velocity at the Γ point (speed of sound), which tends to zero because of the quadratic nature of the dispersion relation. Therefore, it would lead to a big underestimation of its contribution to the thermal conductance.
   Due to its lower group velocity, one may expect the contribution of the ZA mode to the thermal conductance to be less relevant than those of in-plane LA and TA modes. Nonetheless, this statement is correct only if

one considers the ballistic regime and the harmonic approximation. For example, in ref. [102] it is proved that, in the case of WSe_2, ZA phonons have the dominant contribution to the thermal conductivity. As a matter of fact, including phonon-phonon inelastic scattering in the analysis, ZA phonons show a longer life time than TA and LA phonons.

2) Optical phonons are out-of-phase movements of the atoms in the lattice and they are not able to transport heat effectively. This is reflected in the fact that the optical modes are poorly dispersed. Their group velocity tends to zero close to the Γ point and is much lower than for LA and TA modes in all the Brillouin zone.

3) From the simple relation $\omega = \sqrt{\frac{C}{m}}$, higher frequencies are expected for atoms having stiff bonds (high spring constant C) and low atomic mass. High frequencies and a Debye-like dispersion relation are associated in turn to high group velocity and high thermal conductivity.
The bonding in single-layer molybdenum and tungsten dichalcogenides are surprisingly stiff. In general, the sulfides are 15% stiffer than the selenides, while the molybdenum dichalcogenides are 4% less stiff than tungsten dichalcogenides. [21]

4) The greater the mass difference between the M and X atoms of the basis, the greater the energy gap between acoustic and optical modes. Materials with a big gap will undergo less phonon-phonon Umklapp scattering: the scattering channel acoustic+acoustic→optical becomes ineffective due to the requirement on energy conservation for phonon-phonon scattering.
Therefore, we expect an impact on the studied materials due to the phonon-phonon Umklapp scattering, increasing in this order: WS_2, MoS_2, WSe_2, $MoSe_2$.
MoSe2 does not have a band gap between acoustic and optical modes, but in between the optical range.

5) Looking at the phonon PDOS plots in the acoustic range, one may notice that the greater the mass difference between the M and X atoms, the higher the contribution to the collective motion coming from the M atom and the lower from the X atom. The minimum difference corresponds to $MoSe_2$ (Mo = 95.95 amu, Se = 78.97 amu), for which the contribution of Mo and Se is almost the same. In agreement with this principle, in WS_2 (W = 183.84 amu, S = 32.06 amu) the contribution of W is way bigger than that from S.
In LO^1, TO^1 and TO^2 only the X atoms vibrate.
In LO^2, ZO^1 and ZO^2 both M and X contributions are relevant.
On the base of these information, it is natural to think that the introduction of X vacancies could strongly affect the phonon thermal transport. $MoSe_2$ may undergo the highest reduction in thermal conductivity due to the high contribution of Se to acoustic modes, which are the most important for heat transport.

Combining these observations with what was said about the minor importance that X atoms have on the electron transport, it seems like X-vacancy doping could be a promising way to improve the thermoelectric figure of merit.

4.2.3 Phonon Transmission

The orthogonal primitive cells used for computing the transmission of the four TMDCs were made of 12 atoms. To measure the interatomic forces, a 3x1x3 supercell was used (see fig. 4.16), and atomic displacements of 0.04 Bohr were used. The atomic structure was relaxed up to forces less than 10^{-4} eV/$\mathring{A}$ and stresses less than 10^{-4} GPa. A direct space mesh with energy cutoff of 1000 Ry was employed both for the unit cell optimization and for forces' calculation. The Monkhorst-Pack grid used had 10x1x10 k-points for the structure optimization and 4x1x4 for the calculation of the forces.

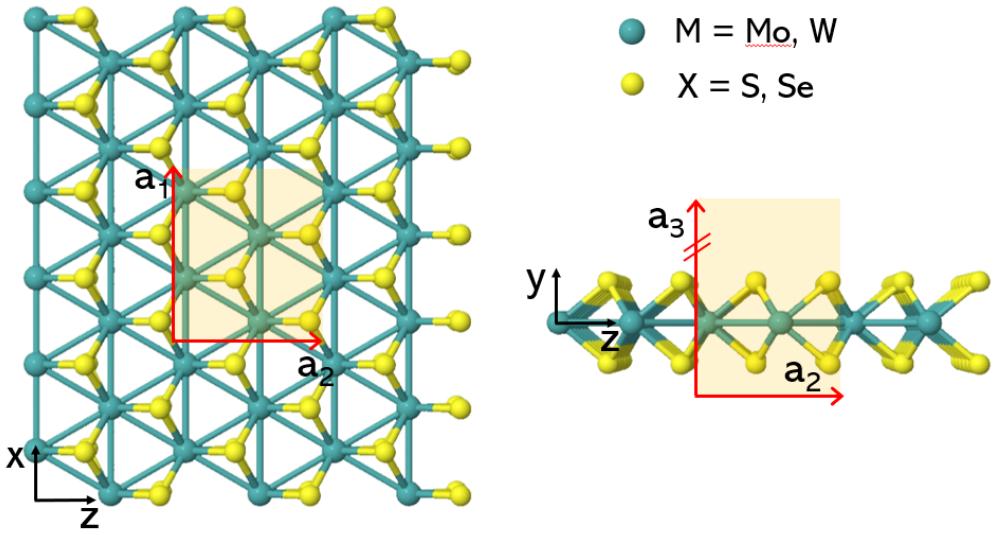

Figure 4.16: Frontal and side views of the 3x1x3 supercell used for the transmission calculation for SL TMDCs of the type MX_2. The primitive cell, having a basis of 4 M atoms and 8 X atoms, is highlighted with a shadowed square. The axis in the out-of-plane direction $\mathbf{a_3}$is interrupted for graphical reasons. It is in fact much longer than $\mathbf{a_1}$ nd $\mathbf{a_2}$ in order to reproduce the vacuum.

The transmission function for pristine SL TMDCs was computed in the armchair direction within the Landauer formalism. The procedure, which is the same used for pristine graphene, is described in Ch. 2.3.2.
Fig. 4.17 shows the transmission functions for MoS_2 (a), WS_2 (b), $MoSe_2$ (c) and WSe_2 (d).

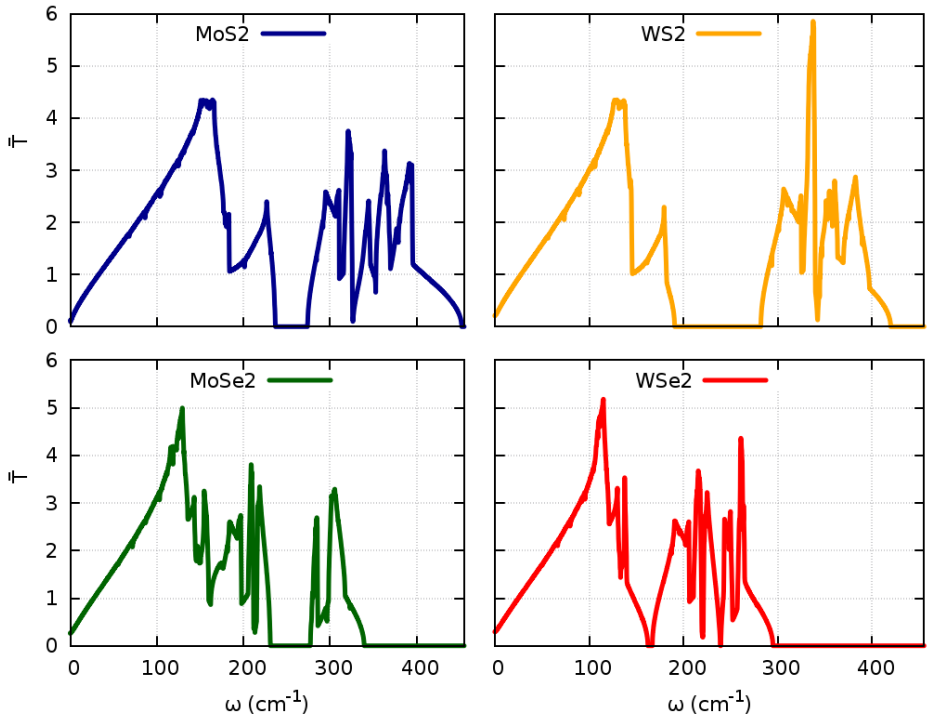

Figure 4.17: Phonon Transmission at T=300K for MoS_2 (a), WS_2 (b), $MoSe_2$ (c) and WSe_2 (d) monolayers. The transport direction is the armchair one.

4.2.4 Phonon Thermal Conductance

Knowing the transmission function, it is straightforward to compute the lattice thermal conductance per unit width via eq. 4.5.

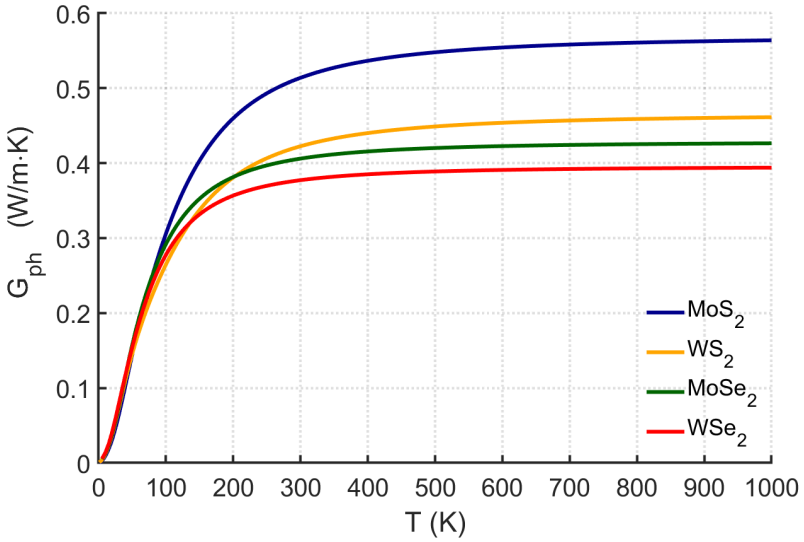

Figure 4.18: Phonon thermal conductance per unit width of MoS_2, WS_2, $MoSe_2$ and WSe_2 monolayers.

It is remarkable to note that the maximum values of the thermal conductance per unit width in TMDCs are much smaller than the one found in graphene: $0.39 - 0.56$ W/(m·K) and 3.5 W/(m·K) respectively. The difference is significant also at room temperature: $0.38 - 0.51$ W/(m·K) vs 1.4 W/(m·K).
Moreover, for TMDCs the thermal conductances grow rapidly with the temperature up until about 100 K before they slowly converge towards a saturation value. This trend is the consequence of the population of all the phonon branches at temperature lower than the room temperature. On the contrary, in graphene the rapid growth in thermal conductance continues up until about 700 K, meaning that at room temperature not all of the phonons are thermally activated.
The plot in fig. 4.18 allows to compare the conductance trends of the four pristine single-layer TMDCs:

1) At room temperature and above, WSe_2 is the material with the lowest conductance, followed by WSe_2, WS_2 and MoS_2, in increasing order. This comparison should be taken only as a qualitative evaluation, since it does not include the intrinsic reduction of the thermal conductivity due to phonon-phonon Umklapp scattering.
   By taking into account the Umklapp scattering[9], the following order was

[9]Including this inelastic scattering mechanisms, the transport regime is not ballistic any more. It follows that the conductance is dependent on the length of the device L_z, which should be determined. This makes also possible to evaluate the thermal

reported in ref. [21]: WS_2 has the highest thermal conductivity, 142 $W\,m^{-1}\,K^{-1}$ at room temperature, followed by MoS_2 (103 $W\,m^{-1}\,K^{-1}$), $MoSe_2$(54 $W\,m^{-1}\,K^{-1}$), and WSe_2 (53 $W\,m^{-1}\,K^{-1}$).
It is clear that going beyond the ballistic regime is necessary to be able to compare results from the simulations with the experimental values. For this reason, a procedure to evaluate the transition to diffusive regime, due to the intrinsic presence of Umklapp scattering, has been implemented and it is shown in Ch. 6.

2) All the studied bidimensional materials present the typical quadratic growth of G_{ph} in the low temperature limit. Then the trend becomes linear with the temperature up until T $\sim$ 100 K for TMDCs and T $\sim$ 500 K for graphene.

3) In an intermediate temperature range, the growth of the curves slows down due to the presence of the energy gap in between acoustic and optical modes. In this range of temperatures, the conductance still increases because it is related to the Bose-Einstein distribution (see fig. 2.11). Nonetheless, the number of states contributing to the conductance remains almost constant.
The heavier the masses of the atoms forming the basis, the lower the frequency corresponding to the onset of the gap; hence, the lower the temperature related to a slowdown of the conductance growth.
In particular, for T=150-250 K the conductances for selenides grow slower than for the sulfides because the acoustic modes extend in a frequency range up to an equivalent temperature of about T=150 K.
In addition, for T=100-300 K the conductance for WS_2 shows a significantly lower increase than that for MoS_2. Indeed, W is heavier than Mo, being the reason for the frequency gap in WS_2 to start at lower frequency ($\sim$ 180 cm^{-1}) than in MoS_2 ($\sim$ 240 cm^{-1}). Despite an increase in temperature, there are not states which could be occupied in that energy range.

4) At higher temperatures, the conductances continue to grow because the highest frequency optical phonons are populating. However, their contribution is less relevant than that coming from the acoustic modes. This is why the growth is very slow. Finally, when all the phonon states are occupied, a saturation value is asymptotically reached.

conductivity (in ballistic regime we are instead considering the conductance per unit width).

Chapter 5

Effects of a Disordered Distribution of Defects: The Impact of Sulphur Vacancies on the Phonon Thermal Conductivity of SL MoS_2

Defect engineering is one way to improve the figure of merit of materials by manipulating the type, concentration, spatial distribution, or mobility of defects within a crystalline solid [65].
The aim is to hinder the phonon transport by introducing defects in the pristine lattice such as substitutional atoms, adsorbed dopants and vacancies, without affecting the electrical transport properties.
The influence of substitution and adsorption doping in monolayer TMDCs on the Seebeck coefficient, electrical conductance and power factor has been examined by Adessi *et al.* in [1]. In this work, the electrical properties were studied by analysing the impact of substitutional impurity atoms (Cl and P) and adsorbed alkalies (Li, Na, K and Rb) on the electronic band structure. The results highlighted a reduction of the power factor (PF) with respect to calculations based on the rigid band model[1].
It was found that the substitution doping mechanism by chloride induces local states at the Fermi level, leading to a poor PF at low dopant concentration. In contrast, alkalies act as almost perfect electron donors; the band structure at the Fermi level is very similar to the band structure of the pristine TMDCs layer. However, due to a degeneracy removal phenomenon, the PF obtained with alkali doping is not as large as the one obtained within the rigid band model.
This study stated that the highest power factor is expected for adsorbed potassium atoms.

[1]This kind of modelling starts from the pristine layer properties and introduces the effect of doping by shifting rigidly the Fermi level of the system. When the Fermi level is shifted towards the valence band it mimics hole doping. When shifted towards the conduction band it mimics electron doping.[1]

In addition, Chee *et al.* [10] showed that the electrical and optical properties of WS_2 and MoS_2 can be modulated in a reversible and controllable way via hydrazine doping and sulphur annealing. Hydrazine treatment of WS_2 resulted to improve the field-effect mobilities, on/off current ratios, and photoresponsivities of the devices. This behaviour was attributed to the surface charge transfer doping of WS_2 and to the sulfur vacancies formed by its reduction[2], which results in an n-type doping effect. In previous studies, Lauhon *et al.* demonstrated that the field-effect mobility of MoS_2 is enhanced due to an increase in electron doping related to higher concentration of sulphur vacancies[33].
Furthermore, Tosun *et al.* [78] studied defect engineering in the fabrication process flow of WSe_2 n-type metal-oxide-semiconductor field-effect transistors. A mild plasma treatment (He or H_2) was used as an approach to reduce the contact resistance of WSe_2, by selective creation of anion vacancies at the metal contact regions. Material characterization by X-ray photoelectron spectroscopy, photoluminescence, and Kelvin probe force microscopy confirmed defect-induced n-doping, which is attributed to the creation of anion (Se) vacancies.
In Ch. 4, it was noticed that the electrical transport properties of MoS_2 are dominated by the contribution of Mo atoms. Moreover, the contribution of Mo and S atoms on the phonon transmission is split in this way: both the atoms give a similar contribution to the transport of acoustic phonons, while the S atoms have the prevalent impact on the optical modes.
From these qualitative observations, it was hypothesized that the introduction of S-vacancies in the lattice could open the way for decreasing the thermal conductivity without affecting significantly the power factor.
The aim of this chapter is to investigate in a quantitative way the effect of a disordered distribution of sulphur vacancies on the phonon transport in MoS_2.

5.1 Introduction of a Single Sulphur Vacancy in the Pristine Lattice

The first step of the analysis consists in inserting a single S vacancy in the unit cell of the material. This unit cell must be large enough so that the concentration of the S vacancies remains realistically low. In this way, the defect affects solely the neighbouring atoms, modifying the properties of the material only locally.
Fig. 5.1 shows a representation of the unit cell for the structure relaxation run and of the supercell for the calculation of the forces.

[2]This reaction can be described by: $N_2H_4 + WS_2 \rightarrow WS_{2-x} + N_2 + 2H_2S$

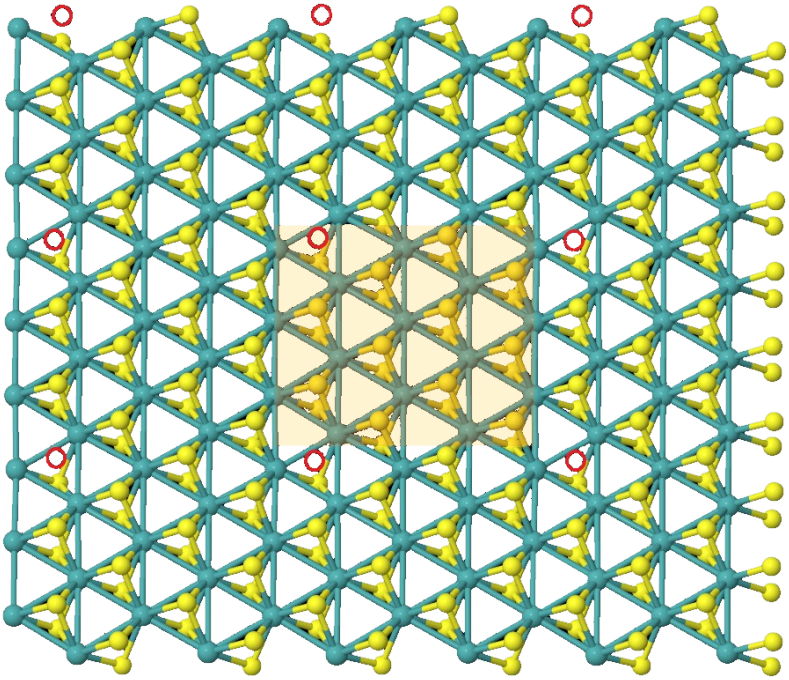

Figure 5.1: Prospective view of the 3x1x3 supercell used for the calculation of MoS_2 with a sulphur vacancy. The unit cell, highlighted with a yellow square, is made of 35 atoms: 12 Mo, 23 S. The sulphur vacancy is marked with a red circle.

The concentration of defects is $x = 9.7190 \cdot 10^{13}$ cm^{-2}, corresponding to a single S-vacancy over a cell of 36 atoms.
Since the systems are treated within DFT by applying periodic boundary conditions, it is important to realize that the defect in the unit cell is repeated in a periodic way as well. As a matter of fact, the calculation shown in this section is not suitable to analyse the impact of a real distribution of vacancies. It will be clear soon that this kind of calculation consists in one of the steps necessary to treat a disordered distribution of defects by using the Green's functions technique.
At this first stage, the transmission is computed with the "counting bands" method. The transmission function and the conductance of this "single-vacancy" monolayer are plotted in fig. 5.2 and fig. 5.3, where they are compared with the curves for pristine MoS_2 obtained in the previous chapter.

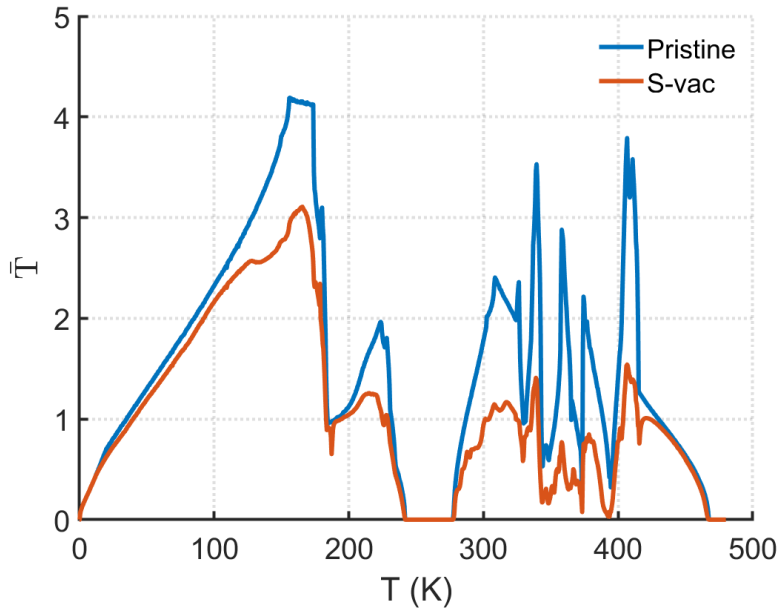

Figure 5.2: Phonon transmission of MoS_2 in presence of a single sulphur vacancy (red) and pristine material (blue).

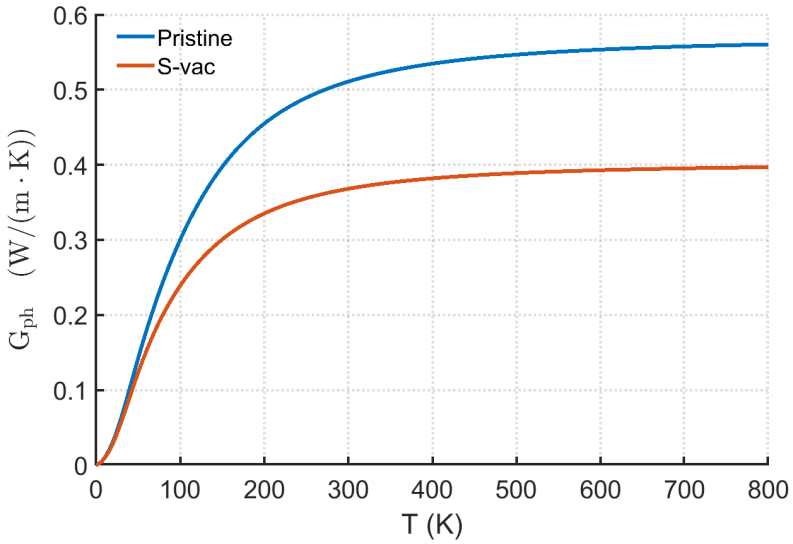

Figure 5.3: Thermal conductance per unit width of MoS_2 in presence of a single sulphur vacancy (red) and pristine material (blue).

It is clear that the introduction of the sulphur vacancy significantly reduces the transmission, especially in the optical range. Consequently, also the phonon thermal conductance is strongly affected by the presence of the defect.

A Technical Note on the Employed Basis Set

The calculations presented in this chapter were obtained using the same procedure and tolerance parameters for the structure optimization and the forces calculation as in the previous chapter about pristine materials. The only difference was the use of a single zeta polarized basis set (sζp). This choice provides a slightly less accurate phonon dispersion and, in turn, a transmission that is altered to a small degree (fig. 5.4). However, it does not affect the thermal conductance curve, which is the final aim of the calculation. In fact, fig. 5.5 demonstrates that the curve of $G_{ph}(T)$ is left unaltered whether a dζp or a sζp basis is employed.

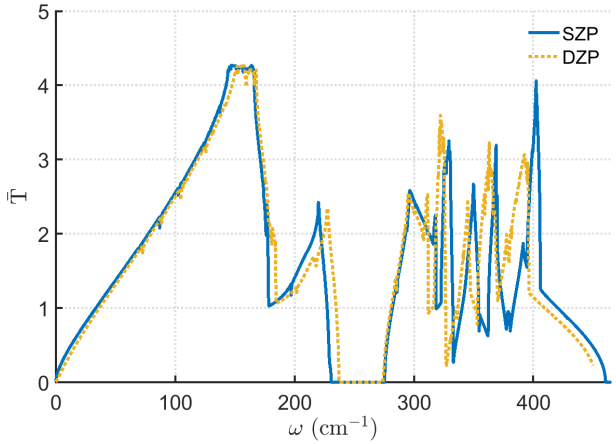

Figure 5.4: Comparison of the transmission of pristine MoS_2 calculated with a single zeta polarized basis(in blue) and a double zeta polarized basis (in yellow).

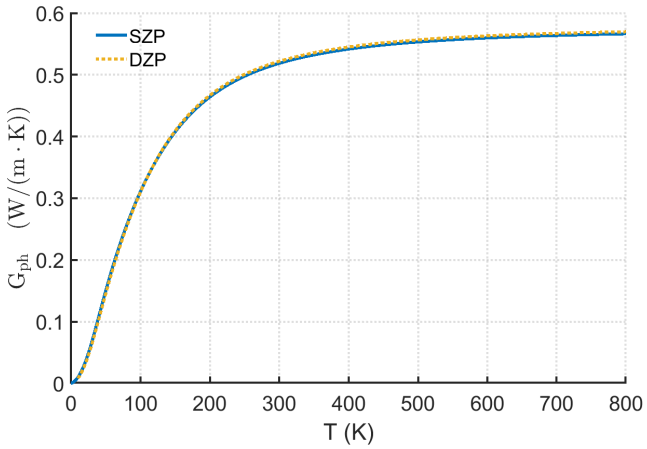

Figure 5.5: Comparison of the transmission of pristine MoS_2 calculated with a single zeta polarized basis (in blue) and a double zeta polarized basis (in yellow).

A slightly lower accuracy in the calculation is rewarded by a strong reduction in the computation time. The choice of a single zeta polarized basis was

fundamental to proceed with the analysis of the impact of a disordered distribution of defects, which required calculations with computation time in the order of a month.

5.2 Effect of a Disordered Distribution of Sulphur Vacancies in MoS_2

This section is devoted to the study of a disordered distribution of sulphur vacancies in MoS_2.
In order to deal with disorder, the approach used in the previous section is insufficient. In fact, the periodical symmetry of the lattice is broken by the introduction of defects in randomised sites. Thus, the "counting bands" method employed so far would fail and the use of the Green's functions technique becomes necessary.
A schematic representation of the studied systems is drawn in fig. 5.6. The semi-infinite contacts are made of pristine material, while the device is composed by a series of blocks. There are five different kinds of blocks; each one represents a different unit cell.

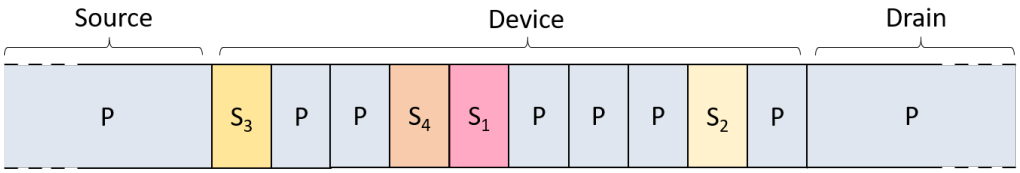

Figure 5.6: Device with a disordered distribution of defects. P stands for a "pristine block", i.e. a monolayer without defects, and S_i stands for a monolayer whose unit cell present an S vacancy in a lattice site labelled as i.

The pristine material corresponds to the P block and, it is the constituent of the semi-infinite contacts as well.
The other four blocks are related to unit cells which present a single S vacancy in four different locations of the lattice.
Several calculations were performed to compute the transmission of all the sub-systems of the type P-S_i and P-S_i-P.
The difference with respect to the "single-vacancy" case, which was treated in the previous section, consists in computing the Green's function of each sub-system. The total Green's function of the "many-blocks" device, and therefore the total transmission, is obtained the knowledge of the Green's functions of the "single-vacancy" systems.

Following this approach, two studies were conducted changing the configuration of the blocks which compose the device.
The first one consisted in an analysis of the lattice thermal conductivity as a function of the concentration of defects, when the length of the device was fixed to 42 nm.

The second one regarded the variation of the conductivity as a function of the length of the device L_z, when the concentration was fixed to $x = 3.3\%$. A code was written in order to produce these different configurations of the device. It generates random sequences of blocks with properties depending on two parameters: the total number of blocks, which determines the length of the device; the percentage of blocks containing sulphur vacancies, which sets the concentration of defects.
A statistical analysis was carried out by averaging several different configurations having the same characteristics.
The results are shown in the following.

5.2.1 Variable Concentration at Fixed Length ($L_z = 42$ nm)

The first study regarded a device of length $L_z = 42$ nm and concentration of sulphur vacancies equal to 0.8% ($9.7 \cdot 10^{12}$ cm^{-2}) and 3.3% ($3.9 \cdot 10^{13}$ cm^{-2}). These concentrations are in line with realistic values that can be obtained experimentally. Indeed, Tsai *et. al.* [81] induced sulphur vacancies in the basal plane of MoS_2 with concentrations in the range $0 - 21.9\%$ by electrochemical generation[3].

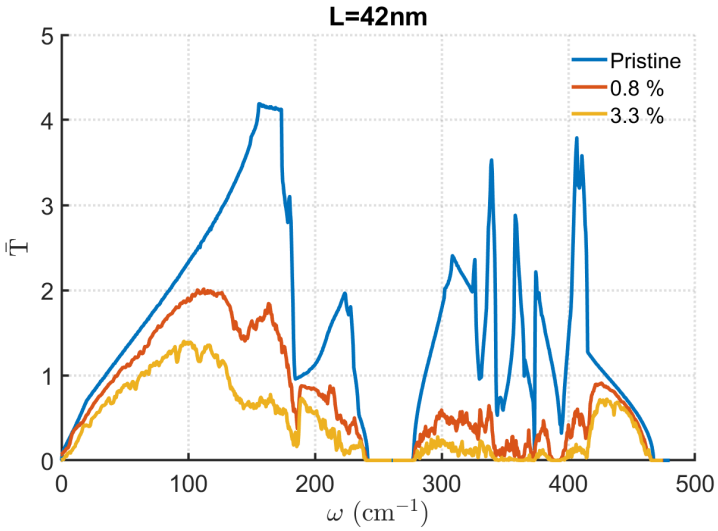

Figure 5.7: Phonon transmission as a function of the concentration of S vacancies. The length of the sample is $L_z = 42$ nm

There is a remarkable reduction of the transmission with respect to the pristine material, which affects both the acoustic and the optical modes. The decrease is even more relevant for the optical phonons with frequencies lower than 400 cm^{-1}, corresponding to the transverse and longitudinal optical modes $TO_{1,2}$ and $LO_{1,2}$ (see fig. 4.11). It was noticed that these

[3]Low concentrations were considered in this thesis because, at high concentrations, vacancies tend to form clusters to stabilize the systems [81]. This phenomenon is not included in our model.

modes are dominated by the sulphur contribution. Thus, their suppression upon introduction of S vacancies is in line with our prediction.

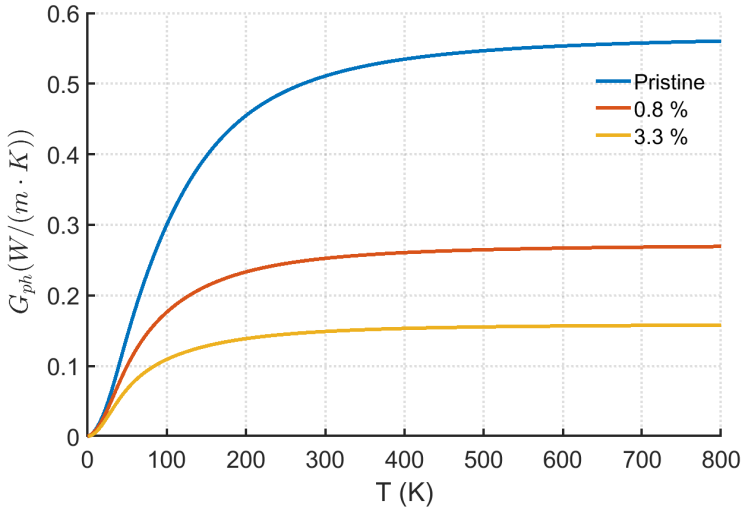

Figure 5.8: Phonon thermal conductance per unit width as a function of the temperature and for different concentrations of S vacancies. The length of the sample is $L_z = 42$ nm

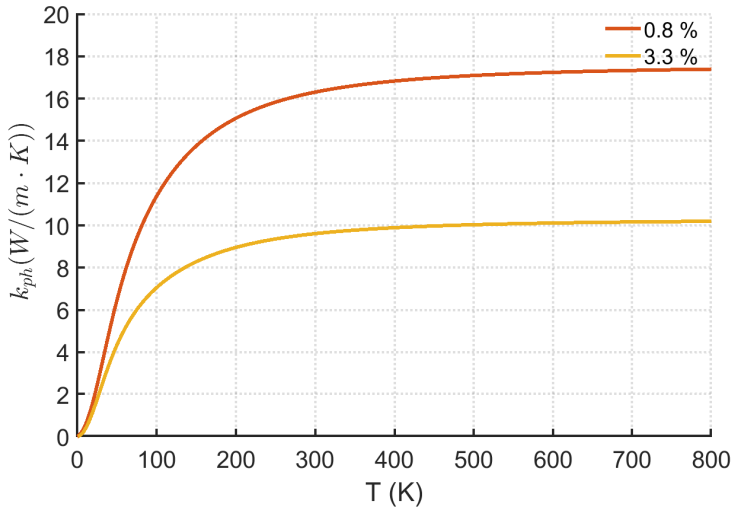

Figure 5.9: Phonon thermal conductivity as a function of the temperature and for different concentrations of S vacancies. The length of the sample is $L_z = 42$ nm

The plots of the conductance per unit width and of the conductivity confirm the observations made for the transmission.
The conductance in presence of 0.8% S vacancies is almost halved with respect to the pristine case, and it further reduces as the concentration increases.
The curves of the conductivities were obtained by multiplying G_{ph} with the length of the device ($L_z = 42$ nm) and by dividing by the thickness of

the single-layer, which was taken as the interlayer distance in bulk MoS_2 ($L_y = 0.65$ nm [59]).
Our calculation confirm that SL MoS_2 has undoubtedly an extremely low thermal conductivity. At room temperature, κ_{ph} is 16.3 $W\,m^{-1}\,K^{-1}$ for $x = 0.8\%$ and 9.6 $W\,m^{-1}\,K^{-1}$ for $x = 3.3\%$. These results are of the same order of magnitude of values previously found in literature for the pristine SL MoS_2. A thermal conductivity of 34.5 $(\pm 4)\,W\,m^{-1}\,K^{-1}$ was found from temperature-dependent Raman spectroscopy [93]. Through the use of *ab initio* calculation combined with Boltzmann Transport Equation, $\kappa_{ph} = 83\ W\,m^{-1}\,K^{-1}$ was estimated in [37] for a sample with a typical size of 1 μm and rough edges at room temperature.
In addition, with respect to these values, the inclusion of S vacancies reduces significantly the already low κ_{ph} of SL MoS_2. This consideration have already been highlighted in ref. [55, 94]. However, the effect of disorder have not been evaluated and no estimates of ZT have been reported.

In order to assess if the introduction of S vacancies has a positive impact on the thermoelectric efficiency, the electronic transport properties are needed as well. The electrical conductivity, the Seebeck coefficient and the electronic part of the thermal conductivity have been computed by Christophe Adessi. All these electric properties depend on the electron transmission $\bar{T}_{el}$ via eqs. 2.28. $\bar{T}_{el}$ is plotted in fig. 5.10 and it is possible to see that the introduction of S vacancies leads to a strong reduction of the electron transmission as well. Therefore, it is necessary to evaluate the thermoelectric figure of merit (ZT), which will be shown at the end of the chapter.

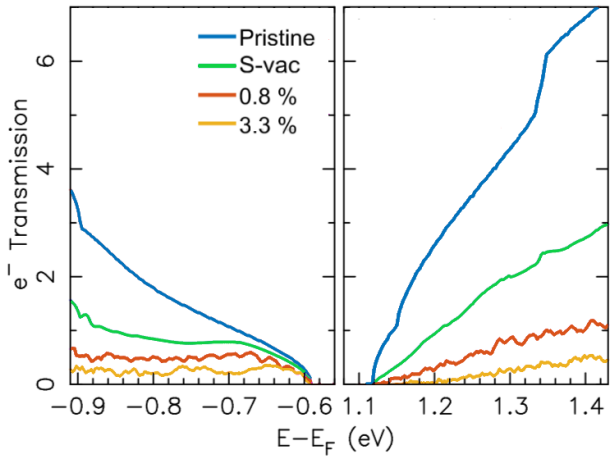

Figure 5.10: Electron transmission for different concentrations of S vacancies. The length of the sample is $L_z = 42$ nm

5.2.2 Variable Length at Fixed Concentration (x = 3.3%)

The second study concerns the effect on the thermal conductivity in devices with different lengths and the same concentration of sulphur vacancies,

which is constant to 3.3%.

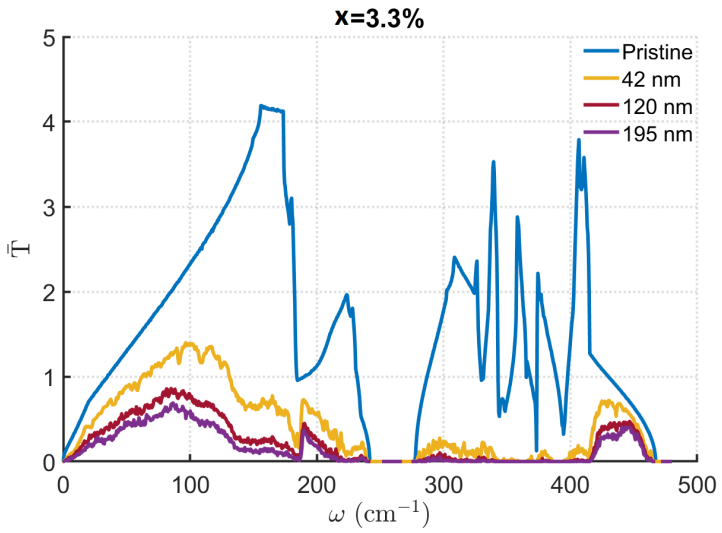

Figure 5.11: Phonon transmission as a function of the length of the sample. The concentration of S vacancies is 3.3%

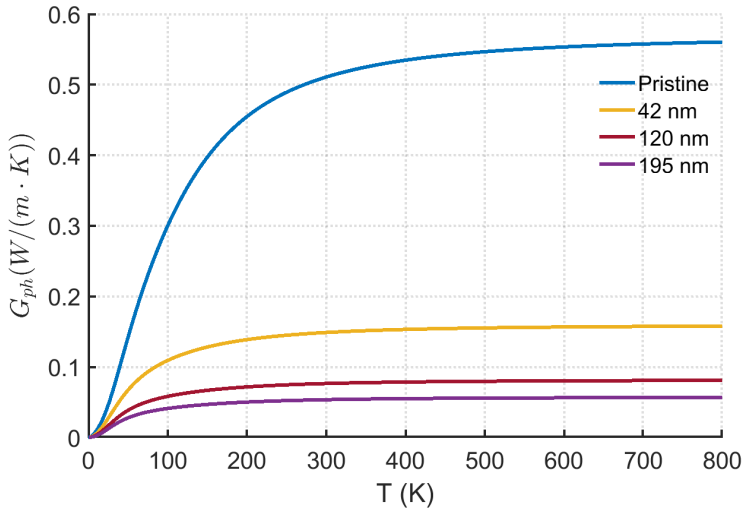

Figure 5.12: Phonon thermal conductance per unit width as a function of the temperature and for different lengths of the sample. The concentration of S vacancies is 3.3%

The transmission and the conductance per unit with of the pristine material are compared with those of devices including S vacancies and having lengths $L_z = 42$, 120, 195 nm. The same remarkable reduction of the phonon transport, which was observed in the previous case, is confirmed in this analysis. Furthermore, the LO and TO modes are suppressed almost completely when the length of the device is longer than 100 nm.

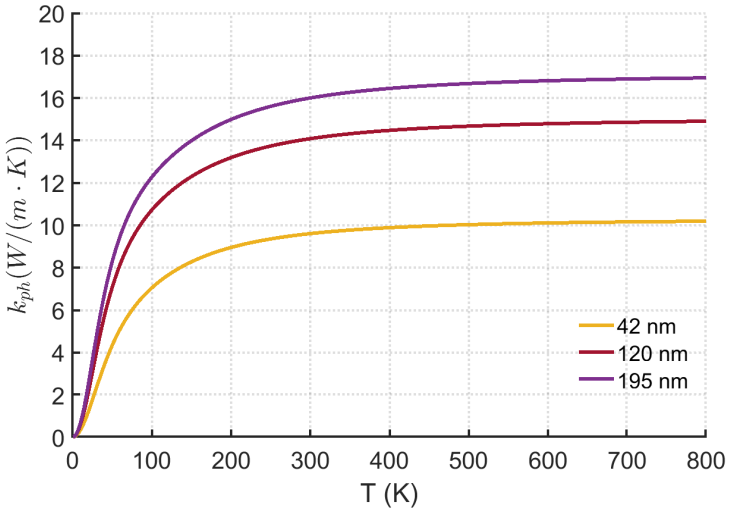

Figure 5.13: Phonon thermal conductivity as a function of the temperature and for different lengths of the sample. The concentration of S vacancies is 3.3%

The conductivity increases with the length of the device, passing from 9.6 $\mathrm{W\,m^{-1}\,K^{-1}}$ for $L_z = 42$ nm to 14.1 $\mathrm{W\,m^{-1}\,K^{-1}}$ for $L_z = 120$ nm and to 16.0 $\mathrm{W\,m^{-1}\,K^{-1}}$ for $L_z = 195$ nm.

The plot of the electron transmission shows that the transport of electrons is strongly reduced by the increase in the length of the device. This reduction is more significant at energy greater than the Fermi energy, corresponding to transport of electrons in the conduction band. As a matter of fact, the reduction of the electrical conductivity, due to sulphur vacancies, will be stronger for n-type materials (injection of electrons) than for p-type (injection of holes).

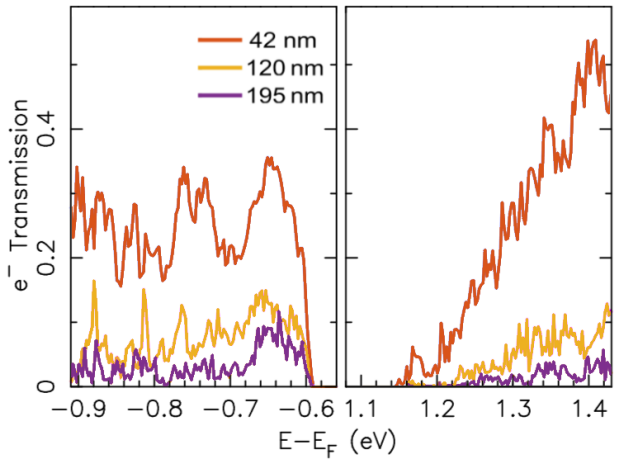

Figure 5.14: Electron transmission for different lengths of the sample. The concentration of S vacancies is 3.3%

5.2.3 The Thermoelectric Figure of Merit

At this point, the evaluation of the figure of merit (ZT) is necessary to understand the balance between positive and negative effects on the thermoelectric efficiency due to the presence of a disorder distribution of S vacancies.
ZT is a dimensionless quantity that expresses the ability of a given material to efficiently produce thermoelectric power and it reads as:

$$ZT = \frac{\sigma_{el}\ S^2}{\kappa_{el} + \kappa_{ph}}\ T \tag{5.1}$$

The denominator is dominated by κ_{ph}, since the electrical contribution to the total thermal conductivity is approximately two times lower than the phonon contribution.
The figure of merit has been computed as a function of the concentration of sulphur vacancies, of the length of the device and of the temperature. In the following figures, the trend of ZT is shown in the two cases of n-type (blue) and p-type (red) materials. In fact, while the lattice thermal conductivity is independent on the nature of the charge carriers, all the electrical properties must be evaluated depending on whether the charges are electrons or holes. The solid and dashed lines in the figures are related to ZT values at T=300 K and T=700 K respectively.

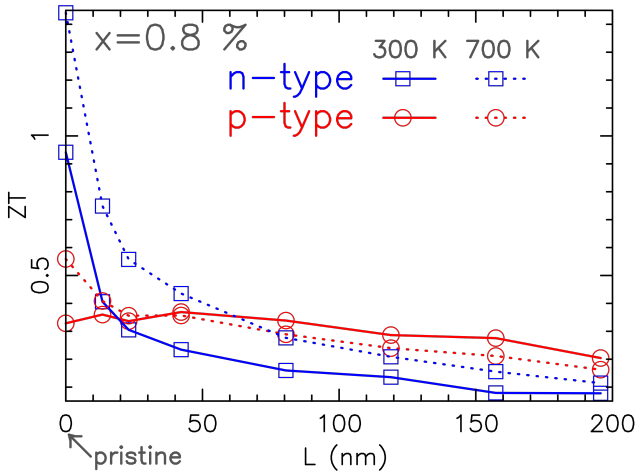

Figure 5.15: Thermoelectric figure of merit of SL MoS_2 in presence of a disordered distribution of sulphur vacancies with concentration of 0.8%

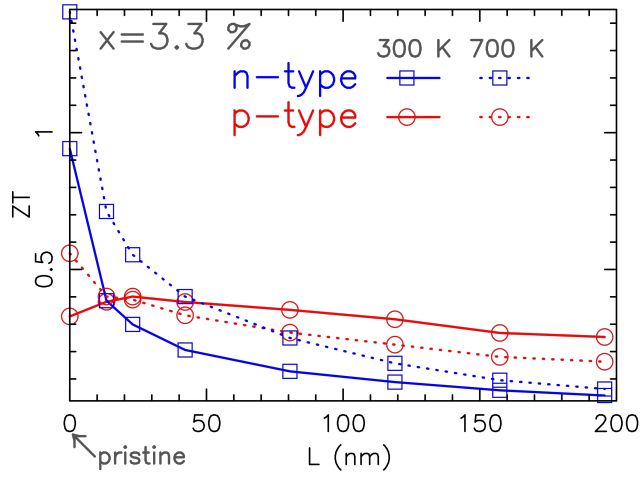

Figure 5.16: Thermoelectric figure of merit of SL MoS_2 in presence of a disordered distribution of sulphur vacancies with concentration of 3.3%

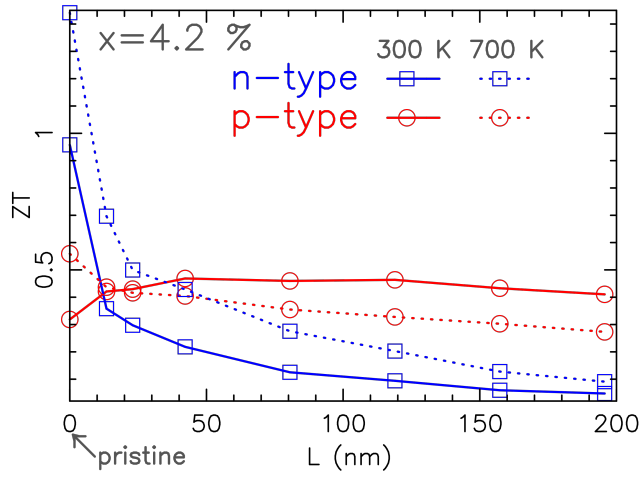

Figure 5.17: Thermoelectric figure of merit of SL MoS_2 in presence of a disordered distribution of sulphur vacancies with concentration of 4.2%

It is clear from these plots that for n-type materials, the figure of merit is worsened by the presence of S vacancies, independently on the defects' concentration and on the temperature. The cause is the low power factor (σ_{el}), which is reduced more than the lattice thermal conductance.
A different behaviour is observed in p-type materials. A slight improvement of the figure of merit is found at T=300 K, which grows with increasing vacancies' concentration and with decreasing length of the device.
At T=700 K, the reduction of the power factor by the presence of S vacancies prevails on the decrease of the lattice thermal conductivity, resulting in a lower ZT.

Let us summarize the main conclusions deriving from the case study examined in this chapter:

- The inclusion of a disordered distribution of S vacancies reduces significantly the already low κ_{ph} of SL MoS_2. However this does not correspond automatically to an improve of the thermoelectric figure of merit.

- For a realistic material (with disordered distributions of defects) the ZT for p-type and n-type materials are drastically different. Overall, the disordered distribution of S vacancies has a small positive impact on ZT only for p-type SL MoS_2 and at low temperatures. In fact, in the best case ($x = 4.2\%$, $T = 300$ K, p-type), ZT is passing from ≈ 0.3 for the pristine material to ≈ 0.5 for the monolayer with S vacancies.
  Instead, the ZT of n-type materials is always worsened by the inclusion of S vacancies.

- In the optics of realizing a device, the total thermoelectric conversion efficiency depends on the combination of both the figure of merits of the n-type and p-type materials which form the legs of the thermoelectric couples (fig. **??**). The inclusion of sulphur vacancies could be viable to improve the ZT of the p-type leg, while a vacancy-free material is preferable for the n-type leg.
  Many other factors contribute to the overall efficiency. For example, our analysis did not consider the reduction of the thermal conductivity caused by phonon-phonon Umklapp scattering. Hence, the estimates of ZT obtained in this chapter are suitable to take into account the impact of the particular kind of defect included in the system. They are not intended to predict the precise efficiency of realistic thermoelectric devices.

- The technique employed to deal with disordered distribution of defects is suitable for a series of future studies. Different strategies may be tested to engineer materials in order to achieve a good "phonon-glass electron-crystal" behaviour. For example, the effect of a combination of different kinds of defects could be evaluated at the same time. Moreover, the concentration of defects could be tuned locally with the aim of producing graded distributions of defects.

Chapter 6

Effect of Inelastic Scattering on the Lattice Thermal Conductance of Graphene: Towards Diffusive Regime

The phonon transport in ballistic regime was studied in Ch. 4 by pure *ab initio* calculations within the Landauer Formalism. The reduction of the conductance due to the presence of a disordered distribution of defects was taken into account as well by using the Green's functions technique (Ch. 5). This chapter presents the effect on the lattice thermal conductivity of phonon-phonon Umklapp scattering and boundary scattering. The former scattering mechanism is a consequence of anharmonic terms in the expansion of the interatomic potential, while the latter accounts for specular scattering due to the roughness of boundaries in real samples. The materials studied are pristine graphene and MoS_2.
A detailed description of inelastic scattering processes was examined in Ch. 3, together with the theoretical framework necessary. It is useful to recall the main points in order to describe the process leading to the results.

The phonon thermal conductance per unit width is found within the Landauer Formalism as:

$$G_{ph}(T) = \frac{\hbar^2}{8\pi k_B T^2} \sum_{\lambda} \int_0^{\infty} \bar{T}_{\lambda}(\omega, T)/L_x \, \frac{\omega^2}{\sinh^2(\frac{\hbar\omega}{2K_B T})} d\omega \tag{6.1}$$

The key quantity to compute G_{ph} is the transmission function $\bar{T}$, whose expression reads:

$$\bar{T}_{\lambda}(\omega, T) = M_{\lambda}(\omega) \; \mathcal{T}_{L_z}(\Lambda_{\lambda}(\omega, T)) \tag{6.2}$$

where $M_{\lambda}(\omega)$ is the density of modes (DOM), which coincides with the phonon transmission computed for the pristine materials (Ch. 4.1.3).
$\mathcal{T}_{L_z}(\omega, T)$ is the transmission coefficient, which accounts for the scattering phenomena and acts like a function modulating the DOM. It depends on

the mean free path value of each phonon $\Lambda_\lambda(\omega, T)$ and on the length of the system L_z through:

$$\mathcal{T}_{L_z}(\omega, T) = \frac{\Lambda_\lambda(\omega, T)}{L_z + \Lambda_\lambda(\omega, T)} \tag{6.3}$$

Since the Umklapp-scattering mean free path is inversely proportional to the temperature, the transmission coefficient will depend on the temperature as well.

To evaluate the transmission function $\bar{T}$, a mixed approach is employed: the full DOM is computed from first principles within the Landauer Formalism; instead the transmission coefficient is computed from the knowledge of the phonon life time, which is a feature typical of methods based on Peierls-Boltzmann Transport Equations in relaxation time approximation. Analytical expressions, based on parameters computed with DFT calculations, are used to evaluate the phonon life times due to Umklapp and boundary scattering.
This approach allows to evaluate the phonon transport properties in the intermediate ballistic-diffusive regime characteristic of mesoscopic systems.

6.0.1 Computation of the Phonon Life Time and Mean Free Path for the Umklapp Scattering Process

Assuming different scattering mechanisms as independent, the effects of Umklapp phonon-phonon scattering (τ_λ^U) and phonon-boundary scattering (τ_λ^B) are combined in the the Matthiessens's rule. The reciprocal of the total phonon life time (phonon scattering rate) is thus given as:

$$1/\tau_\lambda(\omega) = 1/\tau_\lambda^U(\omega) + 1/\tau_\lambda^B \tag{6.4}$$

The Umklapp phonon-phonon scattering rate can be written as:

$$1/\tau_\lambda^U(\omega, T) = \frac{\gamma_\lambda^2(\omega) k_B T \omega^2}{M v_\lambda^2(\omega) \omega_\lambda^{max}} \tag{6.5}$$

where $\gamma_\lambda(\omega)$ is the mode Grüneisen parameter, which characterizes the strength of the Umklapp phonon-phonon scattering process for the mode λ. $v_\lambda(\omega)$ is the modulus of the group velocity vector computed from the phonon dispersion relation at frequency ω for the mode λ. M is the mass of the unit cell and ω_λ^{max} is defined as the highest frequency of the mode λ.
The rate of phonon-boundary scattering reads:

$$1/\tau_\lambda^B(\omega) = \frac{v_\lambda(\omega)}{D} \frac{1-p}{1+p} \tag{6.6}$$

where D coincides with the sample size in the transport direction L_z and p is the specularity parameter, which is defined as the probability of specular scattering at the boundary. The specularity parameter ranges from

0 for completely rough boundary to 1 for perfectly smooth boundary. In the case that $p = 1$, the scattering process at the boundary is completely elastic. Lower values of p correspond to an increasing impact of the inelastic phonon-boundary scattering mechanisms. The lower the specularity parameter, the higher the probability of phonon diffusion.

Once the total life time is known, the phonon mean free path can be computed as:

$$\Lambda_\lambda(\omega, T) = v_\lambda(\omega)\ \tau_\lambda(\omega, T) \tag{6.7}$$

In case of perfectly smooth boundary, the total phonon life time coincides with τ_λ^U. Thus the mean free path results to be:

$$\Lambda_\lambda(\omega, T) = v_\lambda(\omega)\ \tau_\lambda^U(\omega, T) = \frac{M v_\lambda^3(\omega)\omega_\lambda^{max}}{\gamma_\lambda^2(\omega) k_B T \omega^2} \tag{6.8}$$

Grüneisen Parameter

The Grüneisen parameter and the group velocity were computed using *PHONOPY*, as explained in Ch. 3.2.1.
The mode Grüneisen parameter as function of the frequency[1] is depicted in the following graphs.

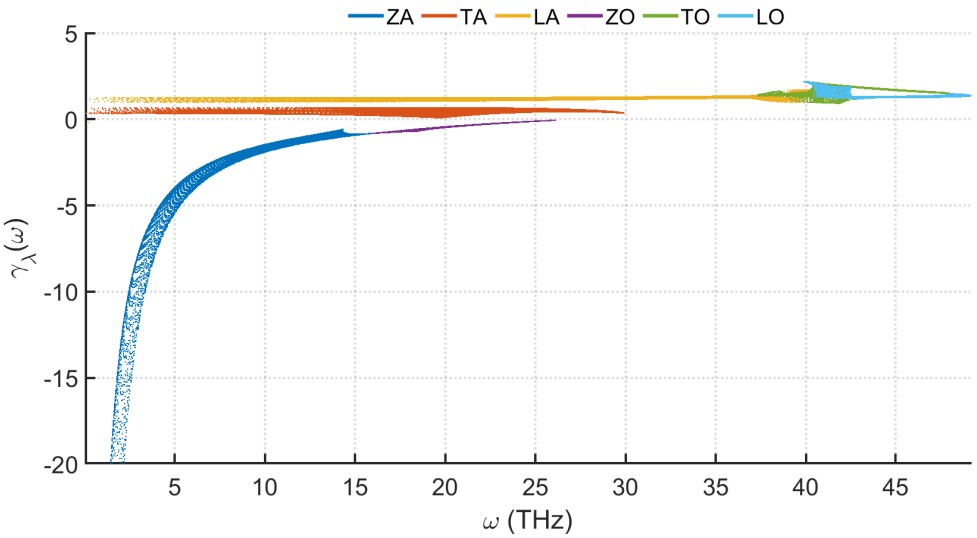

Figure 6.1: Grüneisen parameter of pristine graphene as a function of the frequency. The different colours correspond to each mode. For the ZA mode, the Grüneisen parameter diverges to $-\infty$ for $\omega \to 0$.

[1]To be precise, all the quantities are calculated as function of $\omega((q))$, keeping track of the dependence on wave-vectors in the whole first BZ (see Ch. 3.4). Therefore, phonons with identical ω and different $\mathbf{q}$ do not have the same γ, v, τ and Λ, explaining the multiplicity of values for each frequency ω in the plots.

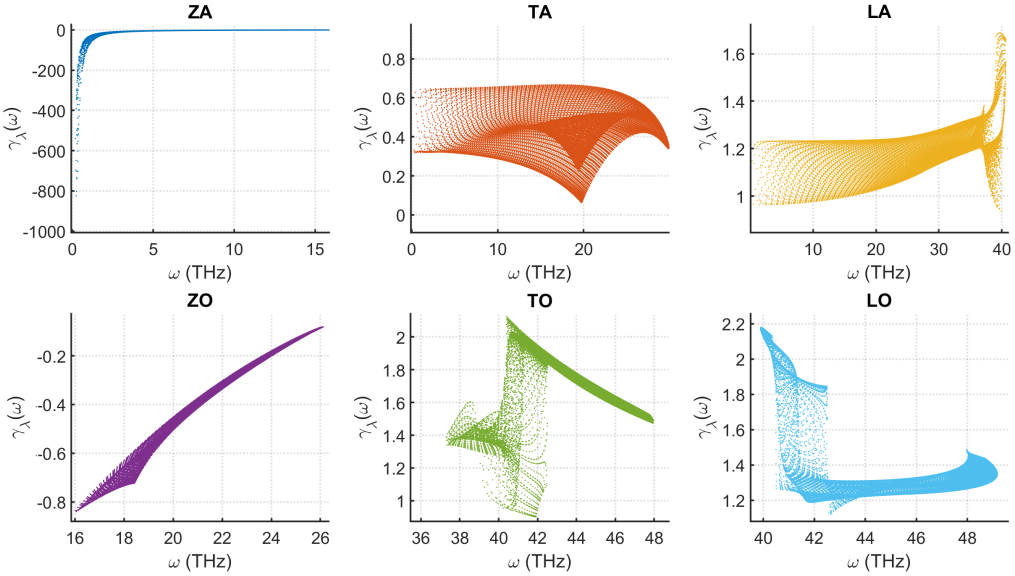

Figure 6.2: Mode Grüneisen parameter of pristine graphene as a function of the frequency. Each mode is plotted in a separate window.

The mode Grüneisen parameter is associated to the degree of anharmonicity of the interatomic force constants. The higher the Grüneisen parameter, the stronger the impact of phonon-phonon Umklapp scattering. It is directly proportional to the coefficient of thermal expansion (eq. 3.11).
The Grüneisen parameter is generally positive, in agreement with the usual positive sign of the coefficient of thermal expansion [43]. In fact, it is well known that, if the temperature increases, usually materials dilate.
However, graphene and its derivatives are notorious for their large negative thermal expansion over a wide range of temperature, ascribed to the negative Grüneisen parameter of the ZA out-of-plane mode [41].
The data plotted in 6.1 and 6.2 confirms that ZA and ZO modes present negative Grüneisen parameters. Moreover, for the ZA mode, the Grüneisen parameter diverges to $-\infty$ close to the Γ point.
Average values of the mode Grüneisen parameter, obtained from the graphs above, are reported in tab. 6.1.

	ZA	TA	LA	ZO	TO	LO
$\bar{\gamma}_\lambda$	-2.1365	0.5761	1.2470	-0.4178	1.7849	1.3512
$\sigma(\gamma_\lambda)$	1.3296	0.1619	0.0721	0.2198	0.1576	0.0471

Table 6.1: Average mode Grüneisen parameter and standard deviation.

Phonon Group Velocity

The group velocity was computed from the full phonon dispersion in the first BZ and plotted in fig. 6.3.

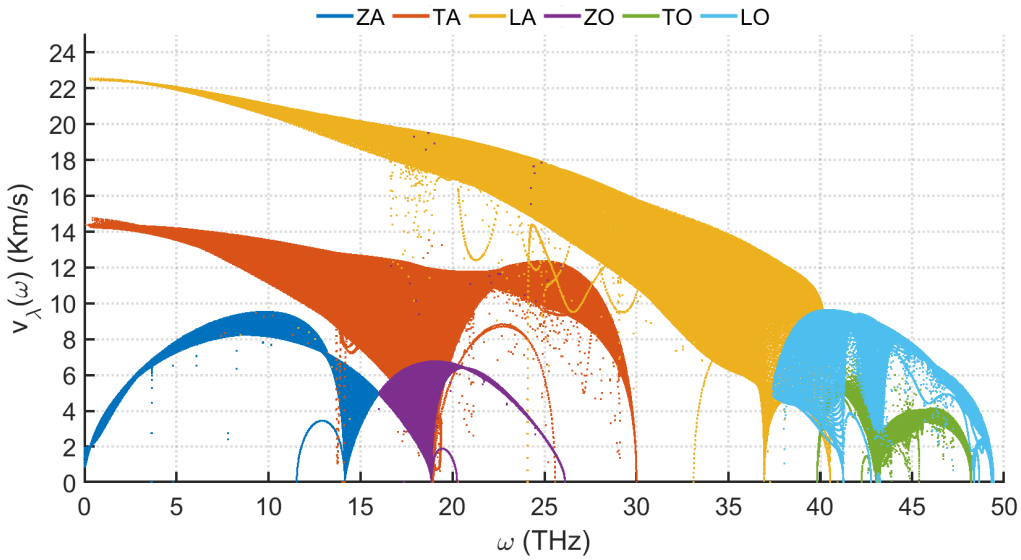

Figure 6.3: Group velocity of pristine graphene as a function of the frequency.

At low frequencies, the TA and LA modes have an almost constant and high group velocity of about 22 Km/s and 14 Km/s respectively, in good agreement with previous experimental results [52] and theoretical calculations [63, 104].
The ZA mode[2] and the optical modes have lower group velocities on average than the in-plane acoustic modes.

[2]The group velocity of ZA phonons v_{ZA} is supposed to tend to zero near the Γ point, while finite values are observed in fig. 6.3. The reason lies in a numerical instability [77] that commonly affects the phonon dispersion of the ZA mode in 2D materials, solely near the Γ point. This instability could have been removed by performing a calculation with more restrictive tolerance parameters, as done in Ch. 4. However, the group velocity is needed only to derive the phonon life times; wrong values of the group velocity, close to the Γ point, do not introduce relevant errors in the life times. In fact, taking v_{ZA} correctly equal to zero, the life time is expected to be zero as well. Taking the finite v_{ZA} from the calculation, wrong at low frequencies, it is found that τ^U_{ZA} tends to zero as well (fig. 6.4). This is due to the divergence at low frequencies of the Grüneisen parameter (see eq. 6.5).

Phonon Life Time and Mean Free Path for Umklapp Scattering

Knowing the Grüneisen parameter and the group velocity, it is straightforward to compute the phonon life times and the phonon mean free paths associated to the Umklapp process. The life time values per mode at room temperature are plotted in fig. 6.4.

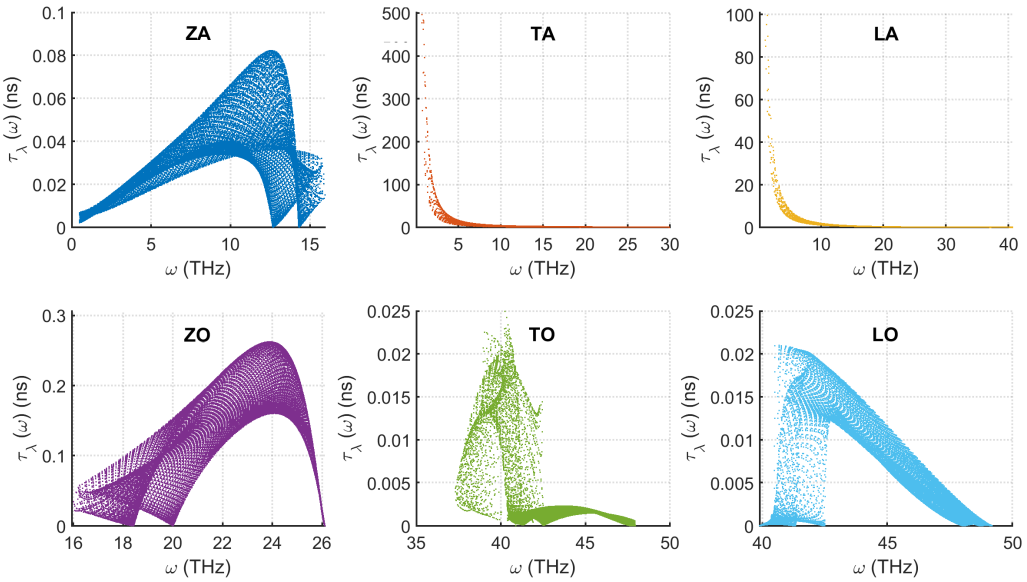

Figure 6.4: Phonon life time associated to the Umklapp process, computed at room temperature (300K).

It is clear from these graphs that TA and LA modes display by far the longest Umklapp life times, which are in the order of nanoseconds at room temperature.
Life times of in-plane acoustic and optical phonons (ZA and ZO) are in the order of hundreds of picoseconds, while for in-plane optical phonons (TO and LO), they are much shorter, in the order of a few picoseconds.
τ_λ^U and Λ_λ^U are inversely proportional to the temperature (eq. 6.5), hence to obtain data at a different temperature one just needs to scale the values at room temperature by a factor $\frac{300\,K}{T}$.

Multiplying the life times for the modulus of the group velocity and averaging over the values of phonons of the same mode, one obtains the average mean free path per mode. These values are listed in tab. 6.2, together with their standard deviation.

	ZA	TA	LA	ZO	TO	LO
$\bar{\Lambda}$ (μm)	0.2436	4.4341	0.6426	0.5975	0.0058	0.0113
$\sigma(\Lambda)$ (μm)	0.1791	3.2897	0.5960	0.4122	0.0040	0.0165

Table 6.2: Average mean free path and standard deviation per mode at T=300K

An intriguing question in the theory of phonon transport in graphene is the relative contribution to heat conduction by LA, TA and ZA phonon polarization branches [48].
Indeed in literature there are many publications contradicting each other. In ref. [66] it is shown that the relative contribution from ZA branch to heat conduction is relevant and increases with decreasing the size, specularity parameter, and temperature of graphene ribbons.
Diversely, in ref. [19, 46] the contribution of optical and ZA phonons to thermal transport has been neglected "because of their low group velocity and large Grüneisen parameter"[48], which imply in turn short life time and mean free path.
In my opinion, this last assumption is mistaken when dealing with mesoscopic systems. In fact, the difference in the life times magnitude among different modes does not represent by itself the criterion to determine which modes contribute to the thermal conductance. It is the transmission coefficient that matters. As a consequence, one has to compare the values of phonon mean free paths, at a given temperature, with the size of the system L_z. In fact, one could follow this argument: imagine that the mean free path is 1 mm for the generic mode-A, while it is 1 μm for the mode-B. If the device was long several microns, it would be correct to state that the contribution of mode-B phonons to the thermal transport is negligible with respect to the one of mode-A phonons. Indeed there is a 10^3 difference in their mean free paths. But if L_z was about 100 nm, then also the mode-B phonons would be transmitted with high probability; in this case the contribution of mode-A and mode-B to the thermal conductance would be similar.
For this reason, the phonon mean free paths require to be analysed as a function of the temperature and then compared with the length of the system.

Fig. 6.5 shows the phonon mean free paths at three different temperatures: 100 K, 300 K and 900 K. Let us consider for example a device of length $L_z = 1$ μm (dashed lines in figures 6.5). It is evident that at T = 100 K all the modes have many phonons with Λ^U comparable to L_z, which can contribute to the thermal conductance. Moving to T = 300 K, TO and LO phonons display mean free paths significantly lower than 1 μm, meaning that their contribution is inactive at room temperature. ZA and ZO have mean free paths shorter than L_z, but still in the same order of magnitude. Thus, their contribution is supposed to be smaller than LA and TA's, but it is not negligible.
Finally, at high temperature (900 K) only the in-plane acoustic modes dominate the thermal transport.

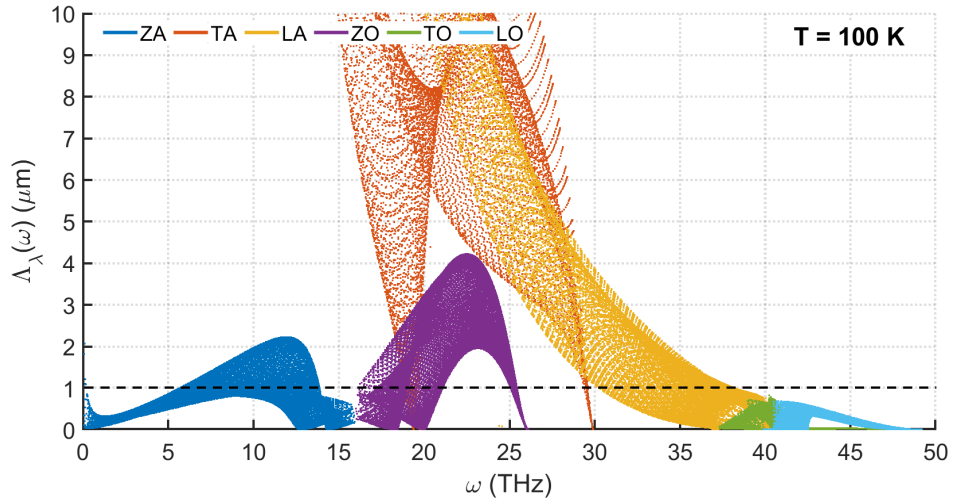

(a)

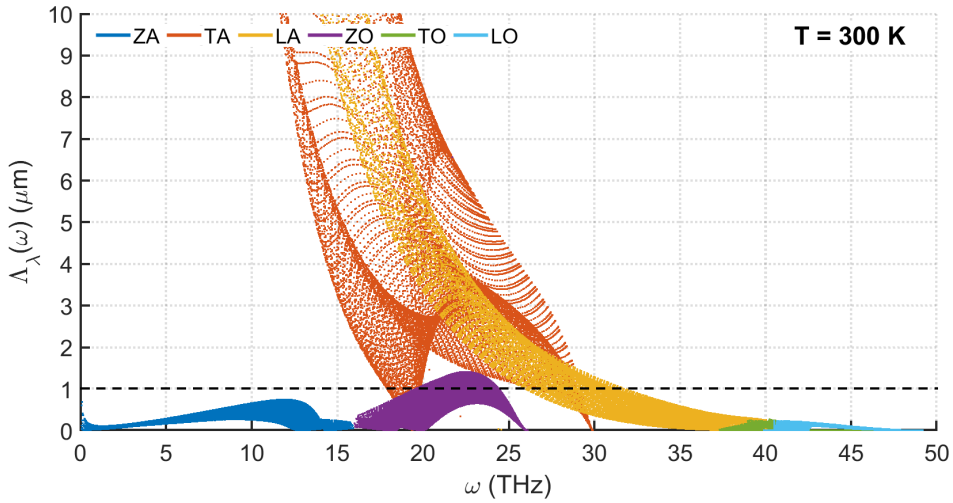

(b)

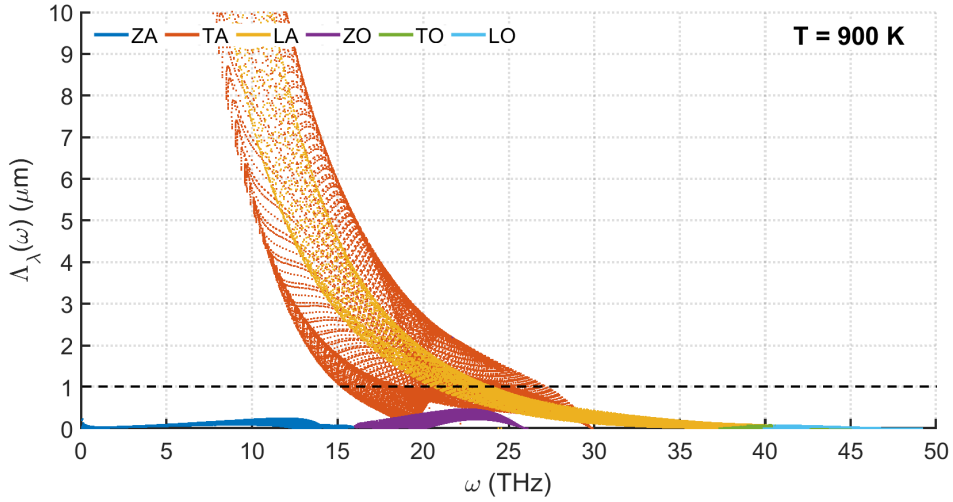

(c)

Figure 6.5: Phonon mean free path (Umklapp scattering) for T=100K (a), T=300K(b) and T=900K (c) in the range $0-10$ μm (Λ^U of LA and TA phonons extend in a range that is several order of magnitude higher).

6.0.2 Coefficient of Transmission

At this point, everything is ready to evaluate the transmission coefficient in a quantitative way and thereafter proceed to the calculation of the lattice thermal conductance.
A graphical representation of $\mathcal{T}_{L_z}(\Lambda_\lambda(\omega, T))$ is given in fig. 6.6 for a sample of length $L_z = 1$ μm at T=300 K; the only Umklapp phonon-phonon scattering contribution is included (p=1).

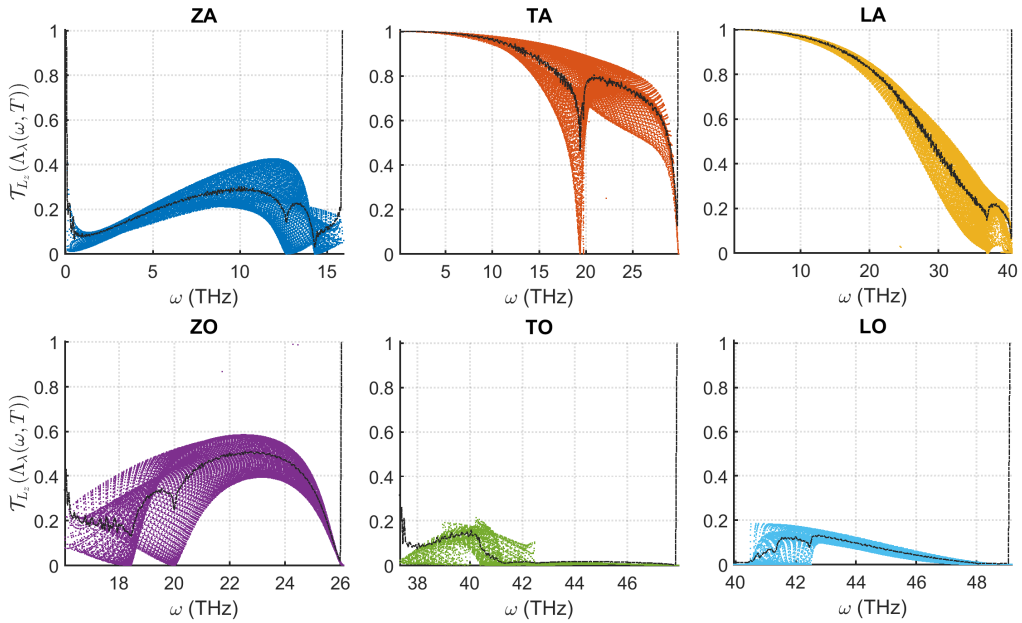

Figure 6.6: Transmission coefficient for a graphene sample of length $L_z = 1$ μm at T=300K. The boundaries are considered as perfectly smooth (p=1), therefore, only the Umklapp contribution to the phonon life time is included. Every mode is plotted in a different quadrant. The coloured dots are the values corresponding to all the q points sampled in the first Brillouin zone, while the black line represents an average over all the phonons with same ω and different $\mathbf{q}$ and λ.

In the following graphs, one can see the transmission coefficient varies with the temperature with $L_z = 1$ μm (fig. 6.7), and how it depends on the sample size at T=300 K (6.8).
In addition, the effect of boundary scattering is included in fig. 6.9, obtaining mean free paths which comprehend both Umklapp and boundary scattering. In this context, the specularity parameter is varied as an arbitrary parameter, aiming to provide an idea of its impact on the transmission. It is not computed on the base of the particular roughness of the samples' boundary.
A black line is drawn to give a qualitative, but immediate idea of the impact of $\mathcal{T}$ on the transmission function. It represents an average over all the phonons with same ω and different $\mathbf{q}$ and λ.

Temperature Dependence

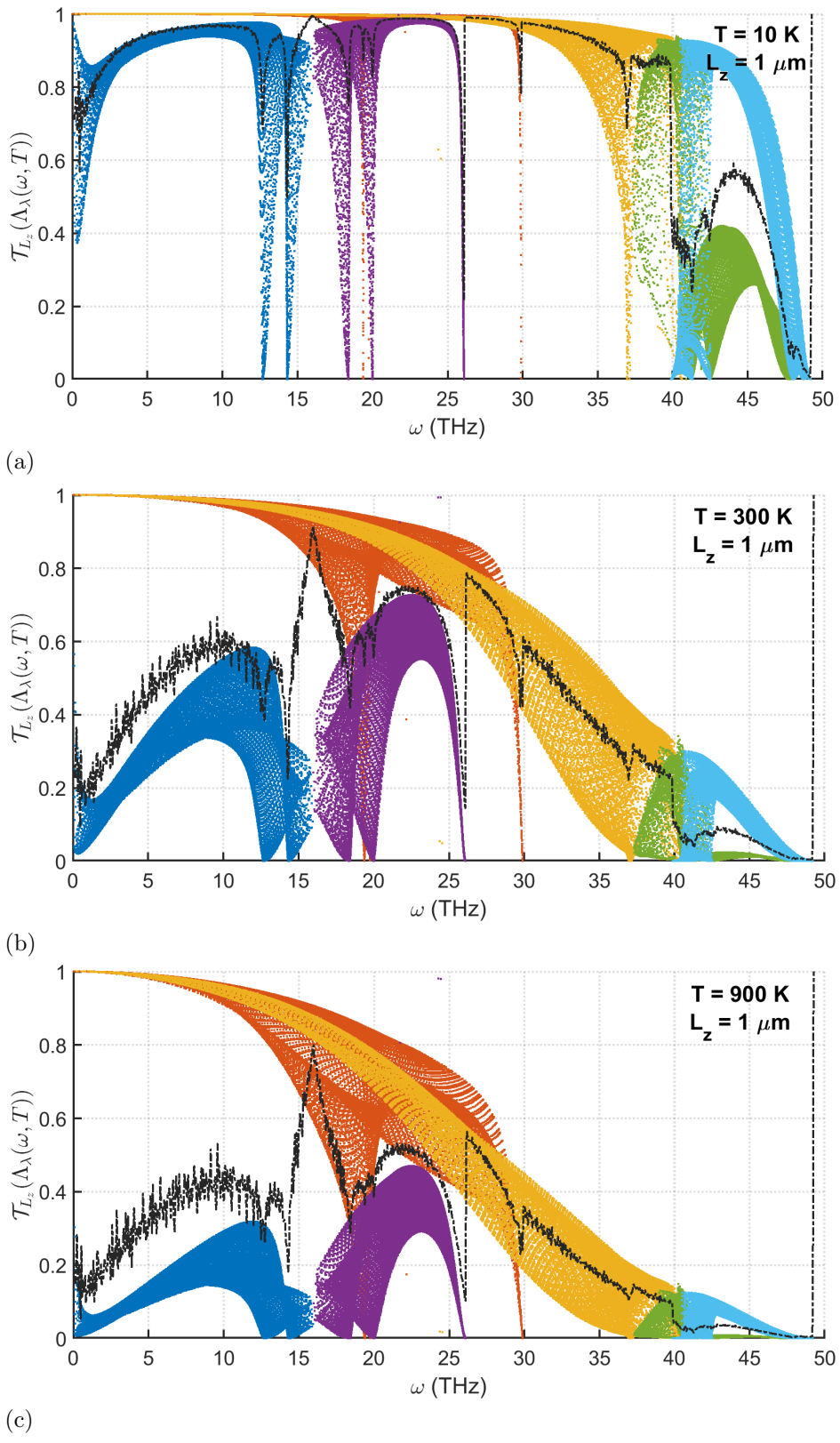

Figure 6.7: Transmission coefficient for a sample of length $L_z = 1\mu\mathrm{m}$ at T=10K (a), T=300K (b) and T=900K (c).

Size Dependence

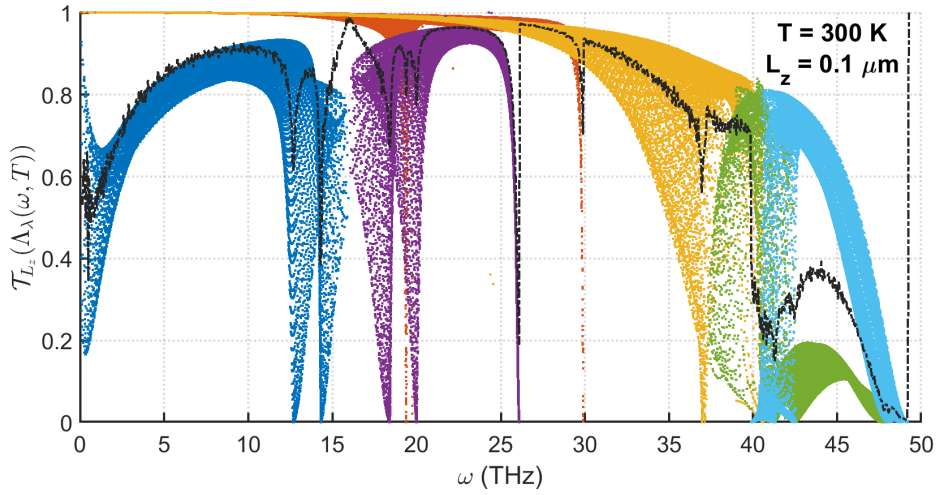

(a)

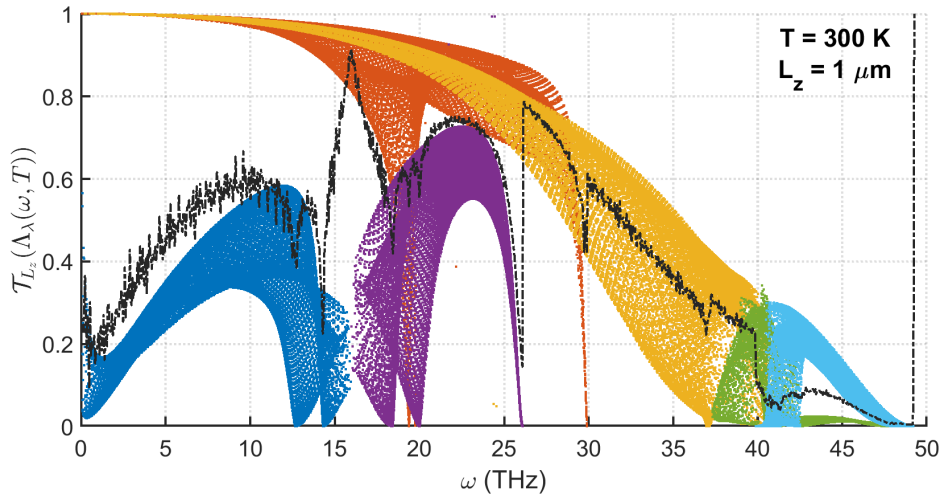

(b)

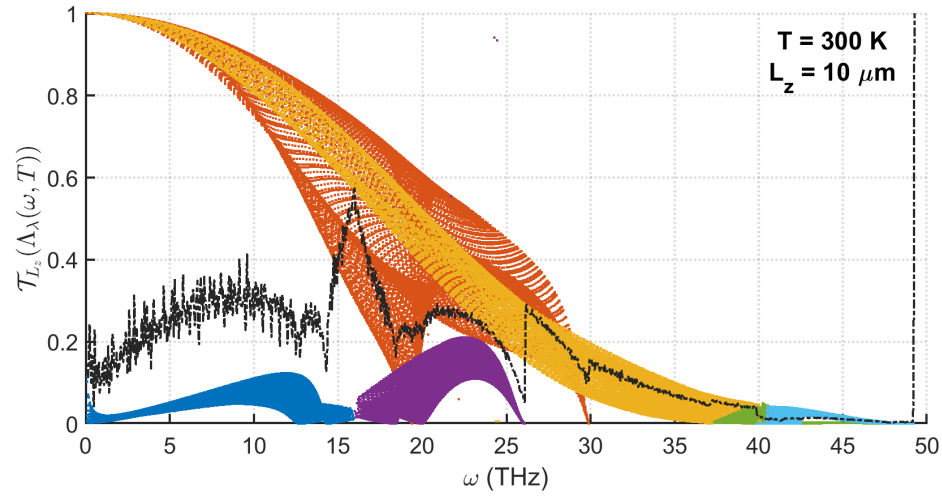

(c)

Figure 6.8: Transmission coefficient at T=300K, for samples with Lz=100 nm (a), Lz=1 micron (b) and Lz=10 micron (c).

Impact of Boundary Scattering

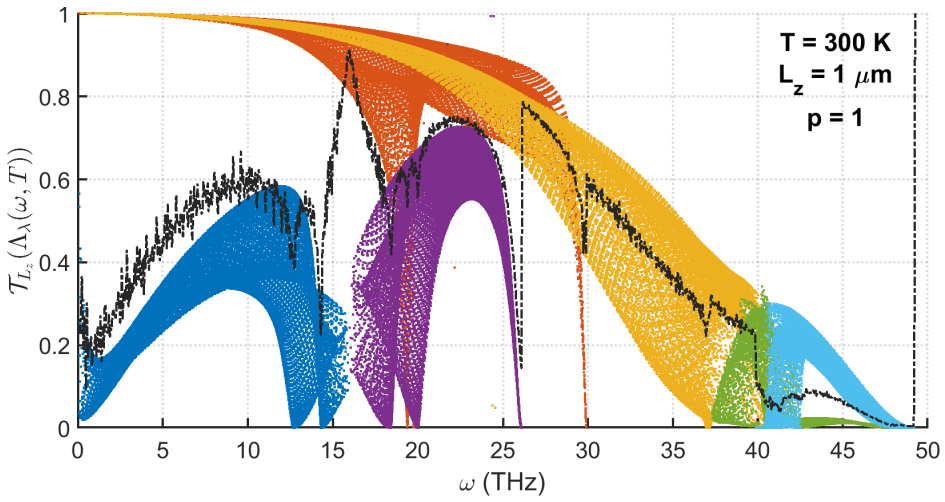

(a)

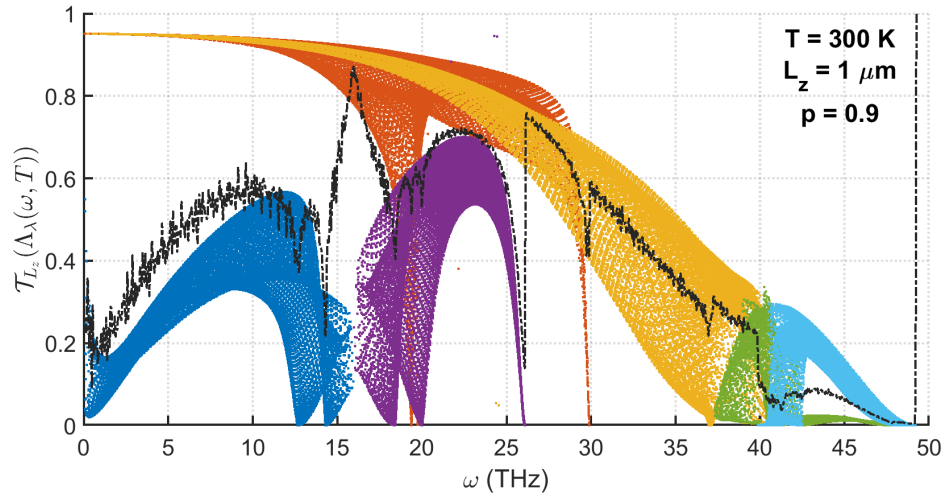

(b)

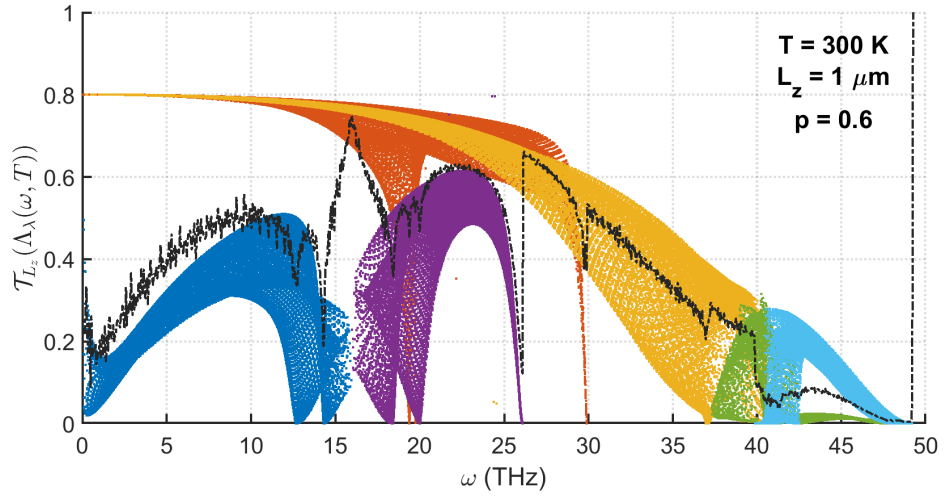

(c)

Figure 6.9: Transmission coefficient for a samples of length Lz=1 micron at T=300K, with p=1 (a), p=0.9 (b) and p=0.6 (c).

6.0.3 Lattice Thermal Conductance

From the knowledge of the transmission coefficient and of the DOM presented in Ch. 4.1.3, the lattice thermal conductance per unit width G_{ph} is computed according to eq. 6.1. The trend of G_{ph} as a function of the temperature is shown for different sample sizes L_z and a specularity parameter $p = 0.9$.[3]

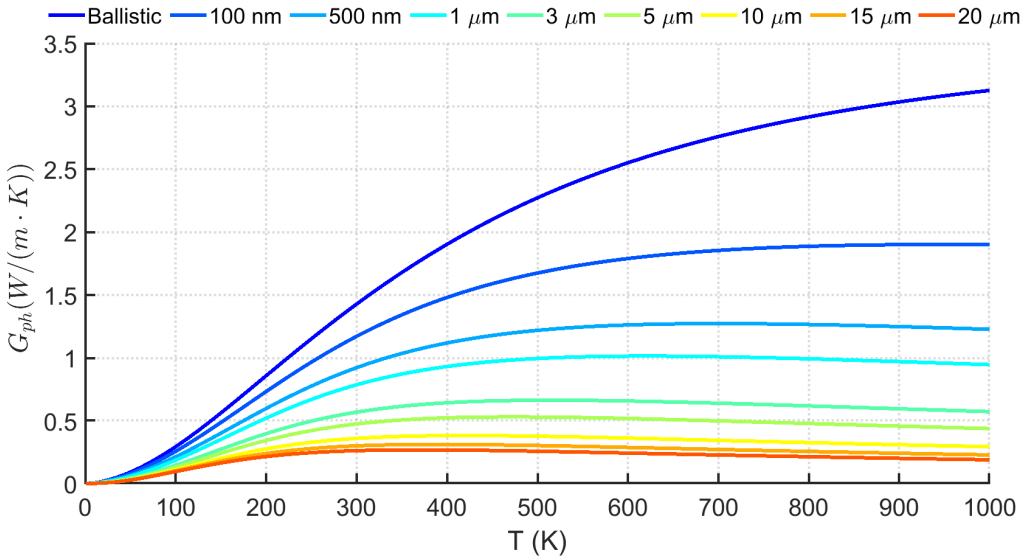

Figure 6.10: Conductance in diffusive regime for graphene to the change of L_z, considering Umklapp phonon-phonon scattering and boundary scattering (p=0.9).

While more and more phonons are populated as the temperature increases, the conductance grows, but there is also a detrimental contribution brought by Umklapp scattering which is more effective at high temperatures. Thus, including inelastic scattering, the conductance reaches its maximum at lower temperature with respect to the ballistic case and then slowly decreases.

A Technical Note on the Calculation

The physical quantities necessary to compute the phonon mean free path, i.e the Grüneisen parameters and the group velocities, were calculated on the base of a unit cell that coincides with the primitive cell of graphene (2 basis atoms). The values of these quantities as a function of the q points of the supercell, which was employed to compute the transmission, were found by interpolation with a code that I wrote with *Matlab*.
To validate this procedure, the conductance has also been computed directly with mean free path values coming from the supercell (8 atom basis). The difference between the two curves is minimal at low temperatures, while a

[3]This value of the specularity parameter was chosen in agreement with ref. [47]. It is an approximated value introduced to consider diffusive scattering from a quasi-smooth boundary. The dependence of p on ω is neglected as well.

maximum error of $\sim 10\%$ occurs at high temperatures (> 500 K). The use of the interpolation method allows to reduce the computation time of at least 1 order of magnitude. An error of about 10% could than be acceptable in the optic of extending this procedure to much more time demanding calculations for systems with defects.

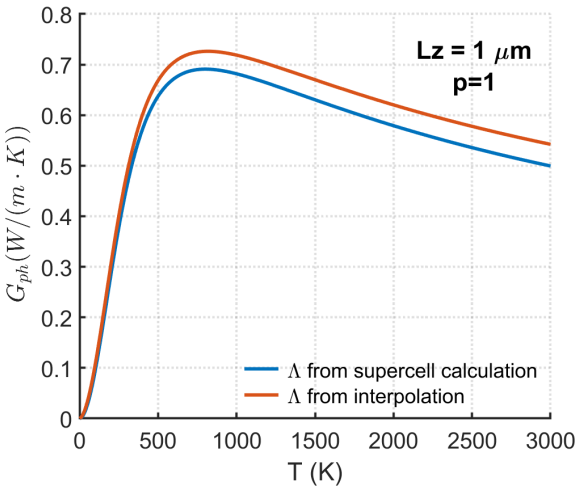

Figure 6.11: Validation of the mean free path interpolation method from the primitive cell calculation. Comparison with the conductance obtained from the data related to the supercell calculation.

6.0.4 Lattice Thermal Conductivity

In order to pass from the conductance per unit width to the conductivity one needs to define the thickness L_y of the studied layer. In this case, L_y is considered equal to 0.345 nm, which is the distance of two graphene layers in bulk graphite. Thus:

$$\kappa_{L_z}(T) = \frac{L_z}{L_y} G_{ph}(T) \tag{6.9}$$

where L_z is the length of the sample which is introduced as a parameter in order to account for the Umklapp and boundary scattering. G_{ph} is the conductance divided by L_x, which is the width of the unit cell used for the DFT calculation.

The conductivity is plotted in fig. 6.12 as a function of the temperature and for different lengths of the sample, with L_z ranging from 100 nm up to 20 μm. Moreover, the effect of the boundary scattering is evaluated in a qualitative way in fig. 6.13, where the specularity parameter p takes three different values ($p = 1, 0.9, 0.6$).

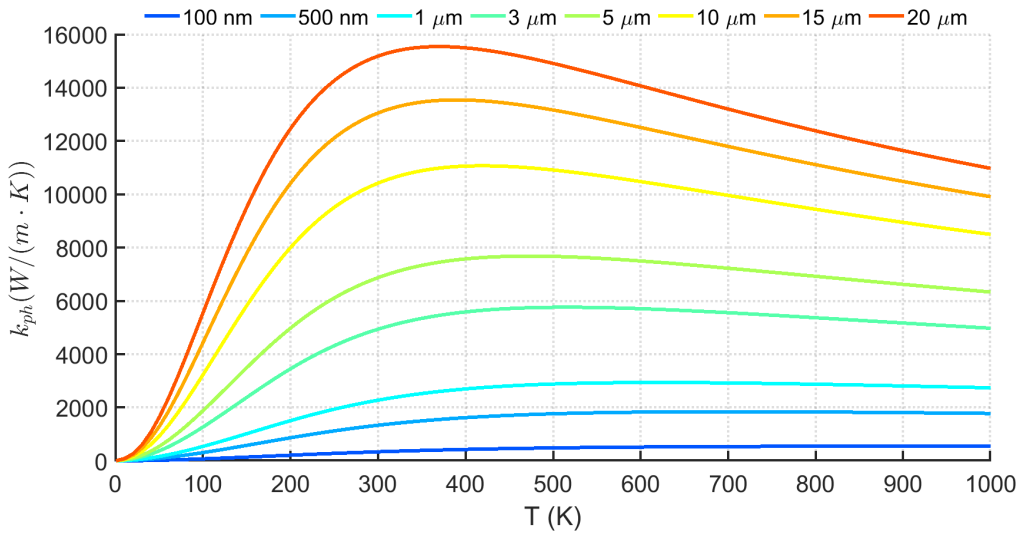

Figure 6.12: Conductivity in diffusive regime for graphene to the change of L_z, considering Umklapp phonon-phonon scattering and boundary scattering (p=0.9). The thickness of the graphene layer has been taken as $L_y = 0.345nm$

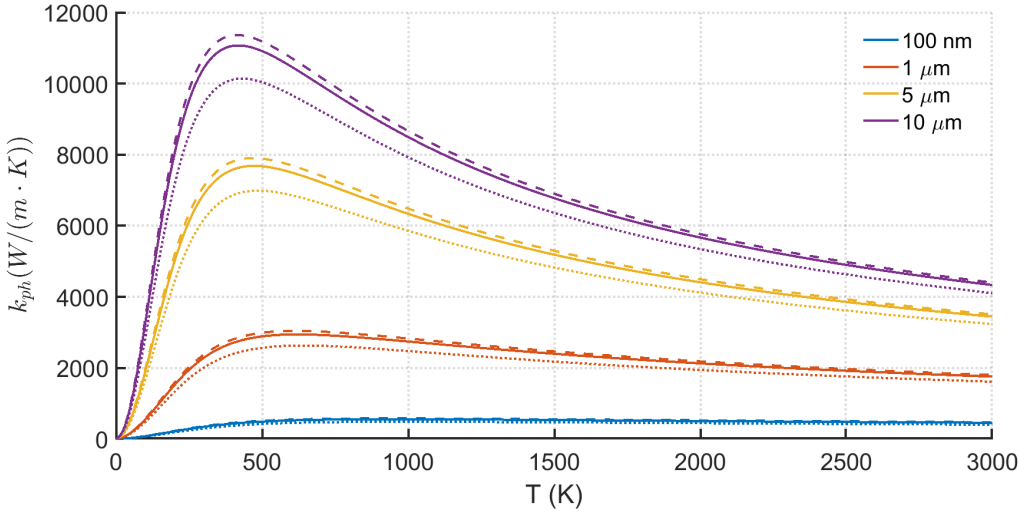

Figure 6.13: Conductivity in diffusive regime for graphene to the change of L_z and of the specularity parameter p: p=1 (dashed line), p=0.9 (solid line), p=0.6 (dotted line)

Through the observation of these figures, many qualitative considerations can be drawn about the lattice thermal conductivity of graphene and the method adopted to deduce it:

1) First of all, a strong dependence of the conductivity on the size of the sample is observed.
   This may seem like a mistake due to the fact that in macroscopic 3D systems the conductivity is defined as a size independent quantity. The reason lies in the physical phenomena arising in 2D materials and in the

physics of transport processes in mesoscopic systems. When dimensionality is reduced or the relevant sizes reach the mesoscopic scale (from tens of nanometers to tens of microns), the knowledge developed on conventional bulk crystals becomes insufficient, and novel properties emerge [8]. This is consistent with the theoretical prediction that heat carriers in graphene can propagate along distances up to the millimetre scale [6]. The origin of such behaviour is under active investigation and it is debated, with arguments focusing on dimensionality effects and on the reduction of the allowed scattering processes [8].

2) Let us focus on the samples with sizes in the order of a few microns, namely on the curves corresponding to $L_z = 1, 3, 5, 10$ μm, which correspond to the sizes of samples usually tested experimentally. The thermal conductivity at room temperature (T=300 K) varies in the range $2000 - 10000$ W m^{-1} K^{-1}. This is exactly the same order of magnitude of most the theoretical and experimental findings.
It has to be noticed that, while it is universally recognised that graphene has the highest known thermal conductivity, well-defined values of the thermal conductivity as a function of temperature, size and other parameters are far from being uniquely determined. Indeed, even if the recent availability of high quality single-layer graphene samples has allowed for a large number of experimental studies, definitive results remain elusive. The difficulty is reflected in a variety of estimates, spanning a rather large range of values between 1500 and 5000 W m^{-1} K^{-1} at room temperature [4]. On the theoretical side, the estimates are equally uncertain and vary in an even larger range of κ between 1000 and 10000 W m^{-1} K^{-1} [17].
Undoubtedly, one thing is clear: graphene shows extremely high thermal conductivity, some orders of magnitude larger than the one found for single-layer MoS_2in Ch. 5.2.
It results from these comparisons that the method used in this chapter provides reliable estimates, at least from a qualitative point of view.

3) The thermal conductivity increases with temperature up to 300-400 K. Then a decreasing trend is observed due to the $1/T$ dependence of the Umklapp phonon mean free path.
In literature [66, 17], the conductivity usually reaches the maximum at lower temperatures ($T\sim 150$ K) and then it decreases rapidly. On the contrary, one has to go to very high temperatures (fig. 6.13) to see a remarkable decrease of the conductivity in this calculation. In any case, the method provides a qualitative correct behaviour. The difference in the trend may occur partially due to the inclusion in this calculation of the ZA optical mode, which displays a long mean free path.
There is still a lot of research going on to evaluate the phonon-phonon scattering in a correct way and to understand which modes contribute significantly to the thermal conductivity. The formula used for the calculations of the life times (eq. 6.5), coming from the Klemens model, has proven its efficacy in many works, but its broad range of applicability is

questionable and requires further analysis. For example, a more precise way of treating the three phonons Umklapp scattering should consider the selection rules for all the allowed momentum transitions in the first Brillouin zone [47].

4) Let us now consider the size effects arising for L_z shorter than 1 μm and larger than 10 μm.

   – According to eq. 6.1, for $L_z << \Lambda$:

$$\begin{aligned} G_{ph} &\propto \frac{\Lambda}{L_z + \Lambda} \xrightarrow{L_z << \Lambda} const \\ k_{ph} &\propto L_z \cdot \frac{\Lambda}{L_z + \Lambda} \xrightarrow{L_z << \Lambda} L_z \end{aligned} \tag{6.10}$$

   This behaviour is well reproduced by the model used. In fact, in the limit of very short lengths, the ballistic case is recovered. In fig. 6.10 it is possible to see that the conductance curves approach the ballistic conductance for decreasing L_z.

   – At very long lengths of the sample ($L_z >> \Lambda$) the classical diffusive regime should be recovered, with the conductivity that is supposed to converge towards the value predicted by Fourier laws.
   In the case of $L_z >> \Lambda$, eq. 6.1 provides the following information:

$$\begin{aligned} G_{ph} &\propto \frac{\Lambda}{L_z + \Lambda} \xrightarrow{L_z >> \Lambda} \Lambda / L_z \\ k_{ph} &\propto L_z \cdot \frac{\Lambda}{L_z + \Lambda} \xrightarrow{L_z >> \Lambda} \Lambda \end{aligned} \tag{6.11}$$

   The classical diffusive limit is more problematic to reproduce, because the conductivity is proportional to the phonon mean free path, which depends on many variables. Usually researchers are treating it by inserting a cut-off for the mean free path of phonons with very long wavelength.
   These correspond to phonons in the neighbourhood of the Γ point, which are not expected to contribute to Umklapp scattering. However, it is still not clear how Normal processes contribute to resistive phenomena by altering the phonon distribution in presence of other inelastic scattering phenomena (see Ch. 3.2). A method that could provide a better insight is based on solving iteratively the Boltzmann transport equations, in order to go beyond the relaxation time approximation (RTA) [8, 17].
   Within the approach used in this thesis, no cut-off at low frequencies was considered. This is why the conductivity curves do not converge at the increase of L_z. Indeed, the mean free paths of TA and LA phonons can be unusually large at low frequencies (in the order of millimiters).

However, even if many ways are present in literature, none of them was convincing due to the luck of a clear physical meaning. In addition, Nika *et al.* showed that the use of an arbitrary low-bound cut-off for the phonon frequency in the thermal conductivity integral for graphene leads to erroneous results [49].

5) The model is not including other defects that are present in experimental conditions, especially in large samples: isotope effect, grain boundaries, Stone-Wales defects, strains, interaction with the substrate, ecc.
These scattering phenomena naturally limit the mean free path and avoid the divergence of the conductivity with increasing sample size. In fact, according to Matthiessen's rule: $\Lambda_{tot}^{-1} = \sum_i \Lambda_i^{-1}$, where i indicates the i-th scattering mechanism.
These defects may be included in further analysis. This mixed approach may turn out to be valuable in this prospective. In fact, naturally occurring defects in the lattice, such as isotopes and Stone-Wales defects, can be treated with great accuracy within the Landauer Formalism, and the effect of anharmonicity can be included via the calculation of the phonon life time, which is a typical concept of methods based on BTE.

In conclusion, the adopted method is able to give accurate estimates on the thermal conductivity of graphene, providing an insight on the transition between ballistic and diffusive regime.

Chapter 7

Conclusions and Future Perspectives

In this thesis the thermal transport properties of graphene and single-layer TMDCs were investigated by DFT calculations using the *SIESTA ab intio* package, within the framework of the Landauer Formalism.
The lattice thermal conductance of pristine graphene, MoS_2, WS_2, $MoSe_2$ and WSe_2 were studied as a function of the temperature in ballistic regime. Comparing the results obtained for these 2D materials, it is clear that TMDCs own a thermal conductance per unit width which is significantly lower with respect to the one of graphene. It was highlighted that going beyond the ballistic regime, by including the Umklapp phonon-phonon scattering processes, is essential for comparing the intrinsic thermal conductivity of pristine materials with experimental results.

A strategy to further reduce the thermal conductivity of TMDCs consisted in the introduction of chalcogen atom vacancies. The aim was to verify to which extent the thermoelectric figure of merit can be improved.
Two analyses were conducted on SL MoS_2 in the presence of a disordered distribution of sulphur vacancies by changing the concentration of defects and the length of the sample. The atomistic Green's function technique was used to deal with the presence of disorder in the systems. This represents an original contribution with respect to previous works present in literature. The results for systems with sulphur vacancies demonstrated a clear reduction of the thermal conductivity compared to the pristine case. In particular, it was shown that the contribution of the optical modes to the phonon transport is highly suppressed.
The lattice thermal conductivity decreases with higher concentration of sulphur vacancies and with longer length of the sample.
The thermoelectric figure of merit of the defective SL MoS_2 was computed by combining the results on the lattice thermal conductivity with data on the electronic transport properties. It was found that for n-type materials, ZT is decreased by the presence of sulphur vacancies, independently of the concentration and of the temperature. Instead, a slight improvement of ZT was observed for p-type materials at low temperature. Hence, the hypoth-

esis regarding the reduction of the thermal conductivity upon introduction of S vacancies was proved. Nonetheless, this is not sufficient to obtain a significant improvement of ZT because of the detrimental impact on the electric conductivity.
Still, the procedure used to deal with a disordered distribution of defects opens the way for future studies. For example, a combination of different kinds of defects can be inserted in the material. Another option may be to tune the concentration of defects locally in the sample with the purpose of finding better and better strategies to achieve a good "phonon-glass electron-crystal" behaviour via defect engineering.

A method was implemented in order to include phonon-phonon Umklapp scattering and phonon-boundary scattering in the calculation of the thermal conductivity. The proposed approach combines the computation of the transmission, the main feature of the Landauer Formalism, with the examination of the phonon life times, which is typical of methods based on the Boltzmann transport equations. A key step of this procedure consisted in the calculation of the mode Grüneisen parameter, which has been an original addition which I contributed to the team.
The method was successfully applied in the calculation of the thermal conductivity of graphene and it allowed to evaluate the transition from ballistic to diffusive regime.

Bibliography

[1] Ch. Adessi, S. Thebaud, R. Bouzerar, and G. Bouzerar. First Principle Investigation on Thermoelectric Properties of Transition Metal Dichalcogenides: Beyond the Rigid Band Model. *The Journal of Physical Chemistry C*, 121(23):12577–12584, 2017.

[2] Emilio Artacho, E Anglada, O Diéguez, J D Gale, A García, J Junquera, R M Martin, P Ordejón, J M Pruneda, D Sánchez-Portal, and J M Soler. The SIESTA method; developments and applicability. *Journal of Physics: Condensed Matter*, 20(6):064208, 2008.

[3] N.W. Ashcroft and N.D. Mermin. *Solid State Physics*. Saunders College, Philadelphia, 1976.

[4] Alexander A. Balandin and Denis L. Nika. Phononics in low-dimensional materials. *Materials Today*, 15(6):266 – 275, 2012.

[5] D R Bowler and T Miyazaki. O(N) methods in electronic structure calculations. *Reports on Progress in Physics*, 75(3):036503, 2012.

[6] Weiwei Cai, Arden L. Moore, Yanwu Zhu, Xuesong Li, Shanshan Chen, Li Shi, and Rodney S. Ruoff. Thermal Transport in Suspended and Supported Monolayer Graphene Grown by Chemical Vapor Deposition. *Nano Letters*, 10(5):1645–1651, 2010. PMID: 20405895.

[7] Yongqing Cai, Jinghua Lan, Gang Zhang, and Yong-Wei Zhang. Lattice vibrational modes and phonon thermal conductivity of monolayer MoS_2. *Phys. Rev. B*, 89:035438, 2014.

[8] Andrea Cepellotti, Giorgia Fugallo, Lorenzo Paulatto, Michele Lazzeri, Francesco Mauri, and Nicola Marzari. Phonon hydrodynamics in two-dimensional materials. *Nature communications*, 6:6400, 2015.

[9] Po-Hao Chang, Mohammad Saeed Bahramy, Naoto Nagaosa, and Branislav K. Nikolić. Giant Thermoelectric Effect in Graphene-Based Topological Insulators with Heavy Adatoms and Nanopores. *Nano Letters*, 14(7):3779–3784, 2014. PMID: 24932511.

[10] Sang-Soo Chee, Chohee Oh, Myungwoo Son, Gi-Cheol Son, Hanbyeol Jang, Tae Jin Yoo, Seungmin Lee, Wonki Lee, Jun Yeon

Hwang, Hyunyong Choi, Byoung Hun Lee, and Moon-Ho Ham. Sulfur vacancy-induced reversible doping of transition metal disulfides via hydrazine treatment. *Nanoscale*, 9:9333–9339, 2017.

[11] Supriyo Datta. *Quantum Transport: Atom to Transistor*. Cambridge University Press, 2005.

[12] Jiao Deng, Dehui Deng, and Xinhe Bao. Robust Catalysis on 2D Materials Encapsulating Metals: Concept, Application, and Perspective. *Advanced Materials*, 29(43):1606967, 2017.

[13] Zhiwei Ding, Jiawei Zhou, Bai Song, Mingda Li, Te-Huan Liu, and Gang Chen. Umklapp scattering is not necessarily resistive. *Phys. Rev. B*, 98:180302, 2018.

[14] M.S. Dresselhaus, G. Chen, M.Y. Tang, R.G. Yang, H. Lee, D.Z. Wang, Z.F. Ren, J.-P. Fleurial, and P. Gogna. New Directions for Low-Dimensional Thermoelectric Materials. *Advanced Materials*, 19(8):1043–1053, 2007.

[15] R. P. Feynman. Forces in Molecules. *Phys. Rev.*, 56:340–343, 1939.

[16] Carlos Fiolhais, Fernando Nogueira, and Miguel Marques. *A Primer in Density Functional Theory*, volume 620 of *Lecture Notes in Physics*. Springer, 2003.

[17] Giorgia Fugallo, Andrea Cepellotti, Lorenzo Paulatto, Michele Lazzeri, Nicola Marzari, and Francesco Mauri. Thermal Conductivity of Graphene and Graphite: Collective Excitations and Mean Free Paths. *Nano Letters*, 14(11):6109–6114, 2014. PMID: 25343716.

[18] P G. Klemens. Thermal Conductivity and Lattice Vibrational Modes . *Solid State Physics (edited by F. Seitz and D. Turnbull (Academic, New York))*, 7:1, 1958.

[19] P G. Klemens. Theory of the A-Plane Thermal Conductivity of Graphite. *Journal of Wide Bandgap Materials*, 7:332–339, 2000.

[20] D .J. Griffiths. *Introduction to Quantum Mechanics*. Pearson Prentice Hall, 2005.

[21] Xiaokun Gu and Ronggui Yang. Phonon transport in single-layer transition metal dichalcogenides: A first-principles study. *Applied Physics Letters*, 105(13):131903, 2014.

[22] Xiaokun Gu and Ronggui Yang. Phonon transport and thermal conductivity in two-dimensional materials. *Annual Review of Heat Transfer*, 19:1–65, 2015.

[23] D. R. Hamann, M. Schluter, and C. Chiang. Norm-Conserving Pseudopotentials. *Phys. Rev. Lett.*, 43:1494–1497, 1979.

[24] Oded Hod, Juan Peralta, and Gustavo E Scuseria. First-principles electronic transport calculations in finite elongated systems: A divide and conquer approach. *The Journal of chemical physics*, 125:114704, 2006.

[25] P. Hohenberg and W. Kohn. Inhomogeneous Electron Gas. *Phys. Rev.*, 136:B864–B871, 1964.

[26] Zhishuo Huang, Wenxu Zhang, and Wanli Zhang. Computational Search for Two-Dimensional MX_2 Semiconductors with Possible High Electron Mobility at Room Temperature. *Materials*, 9(9), 2016.

[27] Changwook Jeong, Supriyo Datta, and Mark Lundstrom. Full dispersion versus Debye model evaluation of lattice thermal conductivity with a Landauer approach. *Journal of Applied Physics*, 109(7):073718, 2011.

[28] Changwook Jeong, Raseong Kim, Mathieu Luisier, Supriyo Datta, and Mark Lundstrom. On Landauer versus Boltzmann and full band versus effective mass evaluation of thermoelectric transport coefficients. *Journal of Applied Physics*, 107(2):023707, 2010.

[29] S. Jiménez Sandoval, D. Yang, R. F. Frindt, and J. C. Irwin. Raman study and lattice dynamics of single molecular layers of MoS_2. *Phys. Rev. B*, 44:3955–3962, 1991.

[30] Javier Junquera. Atomic orbitals of finite range as basis sets. `https://personales.unican.es/junqueraj/JavierJunquera_files/Talks/Bases.pdf`, October 2015.

[31] Javier Junquera. Fundamentals: the quantum mechanical many-body problem and the Density Functional Theory approach. `https://personales.unican.es/junqueraj/JavierJunquera_files/Talks/Introduction_dft.pdf`, October 2015.

[32] Javier Junquera, Óscar Paz, Daniel Sánchez-Portal, and Emilio Artacho. Numerical atomic orbitals for linear-scaling calculations. *Phys. Rev. B*, 64:235111, 2001.

[33] In Soo Kim, Vinod K. Sangwan, Deep Jariwala, Joshua D. Wood, Spencer Park, Kan-Sheng Chen, Fengyuan Shi, Francisco Ruiz-Zepeda, Arturo Ponce, Miguel Jose-Yacaman, Vinayak P. Dravid, Tobin J. Marks, Mark C. Hersam, and Lincoln J. Lauhon. Influence of Stoichiometry on the Optical and Electrical Properties of Chemical Vapor Deposition Derived MoS_2. *ACS Nano*, 8(10):10551–10558, 2014. PMID: 25223821.

[34] C. Kittel. *Introduction to solid state physics*. John Wiley and Sons Inc, 8th edition, 1976.

[35] P.G. Klemens and D.F. Pedraza. Thermal conductivity of graphite in the basal plane. *Carbon*, 32(4):735 – 741, 1994.

[36] W. Kohn and L. J. Sham. Self-Consistent Equations Including Exchange and Correlation Effects. *Phys. Rev.*, 140:A1133–A1138, 1965.

[37] Wu Li, J. Carrete, and Natalio Mingo. Thermal conductivity and phonon linewidths of monolayer MoS_2 from first principles. *Applied Physics Letters*, 103(25):253103, 2013.

[38] Yuan Liu, Nathan O. Weiss, Xidong Duan, Hung-Chieh Cheng, Yu Huang, and Xiangfeng Duan. Van der Waals Heterostructures and Devices. *Nature Reviews Materials*, 1:16042, 2016.

[39] Igor A. Luk'yanchuk, Yakov Kopelevich, and Mimoun El Marssi. Dirac Fermions in graphite: The state of art. *Physica B Condensed Matter*, 404:404–406, 2009.

[40] Mark Lundstrom. Phonon Transport: A Landauer Approach. `https://nanohub.org/groups/ece656_f17/File:36_Phonon_Transport_V3.pdf`, October 2017.

[41] Sarita Mann and V. K. Jindal. Thermal expansion in 2D honeycomb structures: Role of transverse phonon modes. *arXiv e-prints*, page arXiv:1606.07656, 2016.

[42] A. A. Maznev and O. B. Wright. Demystifying umklapp vs normal scattering in lattice thermal conductivity. *American Journal of Physics*, 82(11):1062–1066, 2014.

[43] K. H. Michel, S. Costamagna, and F. M. Peeters. Theory of anharmonic phonons in two-dimensional crystals. *Phys. Rev. B*, 91:134302, 2015.

[44] Vladimir V. Mitin, Viatcheslav A. Kochelap, and Michael A. Stroscio. *Introduction to Nanoelectronics: Science, Nanotechnology, Engineering, and Applications*. Cambridge University Press, New York, NY, USA, 1st edition, 2008.

[45] Hendrik J. Monkhorst and James D. Pack. Special points for Brillouin-zone integrations. *Phys. Rev. B*, 13:5188–5192, 1976.

[46] D. L. Nika, S. Ghosh, E. P. Pokatilov, and A. A. Balandin. Lattice thermal conductivity of graphene flakes: Comparison with bulk graphite. *Applied Physics Letters*, 94(20):203103, 2009.

[47] D. L. Nika, E. P. Pokatilov, A. S. Askerov, and A. A. Balandin. Phonon thermal conduction in graphene: Role of Umklapp and edge roughness scattering. *Phys. Rev. B*, 79:155413, 2009.

[48] Denis L Nika and Alexander A Balandin. Two-dimensional phonon transport in graphene. *Journal of Physics: Condensed Matter*, 24(23):233203, 2012.

[49] Denis L. Nika, Evghenii P. Pokatilov, and Alexander A. Balandin. Theoretical description of thermal transport in graphene: The issues of phonon cut-off frequencies and polarization branches. *physica status solidi (b)*, 248(11):2609–2614, 2011.

[50] K. S. Novoselov, A. Mishchenko, A. Carvalho, and A. H. Castro Neto. 2D materials and van der Waals heterostructures. *Science*, 353(6298), 2016.

[51] Pablo Ordejón. VIBRA Package, Version 0.1.1 - User's Manual. `www.mail-archive.com/siesta-l@listserv.uam.es/msg02665/vibra.pdf`, June 2003.

[52] C. Oshima, T. Aizawa, R. Souda, Y. Ishizawa, and Y. Sumiyoshi. Surface phonon dispersion curves of graphite (0001) over the entire energy region. *Solid State Communications*, 65(12):1601 – 1604, 1988.

[53] M. Paulsson. Non Equilibrium Green's Functions for Dummies: Introduction to the One Particle NEGF equations. *arXiv e-prints*, pages cond–mat/0210519, 2002.

[54] M. C. Payne, M. P. Teter, D. C. Allan, T. A. Arias, and J. D. Joannopoulos. Iterative minimization techniques for ab initio total-energy calculations: molecular dynamics and conjugate gradients. *Rev. Mod. Phys.*, 64:1045–1097, 1992.

[55] Bo Peng, Zeyu Ning, Hao Zhang, Hezhu Shao, Yuanfeng Xu, Gang Ni, and Heyuan Zhu. Beyond Perturbation: Role of Vacancy-Induced Localized Phonon States in Thermal Transport of Monolayer MoS_2. *The Journal of Physical Chemistry C*, 120(51):29324–29331, 2016.

[56] Bo Peng, Hao Zhang, Hezhu Shao, Yuanfeng Xu, Xiangchao Zhang, and Heyuan Zhu. Towards intrinsic phonon transport in single-layer MoS_2. *Annalen der Physik*, 528(6):504–511, 2016.

[57] Bo Peng, Hao Zhang, Hezhu Shao, Yuchen Xu, Xiangchao Zhang, and Heyuan Zhu. Thermal conductivity of monolayer MoS_2 , $MoSe_2$, and WS_2 : interplay of mass effect, interatomic bonding and anharmonicity. *RSC Adv.*, 6:5767–5773, 2016.

[58] John P. Perdew, Kieron Burke, and Matthias Ernzerhof. Generalized Gradient Approximation Made Simple. *Phys. Rev. Lett.*, 77:3865–3868, 1996.

[59] Branimir Radisavljevic, Aleksandra Radenovic, Jacopo Brivio, Valentina Giacometti, and Andras Kis. Single-layer MoS_2 transistors. *Nature nanotechnology*, 6 3:147–50, 2011.

[60] C. Rice, R. J. Young, R. Zan, U. Bangert, D. Wolverson, T. Georgiou, R. Jalil, and K. S. Novoselov. Raman-scattering measurements and first-principles calculations of strain-induced phonon shifts in monolayer MoS_2. *Phys. Rev. B*, 87:081307, 2013.

[61] F. Ritz and C. E. Peterson. Multi-mission radioisotope thermoelectric generator (MMRTG) program overview. *IEEE Aerospace Conference Proceedings*, 5:2950–2957 Vol.5, 2004.

[62] K S. Novoselov, A K. Geim, S Morozov, Da Jiang, Yanshui Zhang, S V. Dubonos, Irina Grigorieva, and A A. Firsov. Electric Field Effect in Atomically Thin Carbon Films. *Nat. Mater.*, 6, 2004.

[63] Daniel Sánchez-Portal, Emilio Artacho, José M. Soler, Angel Rubio, and Pablo Ordejón. Ab initio structural, elastic, and vibrational properties of carbon nanotubes. *Phys. Rev. B*, 59:12678–12688, 1999.

[64] Matthias Schrade and Terje G. Finstad. Using the Callaway Model to Deduce Relevant Phonon Scattering Processes: The Importance of Phonon Dispersion. *Physica Status Solidi B Basic Research*, 255:1800208, 2018.

[65] Edmund G. Seebauer and Kyong Wook Noh. Trends in semiconductor defect engineering at the nanoscale. *Materials Science and Engineering: R: Reports*, 70(3):151 – 168, 2010. 3rd IEEE International NanoElectronics Conference (INEC).

[66] Yulu Shen, G Xie, Xiaolin Wei, Kaiwang Zhang, Minghua Tang, Jianxin Zhong, Gang Zhang, and Yong-Wei Zhang. Size and boundary scattering controlled contribution of spectral phonons to the thermal conductivity in graphene ribbons. *Journal of Applied Physics*, 115, 2014.

[67] Jonathan R Shewchuk. An Introduction to the Conjugate Gradient Method Without the Agonizing Pain. Technical report, Pittsburgh, PA, USA, 1994.

[68] Jose Silva-Guillén, Pablo San-Jose, and Rafael Roldán. Electronic Band Structure of Transition Metal Dichalcogenides from Ab Initio and Slater–Koster Tight-Binding Model. *Applied Sciences*, 6(10):284, 2016.

[69] U. Sivan and Y. Imry. Multichannel Landauer formula for thermoelectric transport with application to thermopower near the mobility edge. *Phys. Rev. B*, 33:551–558, 1986.

[70] G. Jeffrey Snyder and Eric S. Toberer. Complex thermoelectric materials. *Nature Materials*, 7(2):105–114, 2008.

[71] José M Soler, Emilio Artacho, Julian D Gale, Alberto García, Javier Junquera, Pablo Ordejón, and Daniel Sánchez-Portal. The SIESTA method for ab initio order- N materials simulation. *Journal of Physics: Condensed Matter*, 14(11):2745, 2002.

[72] Andrea Splendiani, Liang Sun, Yuanbo Zhang, Tianshu Li, Jonghwan Kim, Chi-Yung Chim, Giulia Galli, and Feng Wang. Emerging Photoluminescence in Monolayer MoS_2. *Nano Letters*, 10(4):1271–1275, 2010. PMID: 20229981.

[73] Andrzej Taube, Jaroslaw Judek, Anna Lapińska, and Mariusz Zdrojek. Temperature-Dependent Thermal Properties of Supported MoS_2 Monolayers. *ACS Applied Materials & Interfaces*, 7(9):5061–5065, 2015. PMID: 25706435.

[74] S. Thébaud, Ch. Adessi, S. Pailhès, and G. Bouzerar. Boosting the power factor with resonant states: A model study. *Phys. Rev. B*, 96:075201, Aug 2017.

[75] Atsushi Togo. Phonopy manual - Release 1.7.4. `https://www.researchgate.net/profile/Fatih_Ersan/post/How_can_I_calculate_lattice_thermal_conductivity_using_phonopy_code/attachment/59d6262579197b80779846ef/AS%3A320708796715008%401453474343187/download/phonopy-manual.pdf`, December 04, 2013.

[76] Atsushi Togo, Fumiyasu Oba, and Isao Tanaka. First-principles calculations of the ferroelastic transition between rutile-type and $CaCl_2$-type SiO_2 at high pressures. *Phys. Rev. B*, 78:134106, 2008.

[77] Atsushi Togo and Isao Tanaka. First principles phonon calculations in materials science. *Scripta Materialia*, 108:1 – 5, 2015.

[78] Mahmut Tosun, Leslie Chan, Matin Amani, Tania Roy, Geun Ho Ahn, Peyman Taheri, Carlo Carraro, Joel W. Ager, Roya Maboudian, and Ali Javey. Air-Stable n-Doping of WSe_2 by Anion Vacancy Formation with Mild Plasma Treatment. *ACS Nano*, 10(7):6853–6860, 2016. PMID: 27294286.

[79] T.M. Tritt. Thermoelectric Materials, Phenomena, and Applications: A Bird's Eye View. *MRS Bulletin*, 31:188 – 198, 2006.

[80] N. Troullier and José Luís Martins. Efficient pseudopotentials for plane-wave calculations. *Phys. Rev. B*, 43:1993–2006, 1991.

[81] Charlie Tsai, Hong Li, Sangwook Park, Joonsuk Park, Hyun Soo Han, Jens K NÃ¸rskov, Xiaolin Zheng, and Frank Abild-Pedersen. Electrochemical generation of sulfur vacancies in the basal plane of MoS_2 for hydrogen evolution. *Nature communications*, 8:15113, April 2017.

[82] B. J. van Wees, H. van Houten, C. W. J. Beenakker, J. G. Williamson, L. P. Kouwenhoven, D. van der Marel, and C. T. Foxon. Quantized conductance of point contacts in a two-dimensional electron gas. *Phys. Rev. Lett.*, 60:848–850, 1988.

[83] Jian-Sheng Wang, Bijay Kumar Agarwalla, Huanan Li, and Juzar Thingna. Nonequilibrium Green's function method for quantum thermal transport. *Frontiers of Physics*, 9(6):673–697, 2014.

[84] Jian-Sheng Wang, Nan Zeng, Jian Wang, and C Gan. Nonequilibrium Green's function method for thermal transport in junctions. *Physical review. E, Statistical, nonlinear, and soft matter physics*, 75:061128, 2007.

[85] Jue Wang, Fang Xie, Xuan-Hao Cao, Si-Cong An, Wuxing Zhou, Li-Ming Tang, and Ke-Qiu Chen. Excellent Thermoelectric Properties in monolayer WSe_2 Nanoribbons due to Ultralow Phonon Thermal Conductivity . *Scientific Reports*, 2017.

[86] Shao-Feng Wang, Hui-Li Zhang, and Xiao-Zhi Wu. A new rotation sum rule for the atomic force constants. *Journal of Physics: Condensed Matter*, 19(38):386233, 2007.

[87] Yongchun Wang, Kaiwang Zhang, and Guofeng Xie. Remarkable suppression of thermal conductivity by point defects in MoS_2 nanoribbons. *Applied Surface Science*, 360:107 – 112, 2016.

[88] Darshana Wickramaratne, Ferdows Zahid, and Roger K. Lake. Electronic and thermoelectric properties of few-layer transition metal dichalcogenides. *The Journal of Chemical Physics*, 140(12):124710, 2014.

[89] T. J. Wieting and J. L. Verble. Infrared and Raman Studies of Long-Wavelength Optical Phonons in Hexagonal MoS_2. *Phys. Rev. B*, 3:4286–4292, 1971.

[90] Jing Wu, Hennrik Schmidt, Kiran Kumar Amara, Xiangfan Xu, Goki Eda, and Barbaros Özyilmaz. Large Thermoelectricity via Variable Range Hopping in Chemical Vapor Deposition Grown Single-Layer MoS_2. *Nano Letters*, 14(5):2730–2734, 2014. PMID: 24749833.

[91] Huaping Xiao, Wei Cao, Tao Ouyang, Xiaoyan Xu, Yingchun Ding, and Jianxin Zhong. Thermoelectric properties of graphene nanoribbons with surface roughness. *Applied Physics Letters*, 112(23):233107, 2018.

[92] Guofeng Xie, Ding Ding, and Gang Zhang. Phonon coherence and its effect on thermal conductivity of nanostructures. *Advances in Physics: X*, 3(1):1480417, 2018.

[93] Rusen Yan, Jeffrey R. Simpson, Simone Bertolazzi, Jacopo Brivio, Michael Watson, Xufei Wu, Andras Kis, Tengfei Luo, Angela R. Hight Walker, and Huili Grace Xing. Thermal Conductivity of Monolayer Molybdenum Disulfide Obtained from Temperature-Dependent Raman Spectroscopy. *ACS Nano*, 8(1):986–993, 2014. PMID: 24377295.

[94] Zhequan Yan, Mina Yoon, and Satish Kumar. Influence of defects and doping on phonon transport properties of monolayer MoSe2. *2D Materials*, 5(3):031008, 2018.

[95] Masaro Yoshida, Takahiko Iizuka, Yu Saito, Masaru Onga, Ryuji Suzuki, Yijin Zhang, Yoshihiro Iwasa, and Sunao Shimizu. Gate-Optimized Thermoelectric Power Factor in Ultrathin WSe_2 Single Crystals. *Nano Letters*, 16(3):2061–2065, 2016. PMID: 26841275.

[96] W Zhang, Timothy Fisher, and N Mingo. The Atomistic Green's Function Method: An Efficient Simulation Approach for Nanoscale Phonon Transport. *Birck and NCN Publications*, 51, 2007.

[97] Xian Zhang, Dezheng Sun, Yilei Li, Gwan-Hyoung Lee, Xu Cui, Daniel Chenet, Yumeng You, Tony F. Heinz, and James C. Hone. Measurement of Lateral and Interfacial Thermal Conductivity of Single- and Bilayer MoS_2 and $MoSe_2$ Using Refined Optothermal Raman Technique. *ACS Applied Materials & Interfaces*, 7(46):25923–25929, 2015. PMID: 26517143.

[98] Xiaoyan Zhang, Lili Hou, Artur Ciesielski, and Paolo Samorí. 2D Materials Beyond Graphene for High-Performance Energy Storage Applications. *Advanced Energy Materials*, 6(23):1600671, 2016.

[99] Yongsheng Zhang. First-principles Debye-Callaway approach to lattice thermal conductivity. *Journal of Materiomics*, 2(3):237 – 247, 2016.

[100] Zhongwei Zhang, Yuee Xie, Yulou Ouyang, and Yuanping Chen. A systematic investigation of thermal conductivities of transition metal dichalcogenides. *International Journal of Heat and Mass Transfer*, 108:417(6), 2017-05-01.

[101] Zhongwei Zhang, Yuee Xie, Qing Peng, and Yuanping Chen. A theoretical prediction of super high-performance thermoelectric materials based on MoS_2/WS_2 hybrid nanoribbons . *Scientific Reports*, 2016-02-17 online.

[102] Wu-Xing Zhou and Ke-Qiu Chen. First-Principles Determination of Ultralow Thermal Conductivity of monolayer WSe_2 . *Scientific Reports*, 5, 2015.

[103] J.M. Ziman. *Electrons and Phonons: The Theory of Transport Phenomena in Solids*. Oxford University Press, 2001.

[104] Ji-Hang Zou, Zhen-Qiang Ye, and Bing-Yang Cao. Phonon thermal properties of graphene from molecular dynamics using different potentials. *The Journal of Chemical Physics*, 145(13):134705, 2016.